ABSTRACT

Title of Dissertation: TECHNIQUES TO MITIGATE THE EFFECTS OF ATMOSPHERIC TURBULENCE ON FREE SPACE OPTICAL COMMUNICATION LINKS

Linda Marie Wasiczko, Doctor of Philosophy, 2004

Dissertation directed by: Professor Christopher C. Davis
Department of Electrical & Computer Engineering

Free space optical communication links are an attractive technology for broadband communications when fiber optic links are unavailable or simply not feasible. Atmospheric turbulence, aerosols, and molecular absorption all affect the propagation of optical waves in the atmosphere. Since atmospheric turbulence is the major source of errors on free space optical communication links, this dissertation investigates two techniques to reduce the impact of atmospheric turbulence on such links. These two techniques are aperture averaging and the incorporation of nonimaging optical elements into optical receiver systems.

Aperture averaging is the process by which atmospheric turbulence-induced intensity fluctuations are averaged across a receiver aperture of sufficient size. We investigate the behavior of aperture averaging in weak and strong turbulence conditions by comparing experimental data with available models for plane and spherical wave

propagation. New expressions for the aperture averaging factor in weak turbulence are given. In strong turbulence conditions, aperture averaging is analyzed with special attention to the various wavenumber spectrum models. This is the first report of experimental strong fluctuation aperture averaging data acquired in non-saturated conditions.

Nonimaging optical elements are particularly useful for the mitigation of atmospheric turbulence-induced beam wander in the focal plane of a free space optical communication receiver. Experimental results of the bit error ratio enhancement due to the incorporation of a nonimaging optical element, specifically a compound parabolic concentrator, are presented. Two link ranges were tested, a 1.7 km link at the University of Maryland experiencing weak turbulence, and a 32.4 km link at the Naval Research Laboratory's Chesapeake Bay Detachment experiencing saturated, strong turbulence. These results are the first reported experimental test of a nonimaging optical element integrated into an outdoor free space optical communications system.

TECHNIQUES TO MITIGATE THE EFFECTS OF ATMOSPHERIC TURBULENCE ON FREE SPACE OPTICAL COMMUNICATION LINKS

by

Linda Marie Wasiczko

Dissertation submitted to the Faculty of the Graduate School of the
University of Maryland, College Park in partial fulfillment
of the requirements for the degree of
Doctor of Philosophy
2004

Advisory Committee:

Professor Christopher C. Davis, Chair
Professor Pamela Abshire
Professor Agisilaos A. Iliadis
Professor Thomas E. Murphy
Professor Owen E. Thompson

Dedication

To my Parents, Bernadine & Dennis,

for teaching me perseverance,

humility, and faith

Keep smiling

Acknowledgements

I want to express my appreciation to my advisor, Prof. Christopher Davis, for his wisdom, friendship, and support during this experience. I also want to thank the members of my dissertation committee for their service and guidance.

I want to thank two dear colleagues and friends for their continuing encouragement: Dr. Patricia Mead and Dr. H. Craig Casey.

I am thankful for the technical and non-technical discussions with my colleagues in the Maryland Optics Group at the University of Maryland, especially: Dr. Igor Smolyaninov, Dr. Stuart Milner, Dr. Quirino Balzano, and Dr. Vildana Hodzic. I also want to thank Dr. Kyuman Cho for introducing me to this project.

I have enjoyed fruitful conversations and collaboration with members of the free space optics community, especially: Dr. Ray Burris, Dr. Chris Moore, and Mr. Michael Vilcheck, of the Naval Research Laboratory; Dr. Jennifer Ricklin and Dr. Mikhail Vorontsov, of the Army Research Laboratory; and Dr. Charles Thompson of the Lawrence Livermore National Laboratory. I appreciate the equipment loans to this dissertation research from Prof. Agis Iliadis, Dr. J. "Buzz" Graves at AOptix, Inc., and Prof. Mario Dagenais.

The American Association of University Women sponsored my dissertation year work through a Selected Professions Fellowship, for which I am extremely grateful.

Finally, I want to thank my parents, my sister, Pamela, and my friends who have supported (and antagonized) me throughout my many years in graduate school.

TABLE OF CONTENTS

LIST OF TABLES

LIST OF FIGURES

Chapter 1

Introduction

1.1 History of Free Space Optical Communication

Since the invention of the Ruby laser in 1960, scientists have attempted to establish reliable communications channels by modulating and propagating optical signals over a line-of-sight path [1]. Most of the early development of free space optical communication links was directed towards space-based applications [2,3,4]. Due to the relative immaturity of laser technology and flawed system demonstrations, research in free space optical communication began a cycle of declining interest and funding, only to be resurrected over and over again.

During the mid- to late-1990s, free space laser communication was once again resurrected. This time, an increasing demand for high bandwidth communications, fueled by the explosion of the internet, renewed interest in free space optics (FSO). By this time, optical fiber communications was well established, and researchers had found ways to use these efficient, cost-effective components in FSO systems.

FSO was voted one of the ten hottest technologies in 2001 [5]. The hype surrounding the technology was partly due to the lack of optical fiber backbone connectivity in metropolitan areas and the high cost of laying optical fiber in those areas. After September 11, 2001, FSO systems were deployed to reconnect parts of the critical New York City infrastructure; after copper wires, optical fiber, and RF antennas were destroyed. The advantages of FSO were trumpeted throughout the

telecommunications sector. These advantages include: rapidly deployablility; support for high bandwidth transmissions; high security; the ability to extend the reach of the optical fiber backbone; and use in disaster recovery situations. Unfortunately, the technology bubble in the stock market burst. This left FSO vendors without telecommunication and cable carriers who could purchase and deploy FSO units on a large scale.

Even with the significant capital investment in FSO during this time, researchers did not solve the technology's reliability problems due to atmospheric turbulence, aerosols, and molecular attenuation. These three environmental properties destroy the coherence of a propagating optical wavefront. The research presented here demonstrates techniques to mitigate the distortions induced on the optical beam by atmospheric turbulence.

1.2 Free Space Optical Communication Techniques

Researchers have pursued a variety of system architectures in an attempt to improve the reliability of FSO links. A "bare bones" FSO system transmits "1" bits by turning the optical source on, and "0" bits by turning the optical source off. This method is called intensity modulation/direct detection (IM/DD), or on-off keying (OOK). This is a low overhead technique, because there is no attempt made to ensure the integrity of the signal. This transmission scheme attempts to collect enough photons at the receiver to correctly detect "1" and "0" bits. Atmospheric turbulence may easily prevent the detection of a sufficient number of photons to correctly interpret the received bits.

Beyond the basic IM/DD scheme, researchers have tried to come up with techniques to improve the likelihood that data bits will be received correctly. Scientists have used adaptive optics techniques, originally developed to improve the quality of stellar telescopes, to try to restore a distorted wavefront to its original state before it was destroyed by atmospheric turbulence. Some used phase conjugation techniques, to pre-distort the beam and hope that atmospheric turbulence, by distorting the wavefront, will actually work to render the wavefront to its unperturbed form. Although these techniques have shown limited success, they require bulky and computation-intensive systems to achieve wavefront correction. Additionally, systems have not been able to compute the wavefront correction fast enough to entirely counteract the affects of atmospheric turbulence.

Diversity techniques are another method of improving the reliability of an FSO system. In effect, if the optical wavefront propagates in at least two distinct ways, there is an increased likelihood that the detected signal will be read correctly. Diversity can occur in the form of spatial diversity (requiring multiple transmitters and/or receivers), temporal diversity (requiring a signal to be transmitted twice, separated by a time delay), or wavelength diversity (requiring the transmission of data on at least two distinct wavelengths). Each of these techniques requires a synchronization of the received signals. Although the techniques are promising, they do require a significant electronic overhead in the retiming and synchronization process.

Finally, coding schemes used in RF and wired communications systems have been adapted for FSO communication. Methods requiring heterodyne detection, including phase shift keying and quadrature amplitude modulation, have been

experimentally demonstrated but do not guarantee enough improvement to be viable commercially [6,7]. Forward error-correction (FEC) codes insert check bits into the data stream, which contribute an additional power and bandwidth overhead on the system. Although coding provides an additional layer of information security, studies have shown that even the best FEC codes cannot negate the affects of atmospheric turbulence alone [6,8,9].

1.3 Low-Overhead Techniques to Mitigate the Effects of Atmospheric Turbulence

The research presented here demonstrates how high-performance FSO communication systems may be designed using techniques that add nearly no power, bandwidth, size, or weight overhead to the overall design.

1.3.1 Aperture Averaging

Aperture averaging is a well known concept, which states that the amount of measured radiation may be increased by increasing the size of the receiver collecting lens aperture. In effect, any irradiance fluctuations across the collecting lens are "averaged" by the size of the lens. Therefore, a lens of any diameter will collect more photons than an ideal point receiver. In a binary communications transmission, such as OOK, aperture averaging will increase the likelihood of correctly detecting the transmitted data stream.

Aperture averaging of irradiance fluctuations was first studied by Fried in 1967 [10]. Fried developed a theoretical expression characterizing the amount of aperture averaging given an incident infinite plane wave. Aperture averaging was experimentally investigated for both horizontal and space-to-ground paths under weak

levels of atmospheric turbulence. However, Fried came to an erroneous conclusion that the amount of aperture averaging is proportional to the inverse square of the aperture diameter. Later in 1973, Fried came to the correct conclusion that there is a $-7/3$ power dependence.

Subsequent experiments on aperture averaging in weak atmospheric turbulence found very poor agreement with theory. The concept that the amount of irradiance fluctuations saturates after a certain propagation distance was not understood, so scientists could not truly differentiate between weak and strong fluctuations. Finally, in 1991, Churnside published experimental results that have shown the best agreement with theory in weak turbulence conditions until now [11]. The behavior of optical waves propagating in strong turbulence is not well understood, although new theories and models have been developed recently. As such, there have been no consistent experimental results for aperture averaging in strong turbulence.

1.3.2 Nonimaging Optics

On a basic level, imaging optics form an image based on the transformation of an object by an imaging element. A lens or compound lens is a typical imaging element. If a converging lens is used, then the object and image are located on opposite sides of the lens, when the object is placed at or beyond the focal length of the lens. A diverging lens will form a virtual image on the same side of the lens as the object. Ideally, the image or virtual image is a perfect replica of the object, although its size may be magnified or reduced.

Imaging optics are useful when the quality of an optical wavefront must be preserved. In the case of FSO with IM/DD, we are only concerned with collecting a

maximum number of photons. Any information about the phase of the wavefront is ignored. Atmospheric turbulence will destroy the coherence of a propagating optical wave, and induce phenomena that will affect the collection of a maximum number of photons.

Nonimaging optics are not required to preserve the integrity of the object. Instead, what would be the image may be partially or completely randomized. Only the conservation of energy is required. A special type of nonimaging optical element is called a concentrator. These elements collect radiation over a restricted angular range, and dispense radiation over a wider angular range. The concentrator operates on the principle of conservation of brightness, preserving the relationship between the irradiance and its angular distribution.

In this research, a nonimaging concentrator is used to mitigate the affects of atmospheric turbulence on the focal plane of an imaging optical receiver. The nonimaging concentrator will not preserve the coherence of the wavefront, but will improve the detection efficiency of the receiver.

1.4 Useful Terminology

Radiometric terminology has been loosely used in scientific research. Here, we specifically define radiometric terms used throughout this dissertation.

Solid angle – Ω, the projection of an area onto a unit sphere; measured in steradians (sr). A sphere has a 4π solid angle.

Projected area – the area projected onto a plane whose normal is the line of sight; the area is multiplied by the cosine of the angle between the normal to the area and the line of sight.

Optical power – P, also known as radiant flux; the flow of radiant energy per unit time; expressed in W/m^2.

Radiance – L, the optical power (or radiant flux) per unit projected area per unit solid angle; expressed in W/m^{2}sr.

Irradiance – $I = dP/d\Omega$, also known in this work as intensity; the flow of energy per unit area per unit time; expressed in W/m^2. The irradiance is proportional to the square of the amplitude of the electric field of an optical wave.

Spectral radiance – $L_\lambda = dL/d\lambda$, the distribution of radiance per unit wavelength; expressed in W/m^{2}srHz. The spectral radiance is meaningful by integrating it over a wavelength range.

Frequency – ν, the number of cycles per second; measured in Hz or sec^{-1}.

Optical wavenumber – $k = 2\pi/\lambda$, where λ is the wavelength of the optical wave.

Spatial wavenumber – κ, the inverse of a spatial scale length.

1.5 Organization

This dissertation is organized in four chapters detailing the theory, methodology, and analysis used to study techniques to mitigate the effects of atmospheric turbulence. Chapter 2 reviews both the physical nature of atmospheric turbulence and theories developed to characterize atmospheric turbulence. A framework for studying optical wave propagation through atmosphere turbulence, in strong and weak turbulence conditions, is presented. Chapter 3 involves an in depth study of aperture averaging in weak turbulence conditions. Aperture averaging models, experimental methodology,

and analysis of new experimental data are explained. Chapter 4 follows the organization of Chapter 3, but instead addresses aperture averaging in strong turbulence conditions. New experimental data in the strong turbulence region are analyzed and compared with available models. Chapter 5 studies and characterizes the performance enhancement of free space optical communication systems when nonimaging optics are integrated into the optical receiver. Chapter 6 summarizes the contributions of this work and addresses areas for future research.

Chapter 2

Optical Wave Propagation through Atmospheric Turbulence

2.1 The Atmosphere

Propagation of optical waves through the atmosphere is affected by atmospheric turbulence, scattering off aerosols, and atmospheric absorption. This thesis addresses the predominant cause of distortion of optical waves in the atmosphere, which is atmospheric turbulence. Atmospheric turbulence is a result of localized variations of temperature, humidity, and pressure in the atmosphere. These variations result in localized refractive index fluctuations, where each localized area of lower or higher refractive index is known as a turbulent eddy [1]. The refractive index of each individual eddy is not much greater than unity, but the cumulative effect of eddies over a 1 km path is great.

The refractive index of air at optical frequencies is,

$$n - 1 = 77.6\left(1 + \frac{7.52 \cdot 10^{-3}}{\lambda^2}\right)\left(\frac{p}{T}\right) \cdot 10^{-6} \tag{2.1}$$

where n is the total refractive index, λ is the wavelength in μm, p is the pressure in mb, and T is the temperature in K. At sea level, $n - 1$ is typically 3×10^{-4} [1]. Humidity effects are typically neglected over land, since humidity affects the value of the refractive index by less than 1%.

2.2 Turbulent Energy Flow

Turbulent flows result when large inertial forces draw together fluid volumes with very different velocities, and irregular velocity fluctuations are apparent. Turbulent flows exist when the Reynolds number is greater than 2500 to 5000 [12], where the Reynolds number is defined by:

$$Re = UL/\upsilon \tag{2.2}$$

where U is the characteristic flow velocity, L is the characteristic dimension of viscous flow, and υ is the kinematic viscosity of the fluid. Since Reynolds numbers in the atmosphere are large, the associated fluid flows are also highly unstable. Eddies of scale sizes on the order of flow dimensions move randomly, and eventually give rise to eddies of smaller scale sizes and lower velocities. Eventually, eddies become small enough that viscosity forces overcome inertial forces, and the eddies can no longer decay. The breakdown in eddies is dictated by [12],

$$Re^{(j)} = U^{(j)}L^{(j)}/\upsilon^{(j)} \tag{2.3}$$

where j is the order of the eddy. Higher orders denote smaller eddies.

Richardson first developed a picture of the turbulent energy redistribution in the atmosphere. The process is shown pictorially in Figure 2.1, with an energy input region, inertial subrange, and energy dissipation region. The dissipation rate ε is related to the velocity U_ℓ of an eddy with characteristic length ℓ by [12],

$$U_\ell \approx (\varepsilon\ell)^{1/3} \tag{2.4}$$

At large characteristic lengths ℓ, a portion of kinetic energy in the atmosphere is converted into turbulent energy [13]. When the characteristic length reaches a specified

outer scale length, L_o, energy begins to cascade. The energy of one eddy is progressively redistributed into eddies of smaller scales, until eddies reach a size equal to the inner scale length, ℓ_o. The inner scale length, or Kolmogorov microscale, is defined by,

$$\ell_o = 7.4\left(\upsilon^3/\varepsilon\right)^{1/4} \tag{2.5}$$

At the surface layer of the Earth, ℓ_o is typically on the order of 4 mm [12], and υ is typically 0.148 cm^2s^{-1} [13]. Kolmogorov proposed that in the inertial subrange, where $L_o > \ell > \ell_o$, turbulence is isotropic and may be transferred from eddy to eddy without loss. When the diameter of a decaying eddy reaches ℓ_o, the energy of the eddy is dissipated as heat energy through viscosity processes [13].

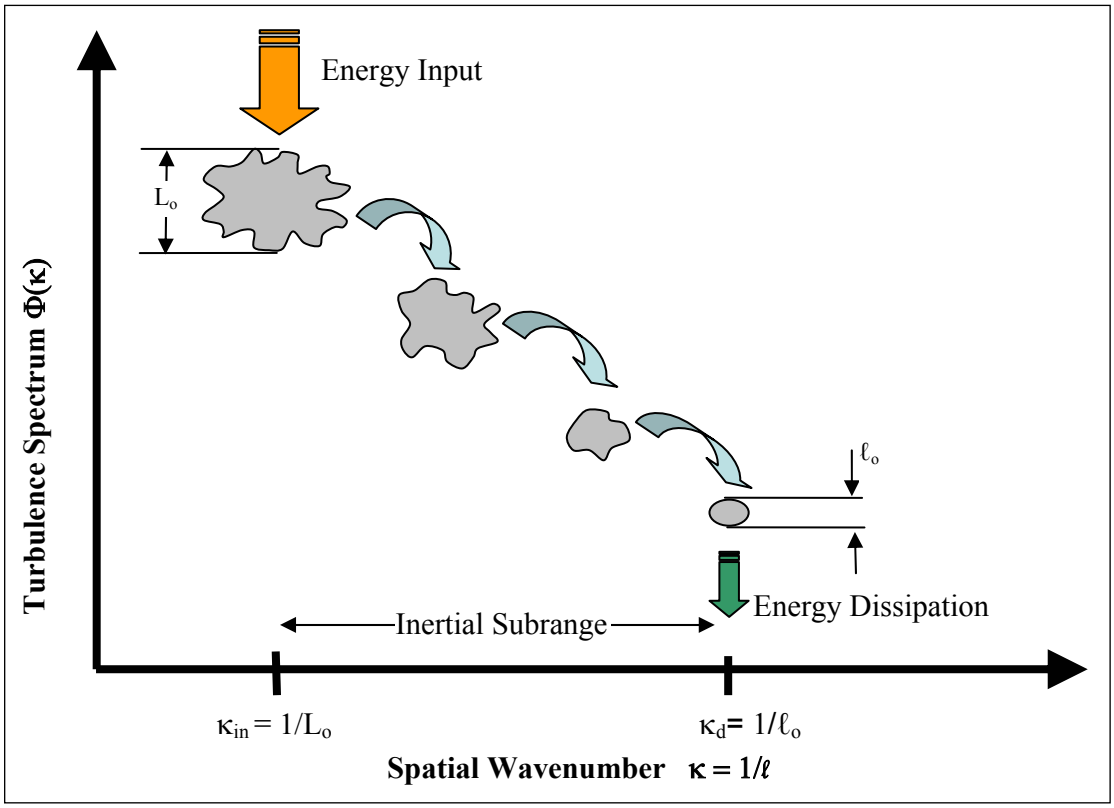

Figure 2.1: Depiction of the process of turbulent decay, showing the energy cascade and subsequent division of turbulent eddies in the atmosphere [adapted from Ref. 13].

2.3 Kolmogorov Turbulence

Turbulence is by nature a random process, and as such may be described using statistical quantities. In 1941, Kolmogorov first developed a universal description of atmospheric turbulence by developing a structure tensor to describe a mean square velocity difference between two points in the atmosphere. The structure function, $D_{ij}(\vec{r})$, is [1]:

$$D_{ij}(\vec{r}) = \left\langle \left[v_i(\vec{r}_1 + \vec{r}) - v_i(\vec{r}_1) \right] \cdot \left[v_j(\vec{r}_1 + \vec{r}) - v_j(\vec{r}_1) \right] \right\rangle \tag{2.6}$$

where $\vec{r}$ is the displacement between two points in space, $\vec{r}_1 + \vec{r}$ and $\vec{r}_1$ [1]; and *i* and *j* are two velocity components. To continue the structure function analysis, two approximations are made given the condition that the displacement is within the inertial subrange. The first is to assume local homogeneity in the atmosphere, which restricts the dependence of the velocity statistics in Eq. (2.6) to the vector displacement, $\vec{r}$. A second assumption of local isotropy limits Eq. (2.6) to a dependence on the magnitude of $\vec{r}$, given as $|\vec{r}|$. These assumptions allow the velocity structure function to be treated as a scalar function [1]:

$$D_{ij}(\vec{r}) = [D_{\parallel}(\vec{r}) - D_{\perp}(\vec{r})] n_i n_j - D_{\perp}(\vec{r}) \delta_{ij} \tag{2.7}$$

where $D_{\parallel}(\vec{r})$ and $D_{\perp}(\vec{r})$ are the structure function components of the wind velocity field parallel and transverse to $\vec{r}$, $\delta_{ij} \in \{1 \Rightarrow i = j; 0 \Rightarrow i \neq j\}$, and n_i, n_j are the components of a unit vector along $\vec{r}$ [1]. To continue this analysis, the flow is assumed to be incompressible, giving $\nabla \cdot \vec{v} = 0$. This assumption is valid when $\vec{v}^2 / a^2 << 1$,

where a is the velocity of sound [12]. Using the assumption of an incompressible flow, we can relate the parallel and transverse components of the velocity structure function:

$$D_{\perp} = \tfrac{1}{2r}\tfrac{d}{dr}\left(r^2 D_{\parallel}\right). \tag{2.8}$$

With this relation, we can describe the structure function in terms of one component:

$$D_{\parallel} = \left\langle \left[v_{\parallel}(r_1 + r) - v(r_1) \right]^2 \right\rangle \tag{2.9}$$

As mentioned previously, Kolmogorov determined that as long as r is within the inertial subrange, we can assume localized fluctuations and the structure function becomes [1]:

$$D_{\parallel} = C_v^2 r^{2/3} \tag{2.10}$$

where C_v^2 is the velocity structure constant with units $m^{-2/3}$. Eq. (2.10) is the Kolmogorov-Obukhov "two-thirds" power law [12]. To use this relation in electromagnetic wave propagation problems, the velocity fluctuation form of Eq. (2.10) must be transformed into a refractive index fluctuation form. This is accomplished by using the potential temperature, θ, which is the temperature of a parcel of air that is brought adiabatically (where heat is neither gained nor lost) from a state having pressure p and temperature T to a state where pressure p_0 = 1000 mbar [14]. For small values of r, as when r is in the inertial subrange, the potential temperature can be approximated by [15]:

$$\theta = T + \tfrac{g}{c_p} h \tag{2.11}$$

where T is the absolute temperature in Celsius, g is the acceleration of gravity, c_p is the specific heat, g/c_p = 9.8 °/km, and h is the height of the parcel above the Earth's surface [1,16]. The value g/c_p is also the adiabatic rate of decrease of the absolute

temperature. At small heights above the Earth's surface, the adiabatic rate g/c_p can be neglected and T is treated as a passive additive [1,16,17]. Passive additives to do not affect turbulence statistics, and therefore do not alter the two-thirds law in Eq. (2.10). The structure function for the potential temperature is well known [1], and is described by:

$$D_\theta(r) = C_\theta^2 r^{2/3} \tag{2.12}$$

By taking the derivative of both sides of Eq. (2.1) with respect to n, we find:

$$\partial n = 77.6\left(1 + \frac{7.52 \cdot 10^{-3}}{\lambda^2}\right)\left[\frac{p}{T}\left(\frac{\partial p}{p} - \frac{\partial T}{T}\right)\right] \tag{2.13}$$

Knowing that pressure fluctuations are relatively small compared to temperature fluctuations, we can approximate $\partial p \to 0$, giving:

$$\partial n = 77.6\left(1 + \frac{7.52 \cdot 10^{-3}}{\lambda^2}\right)\left(\frac{p}{T^2}\right)\partial T \cdot 10^{-6} \tag{2.14}$$

Using the relation of potential temperature to absolute temperature from Eq. (2.11), and the relation of their derivatives $\partial T = \partial\theta$ because T is a passive additive, we find that for $\lambda = 0.6328\mu m$:

$$\partial n = 79.06\left(\frac{p}{T^2}\right)\partial\theta \cdot 10^{-6} \tag{2.15}$$

The direct relationship between refractive index fluctuations and potential temperature fluctuations is shown in Eq. (2.16). We can now infer a relationship between the structure parameter for refractive index and that of the potential temperature as:

$$C_n^2 = 79.06\left(\frac{p}{T^2}\right)C_\theta^2 \cdot 10^{-6} \tag{2.16}$$

Optical refractive index fluctuations near the Earth's surface are a result of temperature variations [1]. C_n^2 is formally known as the refractive index structure parameter, and varies spatially and temporally. We use this indicator to quantify the strength of turbulence along the path of the optical propagation. The value of C_n^2 typically varies from 10^{-17} $m^{-2/3}$ under "weak turbulence" conditions to 10^{-13} $m^{-2/3}$ in "strong turbulence" conditions. Using previous information, the refractive index structure function obeys the same Kolmogorov-Obukhov "two-thirds" power law:

$$D_n(\vec{r}) = C_n^2 |\vec{r}|^{2/3} \tag{2.17}$$

2.4 Wavenumber Spectrum Models

By using a methodology similar to that used for the characterization of the strength of various frequency components in a time-varying electrical signal, we can define a Fourier transform to quantify the ability of different eddy sizes to influence the refractive index of a random medium. To develop a Fourier spectrum, we must first determine how refractive index fluctuations vary between different points in the atmosphere. This relationship is given by a spatial covariance [1,13]:

$$B_n(\vec{r}_1 + \vec{r}, \vec{r}_1) = \langle \delta n(\vec{r}_1 + \vec{r}) \delta n(\vec{r}_1) \rangle \tag{2.18}$$

where δn is the fluctuating part of the refractive index, with $n = \langle n \rangle + \delta n$. Following the previous discussion of Kolmogorov turbulence (Sec. 2.3), the assumption of homogeneity implies that only the separation between two points and not the location of the two points in a random medium affects the physics, so that $B_n(\vec{r}_1 + \vec{r}, \vec{r}_1) \to B_n(\vec{r})$. Near the Earth's surface, the random medium may be treated as isotropic, allowing

$B_n(\vec{r}) \to B_n(r)$. In spherical coordinates, the three-dimensional Fourier transform for the spatial covariance is:

$$\begin{aligned} B_n(r) &= \int d^3\vec{\kappa} \exp[i\vec{\kappa}\cdot\vec{r}]\Phi_n(\vec{\kappa}) \\ &= \int_{-\infty}^{\infty}\int_{0}^{\pi}\int_{0}^{2\pi} d\kappa\kappa^2 \sin(\theta) d\theta d\phi d\kappa \exp[i\vec{\kappa}\cdot\vec{r}]\Phi_n(\vec{\kappa}) \\ &= 4\pi\int_0^\infty d\kappa\kappa^2\Phi_n(\kappa)\frac{\sin(\kappa r)}{\kappa r} \end{aligned} \tag{2.19}$$

where $\Phi_n(\kappa)$ is the isotropic and homogeneous turbulence spectrum. A Fourier integral also relates the structure function to the isotropic and homogeneous turbulence spectrum:

$$D_n(r) = 8\pi\int_0^\infty d\kappa\kappa^2\Phi_n(\kappa)\left(1-\frac{\sin(\kappa r)}{\kappa r}\right) \tag{2.20}$$

which has been derived from the generic Fourier transform description of the spatial covariance and the definition of the refractive index structure function, $D_n(\bar{r}_1+\bar{r},\bar{r}_1) = \left\langle[\delta n(\bar{r}_1+\bar{r})-\delta n(\bar{r}_1)]^2\right\rangle$. The two descriptions of the refractive index structure function from Eqs. (2.17) and (2.20) may be compared to determine the wavenumber power spectrum:

$$C_n^2 r^{2/3} = 8\pi\int_0^\infty d\kappa\kappa^2\Phi_n(\kappa)\left(1-\frac{\sin(\kappa r)}{\kappa r}\right) \tag{2.21}$$

Using power law relations, the wavenumber spectrum is [1,3]:

$$\Phi_n(\kappa) = 0.033C_n^2\kappa^{-11/3} \tag{2.22}$$

Eq. (2.22) is the *Kolmogorov spectrum*. It is only valid in the range $1/L_o << \kappa << 1/l_o$. $\Phi_n(\kappa)$ is an equivalent representation of $D_n(r)$ in inverse space.

There are other spectrum models that attempt to describe behavior beyond the inertial subrange. The *Tatarskii spectrum* uses a Gaussian function to extend coverage to the dissipation range ($\kappa > 1/\ell_o$), where small eddies are influential:

$$\Phi_n(\kappa) = 0.033 C_n^2 \kappa^{-11/3} \exp\left(-\kappa / \kappa_m\right) \tag{2.23}$$

where $\kappa_m = 5.92/\ell_o$. The von Karman model is the most widely-used model to describe characteristics in the energy-input region ($\kappa < 1/L_o$). Although it does an excellent job of describing large eddy formation in the troposphere, the model was originally proposed to describe fluid flow in a circular pipe [18]. The *von Karman spectrum* integrates the small eddy dependence in the Tatarskii spectrum with a large eddy description to give:

$$\Phi_n(\kappa) = 0.033 C_n^2 \frac{\exp\left(-\kappa^2/\kappa_m^2\right)}{\left(\kappa^2 + \kappa_{in}^2\right)^{11/6}} \text{ for } 0 < \kappa < \kappa_m \tag{2.24}$$

where $\kappa_m = 5.92/\ell_o$ and $\kappa_{in} = 1/L_o$. In the inertial subrange, the von Karman spectrum reduces to the Kolmogorov spectrum value.

The Kolmogorov and von Karman spectrums fail to show a "bump" at high wavenumber values in the inertial subrange, near κ_m. Hill constructed an exact spectrum that accounts for the high wavenumber rise [19]. Andrews developed an analytical approximation to the Hill spectrum, since the Hill spectrum uses a second-order differential equation that has to be solved numerically. Andrews calls his approximation the *Modified Atmospheric Spectrum*, which has the representation [20]:

$$\Phi_n(\kappa) = 0.033 C_n^2 \left[1 + 1.802 \left(\frac{\kappa}{\kappa_l} \right) - 0.254 \left(\frac{\kappa}{\kappa_l} \right)^{7/6} \right] \times \frac{\exp\left(-\kappa^2 / \kappa_l^2 \right)}{\left(\kappa^2 + \kappa_{in}^2 \right)} \tag{2.25}$$

The Kolmogorov, von Karman, and modified atmospheric spectrums are plotted in Fig. 2.2 for scale sizes of L_o = 10 m and ℓ_o = 5 mm. The high wavenumber "bump" occurs in the transition between the inertial subrange and dissipation range. The bump occurs in the plot of the modified atmospheric spectrum at the boundary between the energy dissipation range and the inertial subrange in Fig. 2.2, and is especially apparent in the scaled spectral plot in Fig. 2.3.

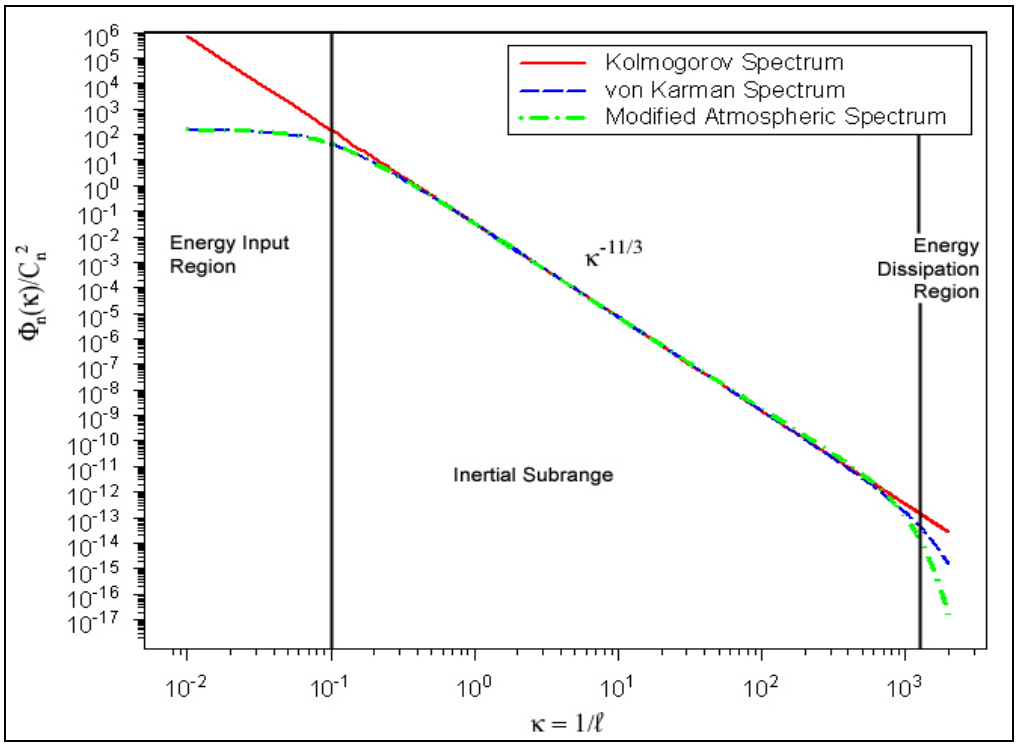

Fig. 2.2: Three wavenumber spectrum models for refractive index fluctuations. The three energy ranges relevant to turbulence statistics are indicated.

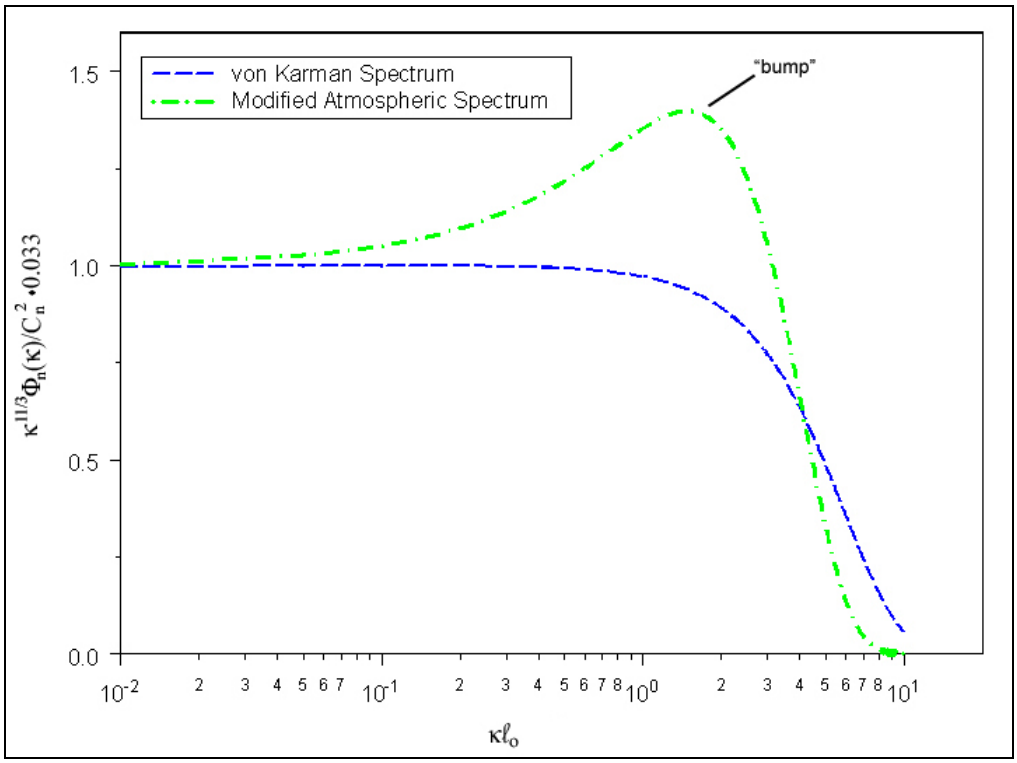

Fig. 2.3: Scaled spectral models for the von Karman spectrum, Eq. (2.24), and modified atmospheric spectrum, Eq. (2.25), plotted against the wavenumber scaled by the inner scale.

2.5 Rytov Approximation

The Rytov approximation is a method to solve Maxwell's equations for electromagnetic wave propagation while accounting for diffraction effects [1,21,22]. A derivation of optical wave propagation is begun from Maxwell's equations, assuming no free charges, μ_0 permeability, and an electromagnetic field with a harmonic time dependence of $e^{-j\omega t}$ [1,22]:

$$\begin{aligned}
&\nabla \cdot \vec{H}(\vec{r},t) = 0 \\
&\nabla \cdot \left[n(\vec{r},t)^2 \vec{E}(\vec{r},t) \right] = 0 \\
&\nabla \times \vec{H}(\vec{r},t) = -jk_0 n(\vec{r},t)^2 \vec{E}(\vec{r},t) \\
&\nabla \times \vec{E}(\vec{r},t) = jk_0 \vec{H}(\vec{r},t)
\end{aligned} \tag{2.26}$$

where $k_0 = \omega/c$ is the free space wavenumber, c is the speed of light in vacuum, n = $n(r)$ is the refractive index of the atmosphere, and $j = \sqrt{-1}$. It is also assumed that the variation of the field with time is much slower than $e^{-j\omega t}$, which justifies a quasi-steady state approach. After some manipulation with vector identities and substitution [1,22], a wave equation is found:

$$\nabla^2 \vec{E} + k^2 n^2 \vec{E} - 2\nabla\left(\vec{E} \cdot \nabla \ln(n)\right) = 0 \tag{2.27}$$

where the third term on the left hand side is a depolarization term. Since it has been shown that the change in polarization of a propagating wave is negligible for both cases of $\lambda << \ell_o$ and $\lambda > \ell_o$ [1], this term may be dismissed. Eq. (2.28) becomes:

$$\nabla^2 \vec{E} + k^2 n^2 \vec{E} = 0 \tag{2.28}$$

Eq. (2.28) may be transformed into a scalar equation for each of the three electric field components. Given a mean air refractive index of 1, the total refractive index is:

$$n(\vec{r}) = 1 + \delta n(\vec{r}) \tag{2.29}$$

where $\delta n << 1$. The Rytov method considers a solution of the form:

$$E(\vec{r}) = \exp(\Psi(\vec{r})) \tag{2.30}$$

Substitution of Eq. (2.30) into Eq. (2.29) yields the nonlinear Ricatti equation [22,23]:

$$\nabla^2 \Psi(\vec{r}) + \nabla\Psi(\vec{r}) \cdot \nabla\Psi(\vec{r}) = -k_0^2 \delta n^2(\vec{r}) \tag{2.31}$$

The Ricatti equation may be solved by a multiplicative perturbation method with a solution [22,23,45]:

$$\Psi(\vec{r}) = \Psi_0(\vec{r}) + \Psi_1(\vec{r}) + \Psi_2(\vec{r}) + \Psi_3(\vec{r}) + \ldots \tag{2.32}$$

The field equation for the basic Rytov solution is a result of keeping the first two terms in the expansion [22,23,45]:

$$\nabla^2\Psi_1(\vec{r}) + 2\nabla\Psi_0(\vec{r})\cdot\nabla\Psi_1(\vec{r}) = -2k_0^2\delta n(\vec{r}) \tag{2.33}$$

Amplitude and phase information for the propagating wave falls out of the Rytov approximation. The first iterative solution to Eq. (2.33) may be written as the perturbed field $U(\vec{r}) = U_0(\vec{r})\exp(\Psi_1(\vec{r}))$, where $U_0(\vec{r})$ is the unperturbed field [45]. Following Refs. [20] and [45], the complex phase perturbation is written as $\Psi_1(\vec{r}) = \chi + iS_1$ $= \ln(A/A_0) + i(S - S_0)$ where χ is the logarithm of the amplitude A, and S is the phase of the field $U(\vec{r})$. The unperturbed amplitude and unperturbed phase are denoted by A_0 and S_0, respectively. This analysis shows that under the Rytov approximation, irradiance fluctuations obey a lognormal distribution, since $\chi = \left[\ln(I/A^2)\right]/2$ [20,45]. The Rytov approximation yields a log amplitude variance $\langle\chi^2\rangle$ for infinite plane wave propagation [22,45]:

$$\langle\chi^2\rangle = \sigma_\chi^2 = 0.307C_n^2L^{11/6}k^{7/6} \tag{2.34}$$

It has been shown that Eq. (2.34) is a good approximation to the log amplitude variance in the range $\sigma_\chi^2 < 1$. The log intensity is related to the log amplitude variance by [1,45]:

$$\sigma_{\log I}^2 = \left\langle \left| \log I - \langle \log I \rangle \right|^2 \right\rangle = 4\sigma_\chi^2 \tag{2.35}$$

and

$$\sigma_{\log I}^2 = 1.23C_n^2L^{11/6}k^{7/6} = \sigma_R^2 \tag{2.36}$$

where σ_R^2 is the Rytov variance. The Rytov variance of an infinite plane wave helps to define the strength of irradiance fluctuations, although it is not an absolute measure of turbulence strength, as shown in Table 2.1.

Strength of Fluctuations	Rytov variance
Weak	$\sigma_R^2 < 0.3$
Intermediate	$\sigma_R^2 \sim 1$
Strong	$\sigma_R^2 >> 1$

Table 2.1: Typical Rytov variance ranges corresponding to weak, intermediate, and strong turbulence levels.

A better comparison of the strength of irradiance fluctuations is provided by the transverse coherence length for a optical wave [13,24]. The coherence length for a plane wave is:

$$\rho_0 = \left(1.46k^2 LC_n^2\right)^{-3/5} \tag{2.37}$$

The coherence length for a spherical wave is:

$$\rho_0 = \left(0.546Lk^2 C_n^2\right)^{-3/5} \tag{2.38}$$

Fried defined a coherence radius $r_0 = 2.099\rho_0$ where ρ_0 is defined in Eq. (2.38) [25,1].

A better way to determine the region of turbulence experienced by a propagating optical wavefront is to plot the three relevant scale sizes: the transverse coherence length, ρ_0, the Fresnel zone size, $\sqrt{\lambda z}$, and the scattering disk size, $L/k\rho_0$. These are plotted in Fig. 2.3 for the plane wave case with $C_n^2 = 5\times10^{-14}$ m$^{-2/3}$, Fig. 2.4 for the spherical wave case with $C_n^2 = 5\times10^{-15}$ m$^{-2/3}$, and Fig. 2.5 for the spherical wave case with $C_n^2 = 5\times10^{-13}$ m$^{-2/3}$. The intersection of the three scale sizes denotes the onset of strong scintillation [19].

Eq. (2.37) is bounded by inner scale and outer scale scattering parameters, since optical propagation in the visible and near-infrared wavelengths near the Earth's surface is dominated by Fresnel scattering [21]. The large eddies in the spectrum set the outer scale scattering parameter:

$$\zeta_0 = 2\pi L\lambda / L_0^2 \tag{2.39}$$

while the small eddies define the inner scale scattering parameter:

$$\zeta_m^2 = \frac{L\kappa_m^2}{k} = 5.56\frac{L\lambda}{\ell_0^2} \tag{2.40}$$

For a test range length of L = 863 m and a wavelength λ = 0.6328 μm, the Fresnel length is 2.47 cm, which is well away from the scale of either scattering parameter.

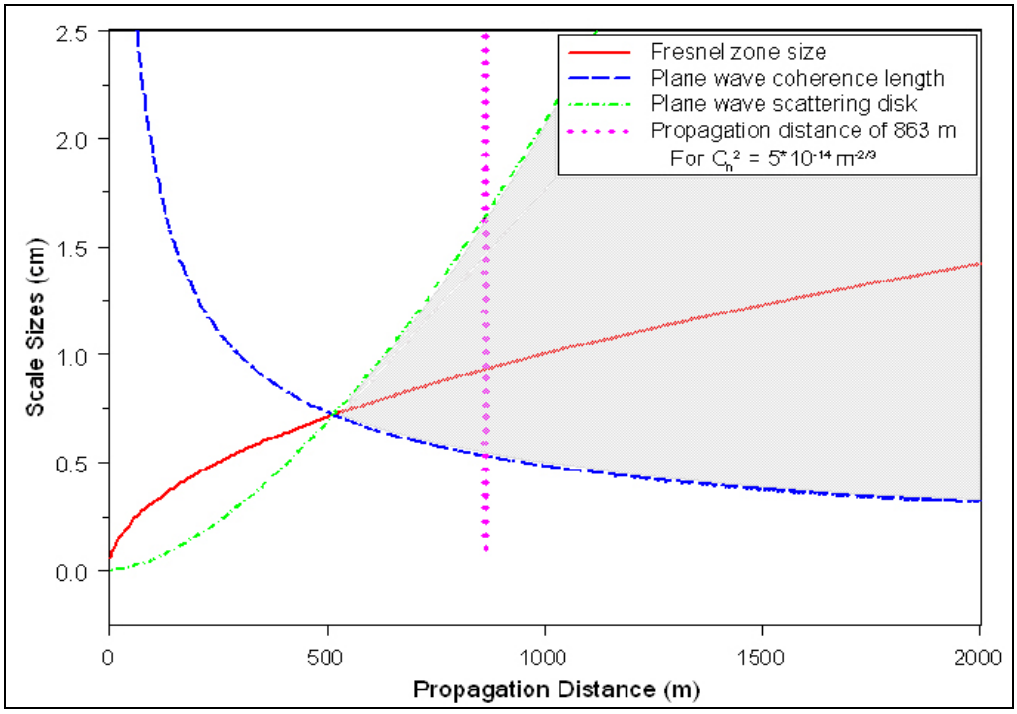

Fig. 2.4: The Fresnel zone size, coherence length, and scattering disk size plotted for a plane wave against propagation distance. For L = 863 m, there are scale sizes on the link contributing to strong fluctuations. The shaded area shows scale sizes that do not contribute to strong fluctuations.

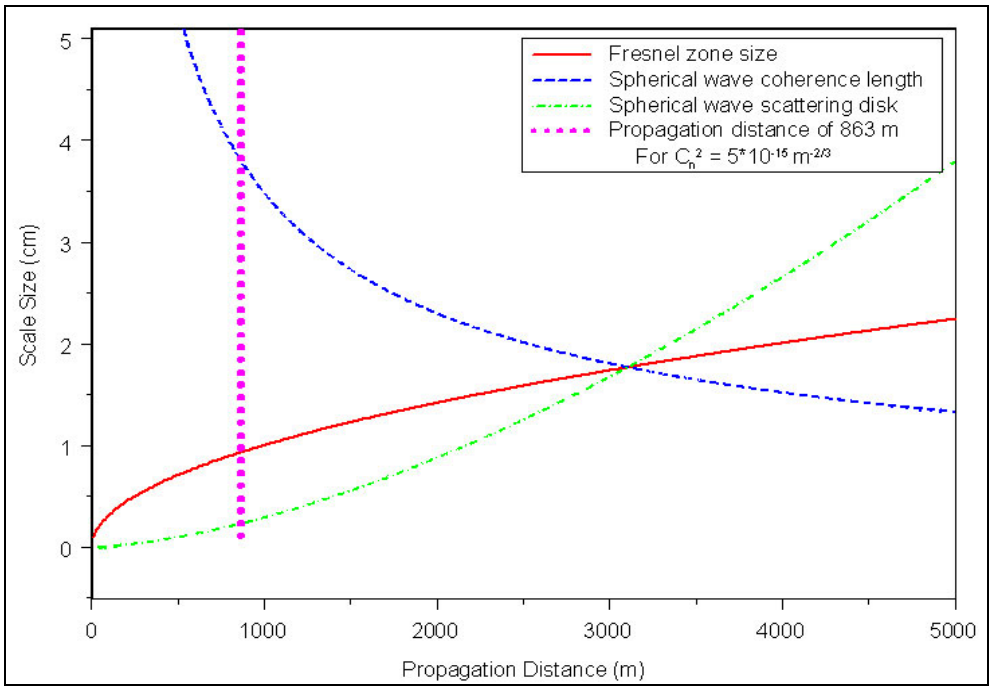

Fig. 2.5: Three scale sizes plotted against the propagation distance for the spherical wave case with $L = 863$ m. When $C_n^2 = 5\times10^{-15}$ m$^{-2/3}$, the wavefront sees weak scintillations with contributing scale sizes on the order of the Fresnel zone size.

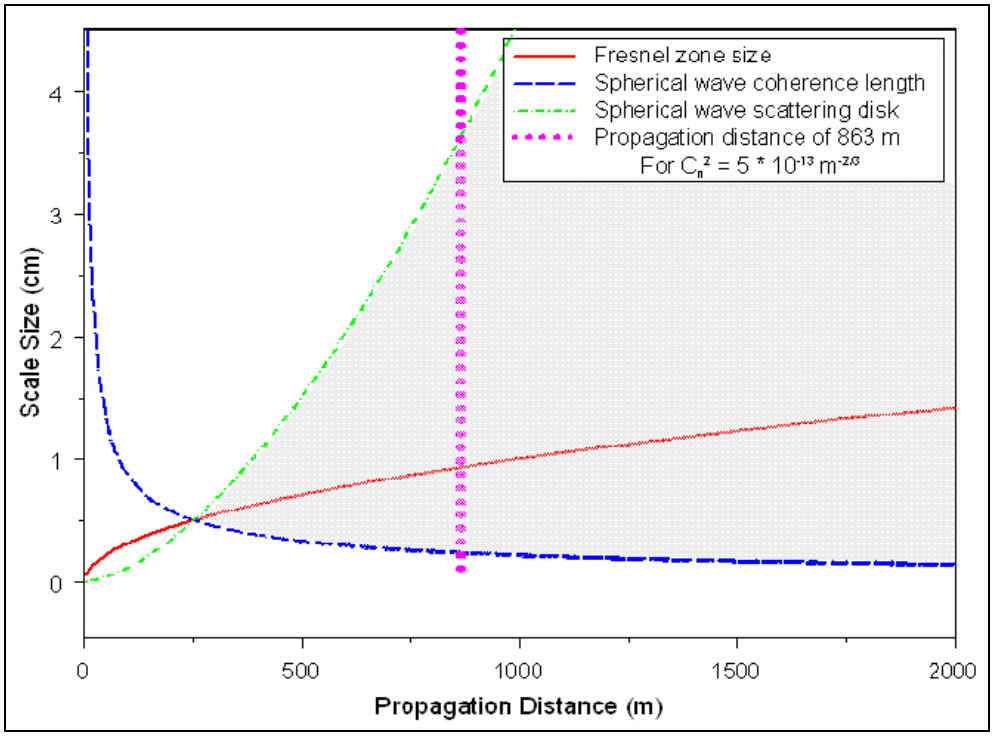

Fig. 2.6: Three scale sizes plotted against the propagation distance for the spherical wave case with $L = 863$ m. From the graph, the wavefront experiences strong fluctuations when $C_n^2 = 5\times10^{-13}$ m$^{-2/3}$, with contributing scale sizes beyond the shaded area.

2.6 Strong Turbulence Theory

Multiple scattering of an optical wave by refractive index inhomogeneities results in strong fluctuations of the irradiance. As the amount of multiple scattering increases with increasing propagation path length, irradiance fluctuations saturate and approach a value of one. This phenomenon was first experimentally reported in a Russian journal by Gracheva and Gurvich [26]. Although Rytov and other Markov based solutions to the stochastic wave equation were investigated [27], no existing analysis method was successful in describing the saturation of scintillation. New research in perturbation theory led to the development of the asymptotic theory for strong scintillations [27,28,29,30]. Other scientists used heuristic methods to predict the saturation of amplitude fluctuations [31,32]. Although the heuristic methods show good results, there is no well-defined relationship between amplitude and irradiance fluctuations in strong turbulence. Heuristic theory will not be used in the analysis of aperture averaging, since the analysis requires information of the value of the logarithm of the amplitude.

2.6.1 Andrews – Prokhorov Asymptotic Analysis

The propagation of an optical wave is defined by different moments of the field. The angular spread of the beam is characterized by the second order moment, which is known as the mutual coherence function (MCF). The fourth order moment defines the irradiance fluctuations of the propagating wave. When the propagating wavelength is small compared to the scale size of inhomogeneities in the random medium, and the variation of the refractive index is much less than one, the fourth order moment with $\vec{E}$ in the $\hat{z}$ propagation direction is [27,29]:

$$\Gamma_4(z,r_1,r_2)=\left\langle E(z,r_1)E(z,r_2)E^*(z,0)E^*(z,r_1+r_2)\right\rangle \tag{2.41}$$

The irradiance variance is related to the fourth order moment by [29]:

$$\sigma_I^2=\left\langle\left(I-\langle I\rangle\right)^2\right\rangle=\Gamma_4(z,0,0)-1 \tag{2.42}$$

With the lack of an analytical solution to Eq. (2.42), asymptotic solutions for the fourth order moment yield the best results for strong turbulence over long propagation paths. Prokhorov summarized the development of asymptotic analysis using the local method of small perturbations [27]. He constructed a set of equations for the averaged field to which the moments of the field were solutions. The local method of small perturbations required that the phase of the fluctuating wave experiences only small variations over a propagating distance $z-z_0$, and satisfies the limit:

$$k^2\left\langle\Delta\varepsilon^2\right\rangle\ell^2<<1 \tag{2.43}$$

where $2\Delta\varepsilon=\left(\varepsilon-\langle\varepsilon\rangle\right)/\langle\varepsilon\rangle$ and ℓ is the scale of the inhomogeneities in the turbulent medium.

2.6.1.1 Andrews Asymptotic Analysis for a Plane Wave

The equation for the fourth-order moment of the electric field of a plane wave propagating in a statistically homogeneous random medium is [27]:

$$\frac{\partial\Gamma_4}{\partial z}=-V\Gamma_4-\left(i/k\right)\frac{\partial^2\Gamma_4}{\partial\vec{r}_1\partial\vec{r}_2} \tag{2.44}$$

with

$$V=D'(\vec{r}_1)+D'(\vec{r}_2)-\frac{D'(\vec{r}_1+\vec{r}_2)}{2}-\frac{D'(\vec{r}_1-\vec{r}_2)}{2} \tag{2.45}$$

where Γ_4 is the fourth moment of the field and $D'(u)$ is the derivative of the phase structure function. Prokhorov wrote the spectral function of irradiance fluctuations as [27]:

$$M(z,\vec{q},\vec{r}_2)=\frac{1}{2\pi}\int d\vec{u}\,\exp[-i\vec{q}\vec{u}]\Gamma_4(z,\vec{r}_1,\vec{r}_2) \tag{2.46}$$

which is the Fourier transform of the fourth order moment with q representing the scale of frequency components in the spectrum. The full power spectrum in the strong fluctuation regime is presented in Eq. (4.17) of Ref. [27]. In his analysis, Prokhorov derived the scintillation index, m^2, or irradiance variance, in strong, saturated turbulence conditions [27]:

$$\sigma_I^2 = m^2 = 1 + N_3(\alpha)\left\{D\left(\sqrt{z/k}\right)\right\}^{-(2/\alpha)(2-\alpha)} \quad \text{for } D\left(\sqrt{z/k}\right) >> 1 \tag{2.47}$$

where

$$N_3(\alpha)=\frac{2^{(\alpha+1)}}{\pi\alpha}\sin\left(\frac{\pi\alpha}{2}\right)\Gamma^2\left(1+\alpha/2\right)\Gamma\left(4/\alpha-1\right)\left(\frac{1}{\alpha-1}\right) \times {}_2F_1\left\{4/\alpha-1,\alpha-1;\alpha;\alpha/(\alpha+1)\right\} \tag{2.48}$$

where α is the power-law exponent of the phase structure function, $D(u)=C(ku)^{\alpha}$, Γ represents the gamma function, and ${}_2F_1$ is the confluent hypergeometric function. The phase structure function in the inertial subrange approximates a 5/3 power relation [13]. For α = 5/3, $N_3(\alpha)$ = 1.22. A solution to the scintillation index can be found using the phase structure function representation [27]:

$$D(r)=2.9C_n^2k^3zr^{5/3} \tag{2.49}$$

By substituting this into Eq. (2.47), we find the asymptotic relation between the scintillation index and the Rytov variance for a plane wave in saturated strong turbulence [20,27]:

$$\sigma_I^2 = 1 + \frac{0.86}{\left(\sigma_R^2\right)^{2/5}} \tag{2.50}$$

For the duration of this thesis, we will refer to Eq. (2.50) as the Andrews asymptotic model for the plane wave case.

The generalized asymptotic form for the covariance may also be written in terms of the transverse coherence length [24,11]. The form of the covariance for a plane wave is given by a two-scale model:

$$C_I(\rho) = \exp\left[-\left(\frac{\rho}{\rho_0}\right)^{5/3}\right] + \frac{1}{2}N_3\left(\tfrac{5}{3}\right)\left(\frac{k\rho_0^2}{L}\right)^{1/3}\left[b_1(\rho) + b_2(\rho)\right] \tag{2.51}$$

where b_1 and b_2 are scale functions that represent the influence of two different scale sizes on the propagating wave. When ρ approaches zero, b_1 and b_2 go to unity; while as ρ approaches infinity, b_1 and b_2 go to zero. When $\rho \to 0$, Eq. (2.51) becomes the asymptotic form of the irradiance variance in Eq. (2.50), as expected.

2.6.1.2 Andrews Asymptotic Analysis for the Spherical Wave

In spherical coordinates, the fourth-order moment of the electric field for a propagating spherical wave in a statistically homogeneous random medium is [27]:

$$\frac{\partial \Gamma_4}{\partial r} = -V\Gamma_4 - \left(\frac{i}{kr^2}\right)\left\{\frac{\partial^2 \Gamma_4}{\partial \xi_\theta \partial \eta_\theta} + \frac{\partial^2 \Gamma_4}{\partial \xi_\phi \partial \eta_\phi}\right\} \tag{2.52}$$

where (r,θ,ϕ) are spherical coordinates with (ξ_θ,ξ_ϕ) and (η_θ,η_ϕ) are constant differences in angular coordinates due to the conversion from cartesian to spherical coordinates. In the region of the interest of the fourth moment, the angles of interest, (ξ_θ,ξ_ϕ) and (η_θ,η_ϕ), are small and near the equator of the spherical coordinate system with $\theta \approx \pi/2$ [27]. Therefore, due to the small angles in the second derivative on the right hand side of Eq. (2.52), there will be an additional constant factor in the term. In saturated strong turbulence, the scintillation index is [27]:

$$\sigma_I^2 = m_{sp}^2 = 1 + N_{sp}(\alpha)\left\{D_{sp}\left(\sqrt{r/k}\right)\right\}^{(2/\alpha)(2-\alpha)} \tag{2.53}$$

with the spherical wave structure function related to the plane wave structure function in Eq. (2.49) by [27]:

$$D_{sp}(u) = (\alpha+1)^{-1} D(u) \tag{2.54}$$

and

$$\begin{aligned} N_{sp}(\alpha) = \left[\frac{2^{\alpha+1}}{\pi\alpha}\right](\alpha+1)\sin(\alpha\pi/2)\Gamma^2(1+\alpha/2) \\ \times\Gamma\left(\frac{4}{\alpha}-1\right)\Gamma^2(\alpha-1)\Gamma^{-1}(2\alpha-2) \end{aligned} \tag{2.55}$$

The spherical wave scintillation index is related to the plane wave phase structure function by [27]:

$$\sigma_I^2 = m_{sp}^2 = 1 + N_{3,sp}(\alpha)\left\{D\left(\sqrt{r/k}\right)\right\}^{(2/\alpha)(2-\alpha)} \tag{2.56}$$

where we have defined $N_{3,sp}$ as:

$$N_{3,sp}(\alpha) = (\alpha+1)^{(2/\alpha)(2-\alpha)} N_{sp}(\alpha) \tag{2.57}$$

As for the plane wave, we assume the phase structure function obeys a 5/3 power law in the inertial subrange, giving $N_{3,sp}(5/3) = 3.86$. The asymptotic scintillation index for a spherical wave in saturated strong turbulence conditions with $\alpha = 5/3$ becomes [20,27]:

$$\sigma_I^2 = 1 + \frac{2.73}{\left(\sigma_R^2\right)^{2/5}} \tag{2.58}$$

The asymptotic formula for the covariance of a spherical wave is of the same form as the two-scale model given by Eq. (2.51), with the spherical values for N_3, ρ_0, b_1, and b_2 used. Throughout the rest of this thesis, we will refer to Eq. (2.58) as the Andrews asymptotic model for the spherical wave for convenience.

2.6.2 Churnside Asymptotic Analysis

After the phenomenon of saturation of scintillation was understood, Churnside built upon Fried's work and published the first significant application of asymptotic theory to the study of aperture averaging. Churnside used the covariance function in Eq. (2.48) to devise a framework to study intensity scintillations when the inner scale is small.

2.6.2.1 Churnside Asymptotic Analysis for the Plane Wave

Churnside evaluated the two-scale model of the covariance function by representing the two scale functions, b_1 and b_2, as:

$$\begin{aligned} b_1(\rho) &= \frac{7}{3}\int_0^1 dx x^{4/3} J_0\left(k\rho\rho_0 x / L\right) \\ b_2(\rho) &= \exp\left[-\left(\frac{\rho}{\rho_0}\right)^{5/3}\right] \end{aligned} \tag{2.59}$$

Both functions go to unity when ρ approaches zero, and go to zero when ρ approaches infinity. Churnside's scale functions are compact forms of the functions presented in Chapter 3 of Ref. [1]. Different authors have evaluated these equations under different constraints [1,29], and Churnside uses limits relevant to aperture averaging. Based on Eq. (2.59), Churnside calculated the irradiance variance to be:

$$\sigma_I^2 = C_I(0) = 1 + 1.22\left(\frac{k\rho_0^2}{L}\right)^{1/3} \tag{2.60}$$

or, in terms of the plane wave Rytov variance:

$$\sigma_I^2 = 1 + \frac{1.14}{\left(\sigma_R^2\right)^{2/5}} \tag{2.61}$$

The Churnside asymptotic approximation is slightly different from that of Sec. 2.6.1.

2.6.2.2 Churnside Asymptotic Analysis for the Spherical Wave

The two-scale model of the covariance function in Eq. (2.51) is evaluated using Churnside's spherical wave representations for b_1:

$$b_1(\rho) = 0.915\int_0^1 dx x^{-1/3}(1-x)^2 \int_0^\infty d\tau \tau^{4/3} J_0\left(\frac{k\rho\rho_0\tau}{L}\right) \times \exp\left[-r^{5/3}(1-x)^{5/3}\right] \tag{2.62}$$

where b_2 is the same as in the plane wave case. The Churnside asymptotic equation for the irradiance variance of a spherical wave is:

$$\sigma_I^2 = 1 + 3.86\left(\frac{k\rho_0^2}{L}\right)^{1/3} \tag{2.63}$$

or, in terms of the plane wave Rytov variance:

$$\sigma_I^2 = 1 + \frac{5.35}{\left(\sigma_R^2\right)^{2/5}} \tag{2.64}$$

The multiplicative constant is slightly higher by Churnside's calculation, compared to the earlier theory in Section 2.6.1.

2.7 Irradiance Variance Models Valid in Both Weak and Strong Turbulence Conditions

2.7.1 Scintillation Index Model for a Plane Wave

Andrews and Philips developed a model to describe plane wave characteristics over the entire range of fluctuation conditions, from weak to strong turbulence [33]. They use the effective Kolmogorov spectrum, which modifies the Kolmogorov spectrum by two filter functions that exclude mid-scale sizes that have an insignificant effect on the propagating wave in the moderate-to-strong turbulence region. The effective Kolmogorov spectrum model is [20,33]:

$$\Phi_{n,\ell}(\kappa) = 0.033 C_n^2 \kappa^{-11/3} \left[G_x(\kappa) + G_y(\kappa) \right] \tag{2.65}$$

where the large-scale filter function that passes only spatial frequencies $\kappa < \kappa_x$ is:

$$G_x(\kappa) = \exp\left(-\frac{\kappa^2}{\kappa_x^2} \right) \tag{2.66}$$

and the small-scale filter function, passing only spatial frequencies $\kappa > \kappa_y$, is:

$$G_y(\kappa) = \frac{\kappa^{11/3}}{\left(\kappa + \kappa_y\right)^{11/6}} \tag{2.67}$$

The wavenumber spectrum given by Eq. (2.65) is a two-scale model for generic scale sizes *x* and *y*. Likewise, modified Rytov theory may be used to define the scintillation index, σ_I^2, in terms of large-scale and small-scale scintillations [20,33]:

$$\sigma_I^2 = \exp\left(\sigma_{\ln x}^2 + \sigma_{\ln y}^2\right) - 1 \tag{2.68}$$

where $\sigma_{\ln x}^2$ and $\sigma_{\ln y}^2$ are the large-scale and small-scale log irradiance fluctuations. These functions are evaluated in Ref. [33], to define the scintillation index for a plane wave, excluding inner scale effects, as:

$$\sigma_I^2 = \exp\left[\frac{0.49\sigma_R^2}{\left(1+1.11\sigma_R^{12/5}\right)^{7/6}} + \frac{0.51\sigma_R^2}{\left(1+0.69\sigma_R^{12/5}\right)^{5/6}}\right] - 1 \tag{2.69}$$

where σ_R^2 is the Rytov variance for a plane wave. Eq. (2.69) reduces to the Rytov approximation in weak turbulence conditions, and the asymptotic model from Eq. (2.58) in strong turbulence saturation conditions.

2.7.2 Scintillation Index Model for a Spherical Wave

The scintillation index (SI) model attempts to describe the behavior of irradiance fluctuations over the entire range of turbulence strengths. The model for a spherical wave is developed using the effective Kolmogorov spectrum, using the same two-scale filter functions presented in Eqs. (2.66) and (2.67) for the plane wave case. The small scale and large scale log irradiance fluctuations are evaluated to define the scintillation index of a spherical wave, neglecting inner scale effects, by [20,33]:

$$\sigma_I^2 = \exp\left[\frac{0.20\sigma_R^2}{\left(1+0.19\sigma_R^{12/5}\right)^{7/6}} + \frac{0.20\sigma_R^2}{\left(1+0.23\sigma_R^{12/5}\right)^{5/6}}\right] - 1 \tag{2.70}$$

where σ_R^2 is the plane wave Rytov variance. Eq. (2.70) has the same form as Eq. (2.69), when we rewrite Eq. (2.69) using the relation between the spherical wave and plane wave Rytov variances $\sigma_{R,sph}^2 = 0.4\sigma_R^2$.

2.7.3 Scintillation Index Model using the Atmospheric Spectrum

The modified atmospheric spectrum is useful when accounting for the influence of the inner scale, ℓ_o, in the calculation of the irradiance variance. The spectrum is still represented by a two scale model, with an enhanced description of the large-scale filter function integrated into the model. In order to properly account for the influence of the inner scale, the new large-scale filter function is defined as [20]:

$$\begin{aligned} G_x(\kappa,\ell_o) &= f(\kappa\ell_o)\exp\left(-\kappa^2/\kappa_x^2\right) \\ &= \left\{\exp\left(\frac{-\kappa^2}{\kappa_l^2}\right)\left[1+1.80\left(\frac{\kappa}{\kappa_l}\right)-0.25\left(\frac{\kappa}{\kappa_l}\right)^{7/6}\right]\right\} \\ &\quad\times\exp\left(\frac{-\kappa^2}{\kappa_x^2}\right) \end{aligned} \tag{2.71}$$

where the term in the {} arises out of the modified atmospheric spectrum in Eq. (2.25). The small-scale filter function has the same form as in Eq. (2.67). Eqs. (2.71) and (2.67) may be combined to form the *Effective Atmospheric Spectrum*, which is an extension of the modified atmospheric spectrum [20]:

$$\Phi_n(\kappa) = 0.033C_n^2\kappa^{-11/3}\left[G_x(\kappa,\ell_o)+G_y(\kappa)\right] \tag{2.72}$$

The irradiance variance of a spherical wave using the spectrum in Eq. (2.72) may be broken down into components attributed to the modified atmospheric spectrum and effective atmospheric spectrum [20]:

$$\sigma_I^2\left(D,\ell_o\right)=\exp\left[\sigma_{\ln x}^2\left(D,\ell_o\right)+\frac{0.51\sigma_{mas}^2\left(1+0.69\sigma_{mas}^{12/5}\right)^{-5/6}}{1+0.9d^2\left(\frac{\sigma_{R,sp}^2}{\sigma_{mas}^2}\right)^{6/5}+0.62d^2\sigma_{R,sp}^{12/5}}\right]-1 \tag{2.73}$$

where $d=\sqrt{kD^2/4L}$. The components of Eq. (2.68) are defined in Eqs. (2.71) through (2.74). The spherical wave Rytov variance is given by:

$$\sigma_{R,sp}^2=0.497C_n^2k^{7/6}L^{11/6} \tag{2.74}$$

The scintillation index using the modified atmospheric spectrum in weak turbulence is [20]:

$$\sigma_{mas}^2\cong 9.65\sigma_{R,sp}^2\left\{0.4\left(1+9/Q_l^2\right)^{11/12}\left[\sin\left(\frac{11}{6}\tan^{-1}\frac{Q_l}{3}\right)+\frac{2.61}{\left(9+Q_l^2\right)^{1/4}}\sin\left(\frac{4}{3}\tan^{-1}\frac{Q_l}{3}\right)-\frac{0.52}{\left(9+Q_l^2\right)^{7/24}}\sin\left(\frac{5}{4}\tan^{-1}\frac{Q_l}{3}\right)\right]-\frac{3.50}{Q_l^{5/6}}\right\} \quad \text{for } \sigma_{R,sp}^2<1 \tag{2.75}$$

where $Q_l=10.89L/k\ell_o^2$. In saturated strong turbulence, the scintillation index becomes [20]:

$$\sigma_{mas}^2\cong 1+\frac{6.57}{\left(\sigma_{R,sp}^2Q_l^{7/6}\right)^{1/6}},\quad \text{for } \sigma_{R,sp}^2>>\frac{100}{Q_l^{7/6}} \tag{2.76}$$

Either Eq. (2.75) or Eq. (2.76) may be used in Eq. (2.73) depending on the strength of turbulence experienced on the link. Finally, the part of the scintillation index resulting from the effective atmospheric spectrum, $\sigma_{\ln x}^2\left(D,\ell_o\right)$, in Eq. (2.73) is defined by [20]:

$$\sigma_{\ln x}^2\left(D,\ell_o\right)=0.04\sigma_{R,sp}^2\left(\frac{\eta_{xd}Q_l}{\eta_{xd}+Q_l}\right)^{7/6}\times\left[1+1.75\left(\frac{\eta_{xd}}{\eta_{xd}+Q_l}\right)^{1/2}-0.25\left(\frac{\eta_{xd}}{\eta_{xd}+Q_l}\right)^{7/12}\right] \tag{2.77}$$

where

$$\eta_{xd}=\frac{8.56}{1+0.18d^2+0.20\sigma_{R,sp}^2Q_l^{1/6}} \tag{2.78}$$

Although Eq. (2.73) may be used to quantify the effects of the inner scale ℓ_o on the irradiance variance, it is generally accepted that ℓ_o has little effect on the strong turbulence irradiance variance [20]. As such, the scintillation index model using the atmospheric spectrum presented in Eq. (2.73) will only be used in conjunction with weak turbulence analysis.

Chapter 3

Aperture Averaging in Weak Turbulence

3.1 Introduction

As electromagnetic waves propagate through the atmosphere, they undergo refraction by turbulent eddies. They eddies are characterized by localized variations in refractive index from the mean. As a propagating wave moves through these eddies, spatially and temporally random irradiance patterns are formed. When a portion of the wave reaches a receiver, the receiver aperture will average across all of these random spatial fluctuations unless the aperture is smaller than the spatial scale of the fluctuations. This phenomenon is called aperture averaging. The aperture averaging factor of the receiver is defined as the ratio of the irradiance fluctuations seen at a receiver with diameter D, to those fluctuations seen by a point receiver (or a receiver that is small enough to approximate a point receiver).

Aperture averaging theory has been extensively developed for plane and spherical waves in weak turbulence conditions [1,10,11,16,21,24,33]. Minimal theory is available for the strong turbulence regime [20,24]. There has been some previous experimental work [10,11], but early experiments did not account for scintillation saturation, and resulted in data markedly different from that predicted by theory. Later experiments did not sufficiently account for background light, and were limited by the short path lengths under investigation[11].

Aperture averaging of optical scintillations is an essential consideration in any receiver telescope design. Incorporating aperture averaging techniques helps optimize optical receiver designs; in that a larger aperture will collect more incoming radiation and reduce the likelihood of fading on an optical communications link. In this chapter, an experiment to quantify the system enhancement of an aperture averaged receiver is conducted. This experiment is built upon the theoretical foundation presented in Chapter 2. A description of the methodology of this experiment is followed by a presentation and discussion of experimental results.

3.2 Data Analysis for Weak Turbulence

3.2.1 General Aperture Averaging Form

The generic form of the aperture averaging factor for a circular aperture with diameter D is [10,11]:

$$A = \frac{\sigma_I^2(D)}{\sigma_I^2(0)} = \int_0^D \frac{C_I(r)}{C_I(0)} \left[\frac{16}{\pi D^2} \left(\cos^{-1}\left(\tfrac{r}{D}\right) - \tfrac{r}{D}\left(1 - \tfrac{r^2}{D^2}\right)^{1/2} \right) \right] r\,dr \qquad (3.1)$$

where r is the distance between two points on the aperture surface, $C_I(r)$ is the spatial covariance of the irradiance, $C_I(0)$ is the variance of the irradiance, and the term in the square brackets is the modulation transfer function (MTF) of the circular aperture.

3.2.2 Weak Turbulence

Weak turbulence was defined in Fig. 2.4 as the case when the transverse coherence length of the received wave is much larger than the Fresnel length. The covariance of the irradiance is [11]:

$$C_I(r) = 16\pi^2 k^2 \int_0^\infty d\kappa \kappa \Phi_n(\kappa) \int_0^L dz J_0(\kappa r s) \sin^2\left[\frac{\kappa^2 (L-z)s}{2k}\right] \quad (3.2)$$

where $k = 2\pi/\lambda$, $\Phi_n(\kappa)$ is the wavenumber spectrum, z is the distance traveled over path length L, J_0 is a Bessel function of the first kind, and s is a scaling factor that is 1 for a plane wave and z/L for a spherical wave.

3.2.2.1 Plane Wave, Small ℓ_o

To calculate the covariance values necessary to input into the aperture averaging factor equation, the Kolmogorov spectrum in Eq. (2.22) may be used since the inner scale is much smaller than the Fresnel length, $\ell_o << (L/k)^{1/2}$. After the Kolmogorov spectrum is substituted into Eq. (3.2), and we assume a point receiver with $r = 0$, the variance of the irradiance is found as [11]:

$$C_I(r=0) = 1.23 C_n^2 k^{7/6} L^{11/6} = \sigma_I^2 \equiv \sigma_R^2 \quad (3.3)$$

The exact aperture averaging factor for a plane wave is [11]:

$$\begin{aligned} A = 21.6 k^{5/6} L^{-11/6} \int_0^\infty d\kappa \kappa^{-8/3} \int dz \sin^2\left[\frac{\kappa^2 (L-z)}{2k}\right] \times \\ \int_0^1 J_0(\kappa D y)\left[\cos^{-1} y - y(1-y^2)^{1/2}\right] y dy \end{aligned} \quad (3.4)$$

The inner integral of the Bessel function is given by $\pi J_1^2(\kappa D/2)/\kappa^2 D^2$. After a change of variables to let $u = \kappa D/2$, A becomes solely a function of $(kD^2/4L)^{1/2}$ [11]:

$$A = 8.47\left(\frac{kD^2}{4L}\right)^{5/6} \int u^{-14/3} J_1^2(u)\left[1 - \frac{kD^2}{4Lu^2}\sin\left(\frac{4Lu^2}{kD^2}\right)\right] du \quad (3.5)$$

It is seen that for a small receiver aperture, when $kD^2/4L << 1$, A approaches one as expected. For large apertures, when $kD^2/4L >> 1$, the sine term is small and may be replaced by the expansion $\sin\gamma \approx \gamma - \gamma^3/6$, so that [11]:

$$A \approx 1.41\left(\frac{kD^2}{4L}\right)^{-7/6}\int_0^\infty u^{-2/3}J_1^2(u)du = 0.932\left(\frac{kD^2}{4L}\right)^{-7/6} \tag{3.6}$$

The $D^{-7/3}$ dependence indicates that the scattering due to turbulence is over a small angle. The light will not be scattered wide enough to miss the receiver aperture entirely. The total aperture averaging factor in the weak turbulence plane wave region has been approximated by Churnside as [11,24,33]:

$$A = \left[1 + 1.07\left(\frac{kD^2}{4L}\right)^{7/6}\right]^{-1} \tag{3.7}$$

Eq. (3.7) is plotted in Fig. 3.1 along with the exact theory formula, Eq. (3.4), for the plane wave. There is a 17% difference in the approximate value of A from the exact theory when $\sqrt{kD^2/4L} = 1$ [11]. Other approximations have been made to the theoretical aperture averaging factor, and show slightly better results. Andrews reported the approximate form for the aperture averaging factor as [34]:

$$A = \left[1 + 1.062\left(\frac{kD^2}{4L}\right)\right]^{-7/6} \tag{3.8}$$

At the same location, where $\sqrt{kD^2/4L} = 1$, the Andrews approximation is 7% higher than the exact theory assuming a Kolmogorov spectrum.

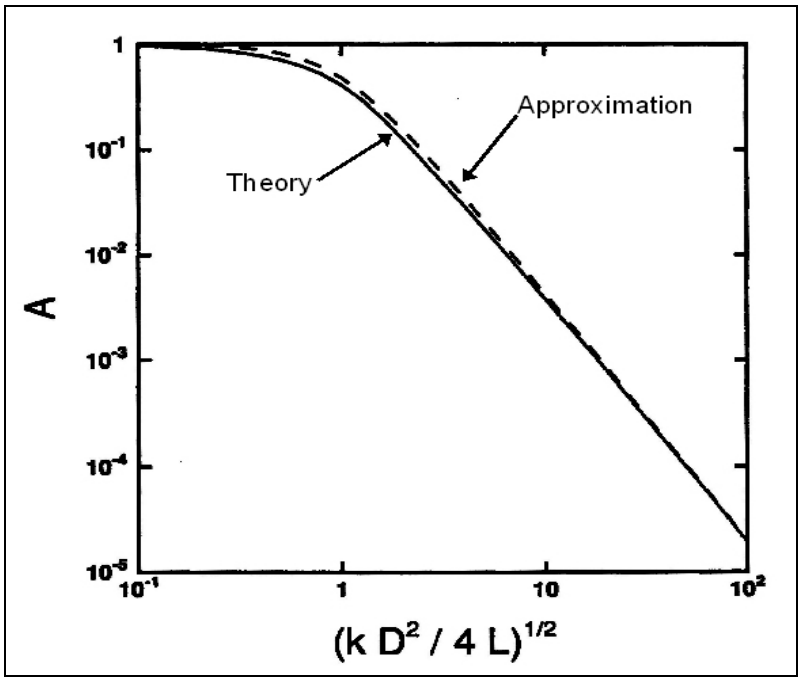

Fig. 3.1: Aperture averaging factor for a plane wave plotted against the ratio of the aperture radius to the Fresnel zone size. The solid line is the exact theory from Eq. (3.4) while the dashed line is Churnside's approximation in Eq. (3.7) [11].

3.2.2.2 Plane Wave, Large ℓ_o

Either the Tatarskii spectrum from Eq. (2.23) or the Hill spectrum [19] may be used when the inner scale is large $\ell_o >> (L/k)^{1/2}$. The Tatarskii spectrum is analytically simpler than the Hill spectrum, and the results are similar [24]. By substituting Eq. (2.23) into the covariance Eq. (3.2), and letting $r \to 0$, the covariance becomes [11]:

$$C_I(0) = 12.8 C_n^2 L^3 \ell_o^{-7/3} \tag{3.9}$$

By following a similar method as in Section 3.2.2.1, and making the substitution $u = kD/2$, the aperture averaging factor is [11]:

$$A = 0.686\left(\frac{D}{\ell_o}\right)^{-7/3} \int_0^\infty u^{-2/3} J_1^2(u) \exp\left(-0.1141 \frac{\ell_o^2 u^2}{D^2}\right) du \tag{3.10}$$

When $D >> 1$, the exponential in Eq. (3.10) approaches unity, and A can be approximated by [11]:

$$A = \left[1 + 2.21\left(\frac{D}{\ell_o}\right)^{7/3}\right]^{-1} \tag{3.11}$$

An improved approximation to Eq. (3.11) is [11]:

$$A = \left[1 + 2.19\left(\frac{D}{\ell_o}\right)^{2}\right]^{-7/6} \quad \text{for } 0 \le D/\ell_o \le 0.5 \tag{3.12}$$

3.2.2.3 Plane Wave, ℓ_o on the Order of the Fresnel Length

In an intermediate regime, when the inner scale is similar to the Fresnel length, a decision must be made as to which approximation to the aperture averaging factor to use. By setting the two aperture averaging approximations equal to each other, Eq. (3.8) = Eq. (3.12), they are found to be equal when $\ell_o = 2.73(L/k)^{1/2}$. Churnside has recommended using the small inner scale approximation when $\ell_o < 2.73(L/k)^{1/2}$, and the large inner scale approximation when $\ell_o > 2.73(L/k)^{1/2}$ [11]. Andrews recommends using Eq. (3.8) when $kD^2/4L < 1$ [34].

3.2.2.4 Spherical Wave, Small ℓ_o

The Kolmogorov spectrum may be used to evaluate the covariance of the irradiance (Eq. (3.2)), along with $s = z/L$ for a spherical wave, and $r = 0$ [11]:

$$C_I(0) = 0.497 C_n^2 k^{7/6} L^{11/6} = \sigma_I^2 \equiv \sigma_{R,sp}^2 \tag{3.13}$$

The exact form of the aperture averaging factor in Eq. (3.1) is written using the spherical wave covariances [11]:

$$A = 53.4k^{5/6}L^{-11/6}\int_0^{\infty} dKK^{-8/3}\int_0^1 dz\sin^2\left[\frac{K^2 z(L-z)}{2kL}\right] \times \int_0^1 dyyJ_0\left(\frac{KDzy}{L}\right)\left[\cos^{-1} y - y\left(1-y^2\right)^{1/2}\right] \tag{3.14}$$

After evaluating the aperture averaging factor integral as in Section 3.2.2.1, it can be approximated as [11]:

$$A = \left[1 + 0.214\left(\frac{kD^2}{4L}\right)^{7/6}\right]^{-1} \tag{3.15}$$

The exact and approximate forms of the aperture averaging factor for a spherical wave with small inner scale are shown in Fig. 3.2. Where $\sqrt{kD^2/4L} = 1$, the approximate version predicts the amount of aperture averaging to be 86% less than the theory [11,24].

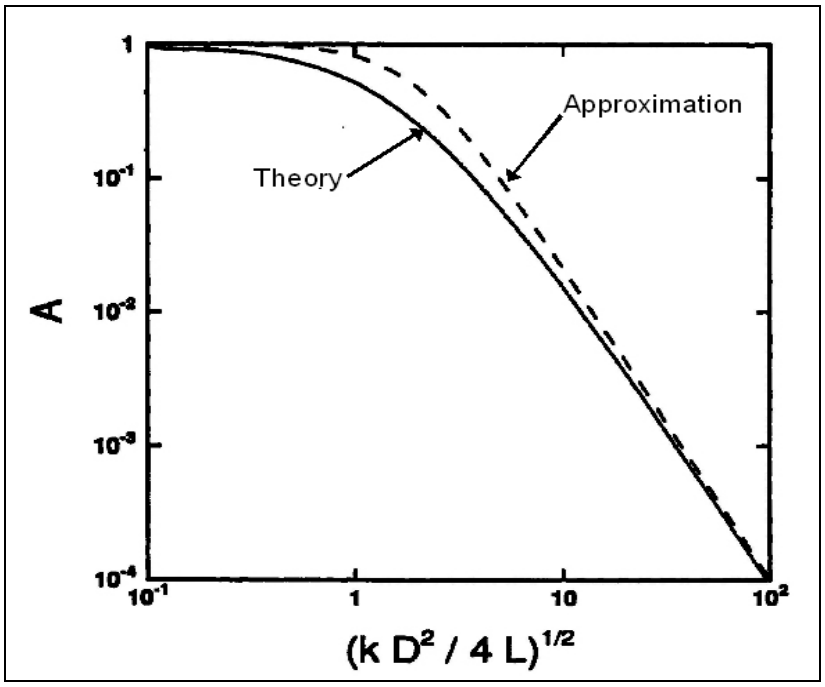

Fig. 3.2: Aperture averaging factor for a spherical wave with small inner scale. The solid line is the exact theory given a Kolmogorov spectrum, while the dashed line is the approximate formula of Eq. (3.15) [11].

3.2.2.5 Spherical Wave, Large ℓ_o

By evaluating the covariance of the irradiance in Eq. (3.2) with the Tatarskii spectrum, and $r = 0$ [11]:

$$C_I(0) = 1.28 C_n^2 L^3 \ell_o^{-7/3} = \sigma_I^2 \tag{3.16}$$

The aperture averaging factor is approximated by [11]:

$$A = \left[1 + 0.109 \left(\frac{D}{\ell_o} \right)^{7/3} \right]^{-1} \tag{3.17}$$

3.2.2.6 Spherical Wave, ℓ_o on the Order of the Fresnel Length

By following the argument in Section 3.2.2.3, Eq. (3.15) is equal to Eq. (3.17) when ℓ_o is 1.5 times the Fresnel length. Churnside recommends using the small inner scale approximation when $\ell_o < 1.5(L/k)^{1/2}$ and the large inner scale approximation when $\ell_o > 1.5(L/k)^{1/2}$ [11]. Andrews recommends using the small inner scale result when $kD^2/4L < 1$.

3.3 Aperture Averaging Experiment

Experimental aperture averaging data is necessary to verify previously developed theory [1,13,16,17,20] and ensure that modern optical communication systems are correctly optimized. After the development of plane wave theory of optical propagation through turbulence, the advent of the laser allowed experimental studies of aperture averaging. However, these experiments were conducted over very long paths and were susceptible to the effects of saturation of scintillation [17]. A more recent experiment by Churnside [11,24] used 100, 250, 500, and 1000 m paths to avoid

saturation effects, and produced results in reasonably good agreement with spherical-wave theory over short paths of 250 m [11,24]. Over longer paths, the experimental data tended to diverge from theory. The scintillometer used in the experiment measured turbulence over a 250 m path, and not the path length under test, which reduces confidence in the precision of the C_n^2 data. Other shortcomings of this experiment include the lack of simultaneous background light measurements and a use of only six apertures, ranging from 1 mm to 5 cm. Many commercial free space optical communication units use apertures with diameters larger than 5 cm, so breadth of data collected by Churnside in Ref. [11] is insufficient for practical use.

3.3.1 Aperture Averaging Transmitter and Receiver Systems

The aperture averaging transmitter uses a 21 mW JDS Uniphase HeNe laser. The laser operates in a single mode (TEM_{00}) at 632.8 nm, with a 0.70 mm output diameter and 1.15-mrad beam divergence. The beam passes through an optical chopper and a 30x Melles Griot beam expander. The beam expander is adjustable so that the beam diameter at the receiver may be tuned; for this experiment, the beam diameter at the receiver is ~1.5 m. The optical chopper serves an important purpose during the data acquisition in that it allows us to calculate mean background light levels at the same time that intensity data is being recorded. The optical chopper is operated with a frequency of 3.636 ms, which is on the order of the time that the turbulence on a specific path through the atmosphere remains constant. A photograph of the aperture averaging transmitter is shown in Fig. 3.3.

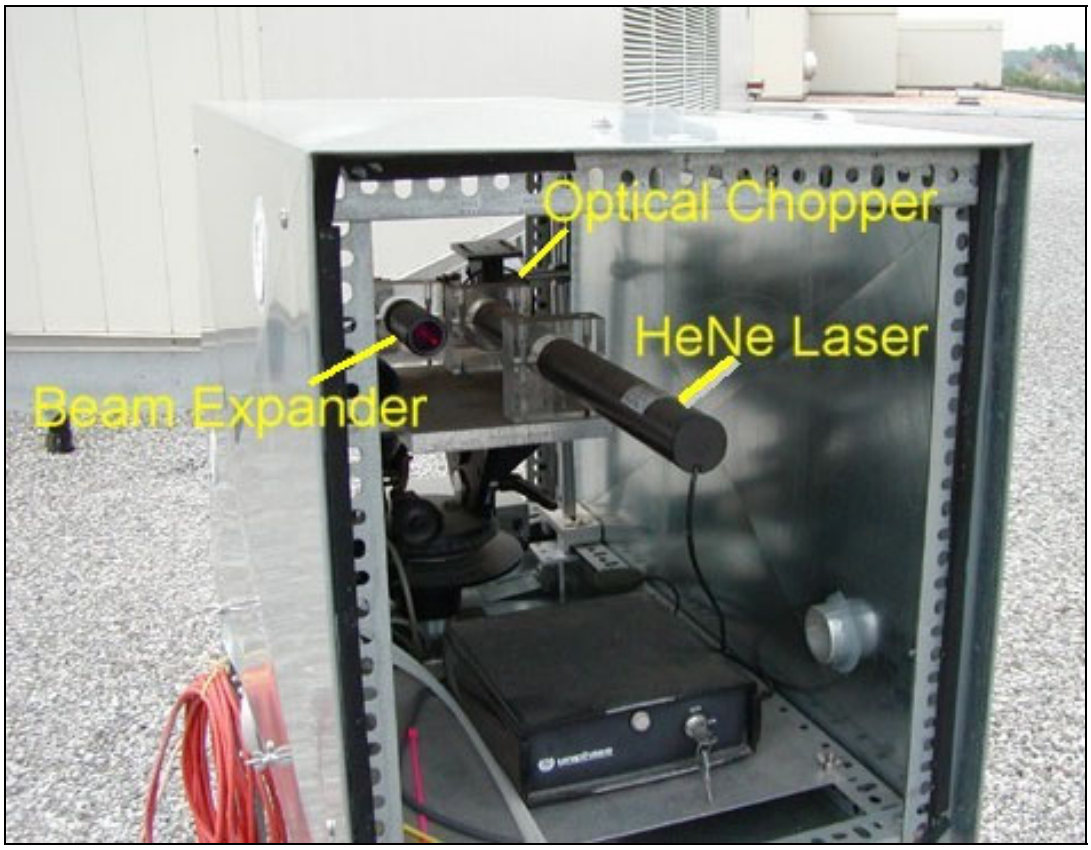

Fig. 3.3: Aperture averaging transmitter on the roof of the A.V. Williams Building at the University of Maryland, College Park.

The laser light propagates over an 863 m path between the A.V. Williams Building and the Chesapeake Building. The transmitter on the roof of A.V. Williams is approximately 14 meters above the ground, while the receiver in the Chesapeake Building is approximately 12 meters above ground. An aerial photograph of the path, with the line of sight indicated, is shown in Fig. 3.4. The terrain propagated over is mostly asphalt parking lots, with a few trees and grassy fields. One part of the path passes near the rotunda on the east side of the Comcast Center, which may have some affect on the homogeneity of the turbulence measurements.

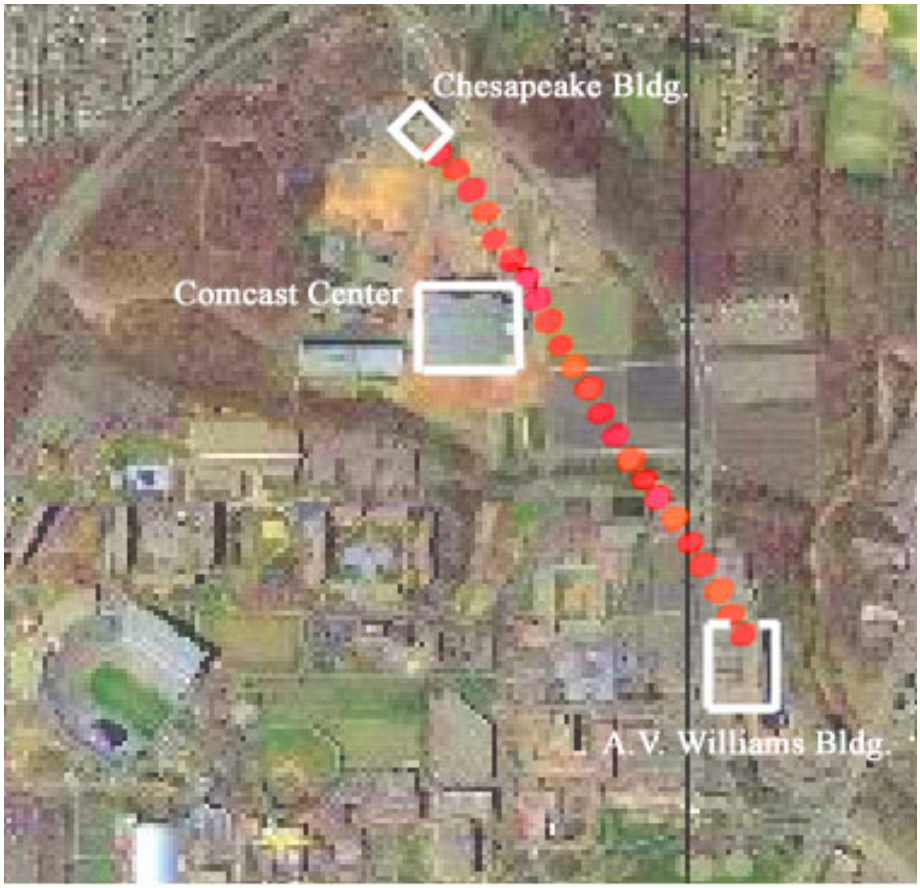

Figure 3.4: An aerial photograph of the propagation path (dotted line). Satellite photograph taken in 2002 by GlobeXplorer.

The receiver system is composed of two receive apertures, a point receiver and a variable aperture receiver, shown in Fig. 3.5. The point receiver is an effective scintillometer and is used to calculate path-averaged C_n^2 measurements. Light is first filtered through a laser line filter at 632.8 nm with a 10 nm passband width. The filter removes any stray light from interfering with the operation of the scintillometer. The laser line filter is angle dependent, so only light parallel to the propagation path at a wavelength near 632.8 nm will pass. The aperture diameter of the point receiver is 5 mm, which is smaller than the Fresnel zone size for the path, $\sqrt{\lambda L} = 2.34\,\text{cm}$. The minimum aperture size, required to measure $A = 1$ in weak turbulence, is the diameter

where $kD^2/4L = 1$. For this experimental setup, D_{min} = 1.86 cm. Since the scintillometer aperture diameter is smaller than the minimum aperture diameter for A = 1, the baseline C_n^2 measurements are true path-averaged values. After passing through the scintillometer receive aperture, light is detected by a Perkin-Elmer FFD-100 Si photodetector. The FFD-100 has a 5.1 mm^2 active area, with a responsivity of 0.43 A/W at 632.8 nm. The detected signal is amplified by a variable transimpedance amplifier and recorded by LabVIEW.

The variable aperture receiver is a Rolyn Optics 20 cm planoconvex lens. An aperture stop of sizes ranging from 1 cm to 16 cm is placed behind the plane side of the lens, to limit the aperture diameter. To ensure that the receiver does not saturate, a New Focus neutral density filter wheel is placed in front of the photodetector. At large receive apertures, the filter wheel is necessary to avoid detector saturation and measure the intensity variance accurately. Since neutral density filters are not angle dependent, they will not affect the distribution of irradiance fluctuations. The incident beam is then received by a Perkin Elmer FFD-200 Si photodetector and amplified through a variable transimpedance amplifier. The transimpedance gain is set when the photodetector is illuminated through the smallest aperture diameter; thereby allowing the electronic gain to remain constant, while the receive optical power is controlled by changing the neutral density filter transmittance. The FFD-200 has a 20 mm^2 active area with a responsivity of 0.43 A/W at 632.8 nm. The signal is than recorded and processed in LabVIEW. Typical oscilloscope traces of the aperture averaged and scintillometer signals are shown in Fig. 3.6.

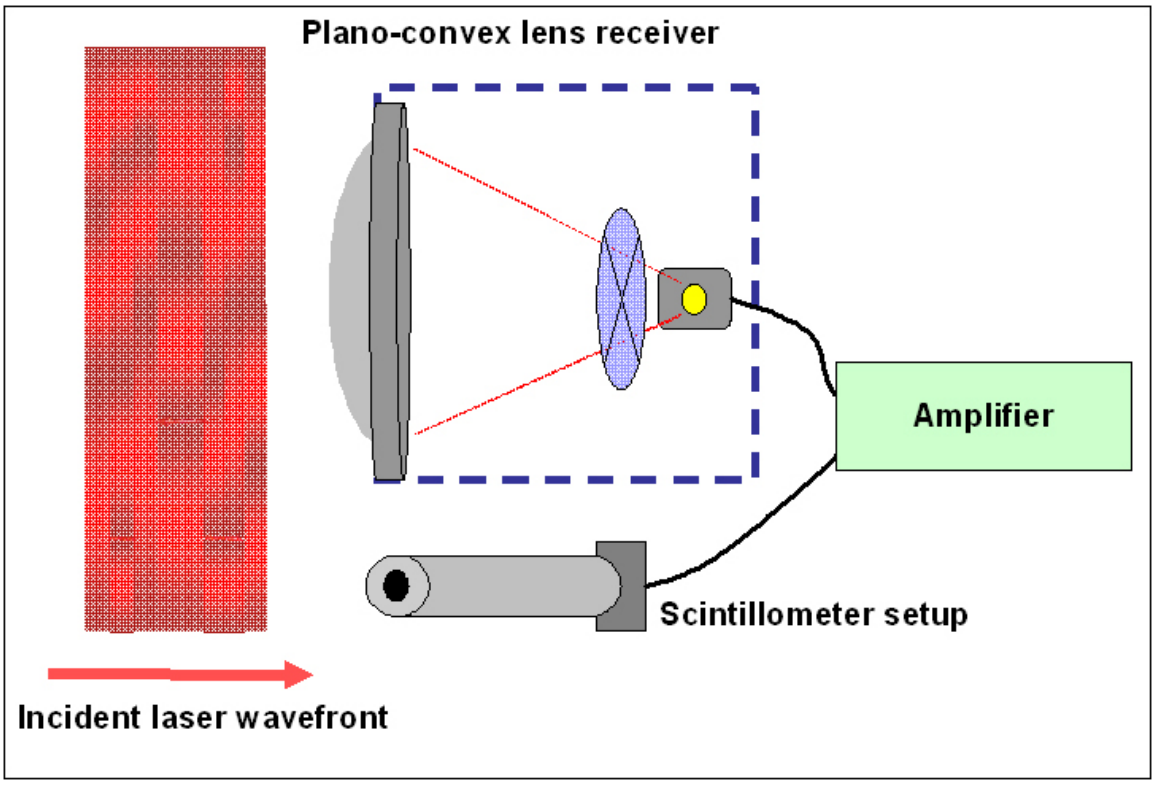

Fig. 3.5: Diagram of the aperture averaging receiver setup. The scintillometer channel uses a 5 mm diameter receive lens.

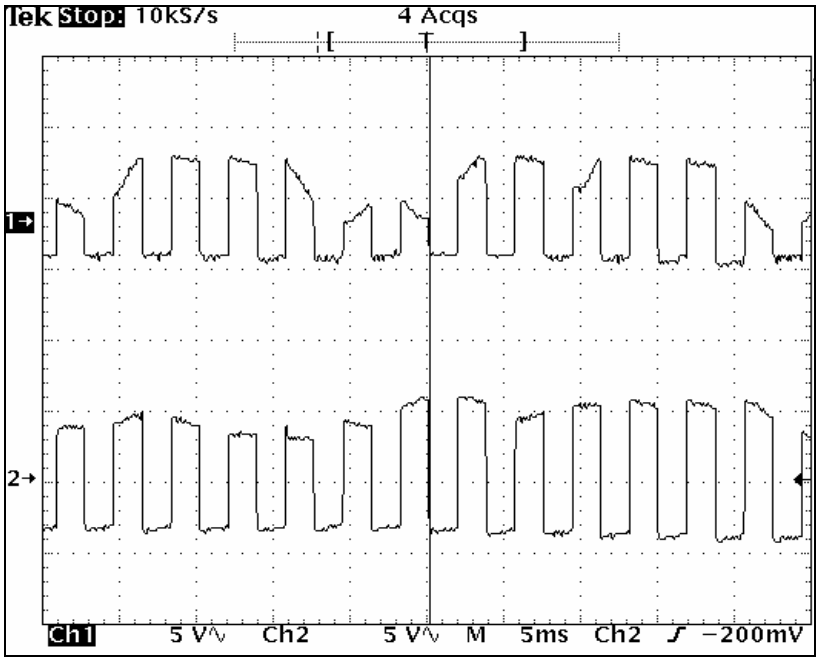

Fig. 3.6: An optically chopped signal propagated over 863 m and viewed on the Tektronix oscilloscope. Channel 1 is the signal detected by the scintillometer, while Channel 2 is detected by the aperture averaged receiver. The signal detected on Channel 2 shows smaller intensity fluctuations.

3.3.2 LabVIEW Data Acquisition

A customized LabVIEW program, whose front panel is shown in Fig. 3.7, samples the optically chopped 275 Hz signal at a rate of 3000 samples/sec. Data collection for each aperture is typically done in 5 to 15 minute intervals. The maximum and minimum interchannel sampling delays for two channels are 62.5 μsec and 5 μsec, respectively. This time difference is well below the reordering time of the turbulent atmosphere, so the turbulent channel is quasistationary.

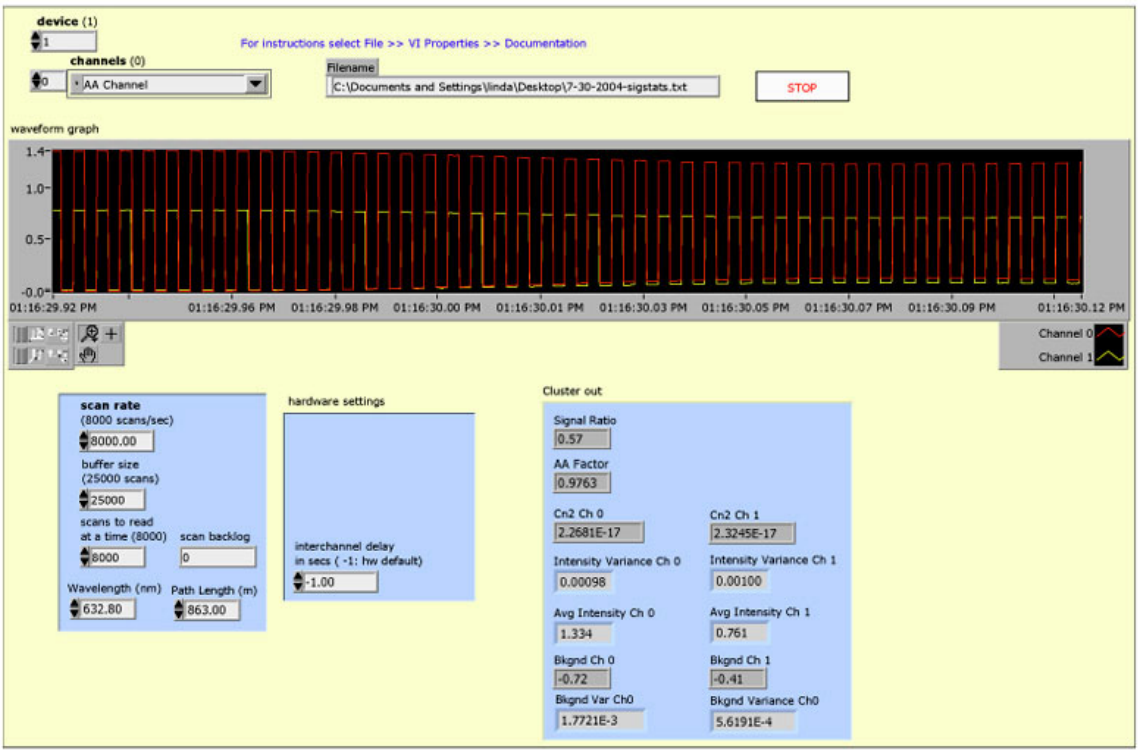

Fig. 3.7: Front panel of the LabVIEW program designed to calculate and record irradiance statistics for the aperture averaging experiment.

The LabVIEW program calculates irradiance statistics relevant to determining the aperture averaging factor over a 1 minute sampling interval. Fig. 3.8 is a flowchart representing the data acquisition process for one channel. The chart explains the methodology used to determine the normalized irradiance variance, σ_I^2, from the

measured waveform data. The *waveform* type in LabVIEW is a new data type introduced in LabVIEW 6.0 that stores information on sampled voltage (y), acquisition start time (t_0), and sampling interval (Δt). The *waveform* type makes signal analysis easier because the sampled data is synchronized with the sampling time. LabVIEW also includes an extensive functionality to take advantage of the *waveform* type.

From Fig. 3.8, the detected chopped signal is sorted into high and low voltage values. The mean of the low values is the average background signal. This background signal is than subtracted from the recorded high values, which is then averaged over a 1 minute interval to give the mean intensity. Simultaneously, the variance of the high values for that acquisition period is calculated. The variance of the high values is then normalized by the square of the mean intensity, which gives σ_I^2.

Table 3.1 shows the 13 values that are output by LabVIEW into a data file. The two channels recorded are called Ch. 0 and Ch. 1, due to the naming conventions in LabVIEW. The one 1-min path averaged C_n^2 is then calculated from the normalized irradiance variance σ_I^2 using the equation for the plane wave Rytov variance. The aperture averaging factor, A, is calculated each sampling interval from the ratio of the normalized intensity variances of the two channels, as in Eq. (3.1). These values are then written to a data file every minute. The background variance values are only output to ensure that there is no significant baseline wander on the measured signal that could distort the measured irradiance statistics.

The LabVIEW program requires a large storage buffer to hold 60 seconds worth of samples, measured at 3000 samples per second. Shorter averaging times were also used in the initial experiments, however results were much more erratic. The longer

averaging time ensures that there are a sufficient number of samples so that lognormal statistics are obeyed [35]. Only half the number of samples acquired may be used in the calculation of the irradiance variance, since the signal is optically chopped. The other half of the samples are used to determine the mean background level.

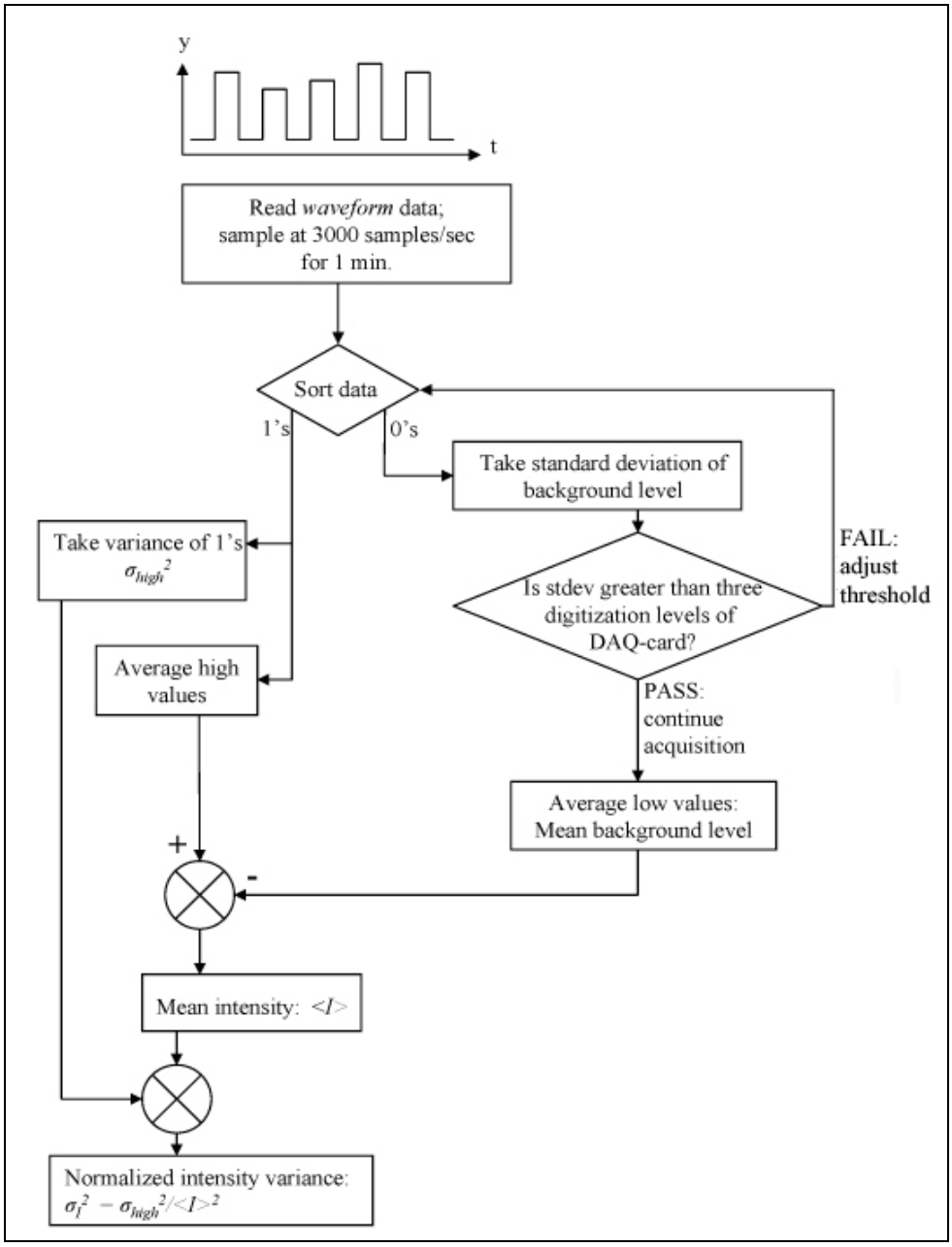

Fig. 3.8: Flowchart of the data acquisition process in LabVIEW for one channel. The diagram explains how intensity and background levels are determined for the sampled signal averaged over a 1 min. interval.

Time	measured to 1/1000th of a second
Signal Ratio	$\frac{\langle I \rangle_{Ch.1}}{\langle I \rangle_{Ch.0}}$
Aperture Averaging Factor, A	$\frac{\sigma^2_{I\,Ch.0}}{\sigma^2_{I\,Ch.1}}$
C_n^2 Ch. 0	$\frac{\sigma^2_{I\,Ch.0}}{1.23k^{7/6}L^{11/6}}$
Irradiance Variance Ch. 0	$\sigma^2_{I\,Ch.0}$, variance of high values normalized by $\langle I \rangle^2_{Ch.0}$
Average Intensity Ch. 0	$\langle I \rangle_{Ch.0}$, mean of high values with background level subtracted out
Average Background Ch. 0	mean of low values
Background Variance Ch. 0	variance of low values
C_n^2 Ch. 1	$\frac{\sigma^2_{I\,Ch.1}}{1.23k^{7/6}L^{11/6}}$
Irradiance Variance Ch. 1	$\sigma^2_{I\,Ch.1}$, variance of high values normalized by $\langle I \rangle^2_{Ch.1}$
Average Intensity Ch. 1	$\langle I \rangle_{Ch.1}$, mean of high values with background level subtracted out
Average Background Ch. 1	mean of low values
Background Variance Ch. 1	variance of low values

Table 3.1: List of 13 values output per averaging interval in LabVIEW data file. Here, Channel 0 represents the aperture averaged signal, while Channel 1 represents the scintillometer signal.

3.3.3 Fetch Effects

The height of the path above ground, approximately 12 m, limits the strength of turbulence experienced on an average day. Although the terrain along the path is mostly flat with grass of pavement, there are a few trees and two buildings that impinge

on the path, which could result in fetch effects. To be able to neglect fetch effects, the height above ground must be larger than the boundary layer 100-to-1 rule for fetch effects [36,37]. The rule states that there will be an internal boundary layer established at a height that is $1/100^{th}$ of the half width of the path. For our path of 863 m, this height is approximately 4.3 m. Since that propagation path is higher than this internal boundary layer, we can assume that we are nearly free of fetch effects [36,37].

3.4 Plane Wave Experimental Results

Theory and approximation of the plane wave aperture averaging factor with small inner scale was presented in Sec. 3.2.2.1. The aperture averaging factor, A, is typically plotted against the ratio of the aperture radius to the Fresnel zone size. Recall that the Fresnel zone size is the dominant scale size in cases of weak turbulence. Three accepted approximations to the aperture averaging factor are calculated and plotted in Fig. 3.9. The scintillation index model is an attempt to define an irradiance variance that is valid across all turbulence levels. The plane wave scintillation index diverges from its Rytov predicted weak turbulence value when $\sigma_R^2 \geq 0.5$. Therefore, for different strengths of turbulence indicated by C_n^2, the scintillation index model does predict different aperture averaging results from the accepted approximations to weak turbulence theory. A C_n^2 value of 10^{-16} $m^{-2/3}$ corresponds to $\sigma_R^2 = 0.0043$. A C_n^2 of 10^{-14} $m^{-2/3}$ changes the Rytov variance by a factor of 100 and we find that $\sigma_R^2 = 0.43$.

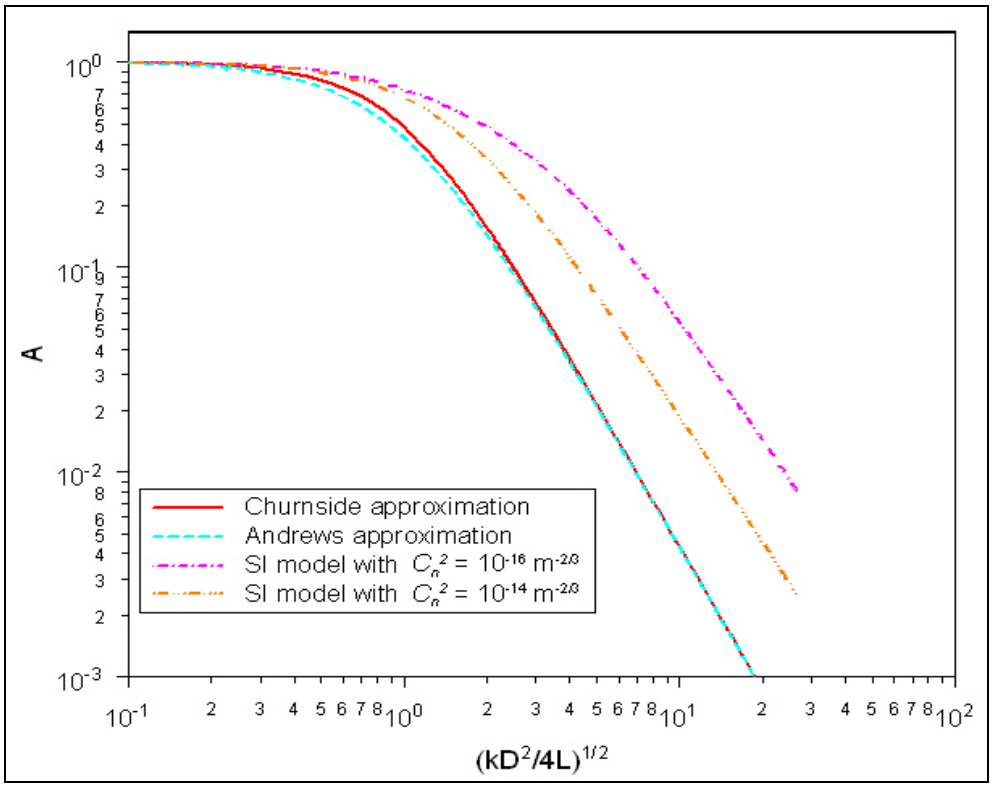

Fig. 3.9: Plane wave aperture averaging factor plotted as the Churnside approximation Eq. (3.7), the Andrews approximation Eq. (3.8), and the scintillation index (SI) model for various values of C_n^2.

Experimental data plotted against the ratio $\sqrt{kD^2/4L}$ is shown in Fig. 3.10. The mean data is plotted with error bars of one standard deviation. The data does follow the trend predicted by theory. For smaller apertures, the experimental aperture averaging data seems to retain high values, whereas the approximate models drop off. Since the laser is diverged, we expect better agreement with the spherical wave aperture averaging models.

The Andrews scintillation index model is the only model that takes into account the strength of turbulence in the weak fluctuation region. As seen from Fig. 3.10, the SI model predicts less aperture averaging than weak fluctuation theory for given values of receiver aperture. When our experimental data was analyzed, there was no significant

dependence of A on C_n^2 in the weak turbulence region, and certainly not the substantial variation predicted by the scintillation index model.

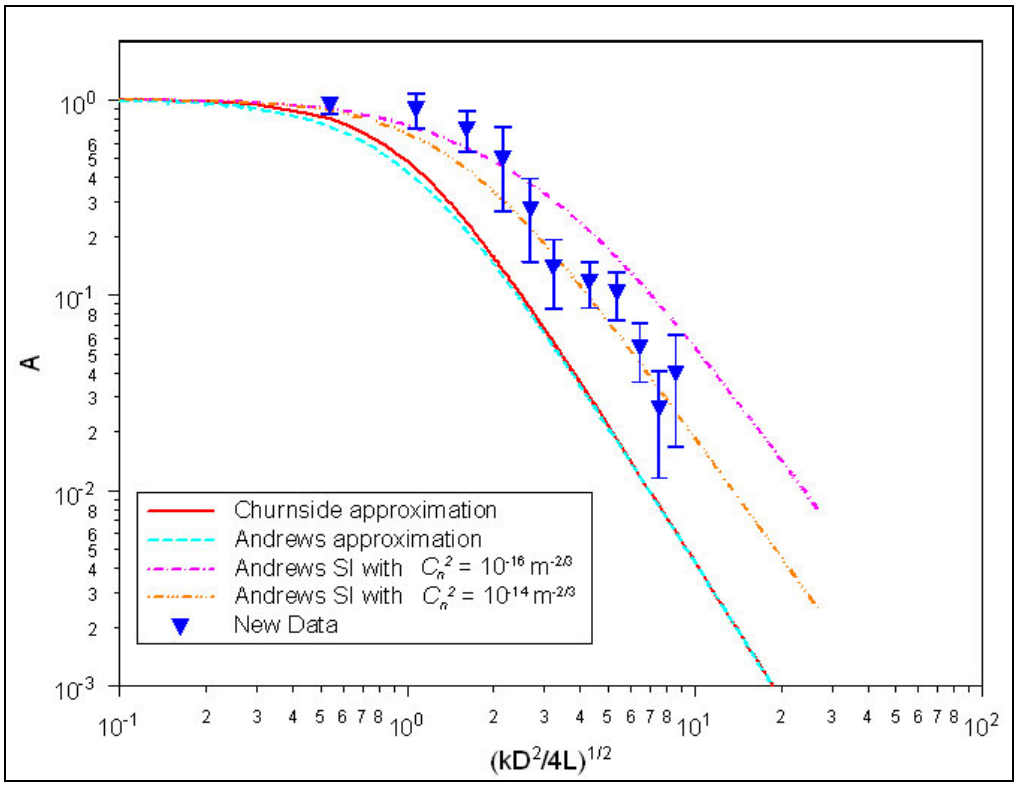

Fig. 3.10: New mean experimental data plotted with error bars, along with approximations to the aperture averaging factor.

The mean data is plotted along with the experimental Churnside data in Fig. 3.11. The Churnside data was measured on a 500 m path, although C_n^2 was measured over only half the path using an incoherent scintillometer [11,24]. It was assumed that due to the flatness of the terrain that the measured C_n^2 was indicative of the path averaged value. The laser and scintillometer were propagated over a plateau of grassland at a height of 1.5 m above ground. The 1.2 mrad divergence of the HeNe was used directly, so it was assumed that the data would be a better fit to the spherical wave theory. It is apparent from Fig. 3.11 that the plane wave theory does not sufficiently

characterize the amount of aperture averaging taking place, especially at larger aperture diameters.

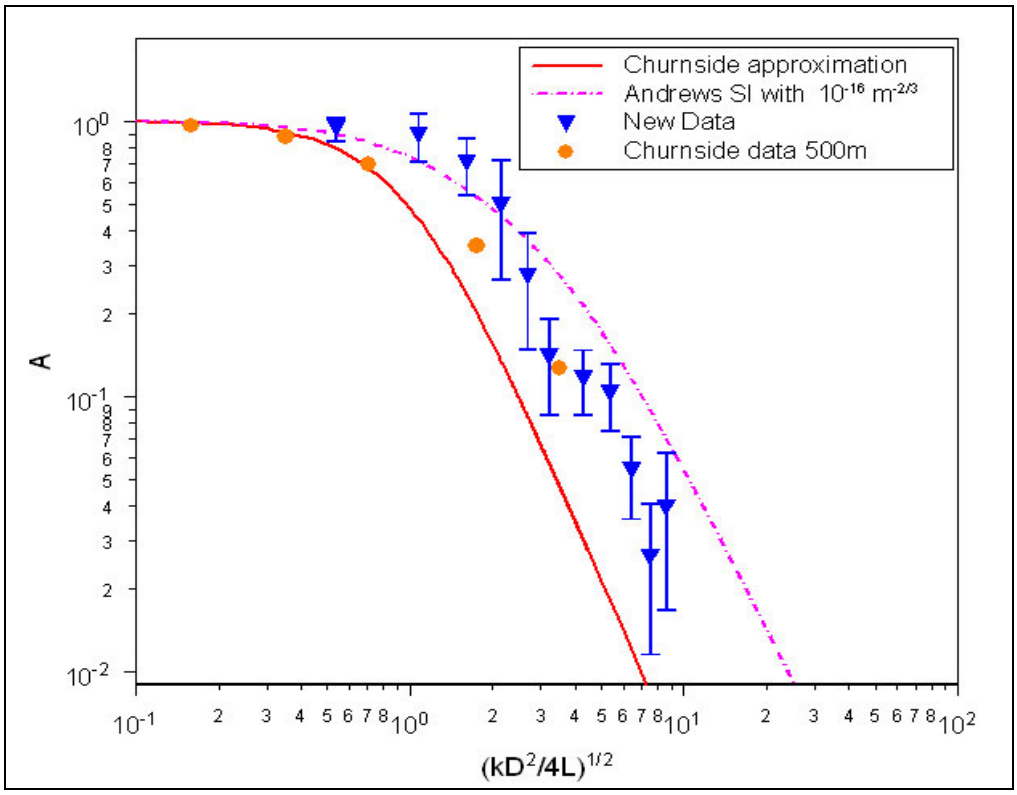

Fig. 3.11: New mean aperture averaging data plotted with Churnside experimental data taken over a 500 m path. Neither the plane wave Churnside approximation nor the SI model are a good fit to the data.

3.5 Spherical Wave Experimental Results

Spherical wave weak turbulence theory and approximation was presented in Section 3.2.2.4. Since the beam divergence in this experiment is ~ 1 mrad, we expect the data to be in good agreement with the spherical wave analysis. Fig. 3.12 compares the Churnside approximation to the scintillation index model for the aperture averaging factor. The Churnside model predicts a higher knee than the scintillation index model. As shown in Fig. 3.2, this knee overpredicts the exact theory given a Kolmogorov spectrum, thereby underestimating the amount of aperture averaging taking place.

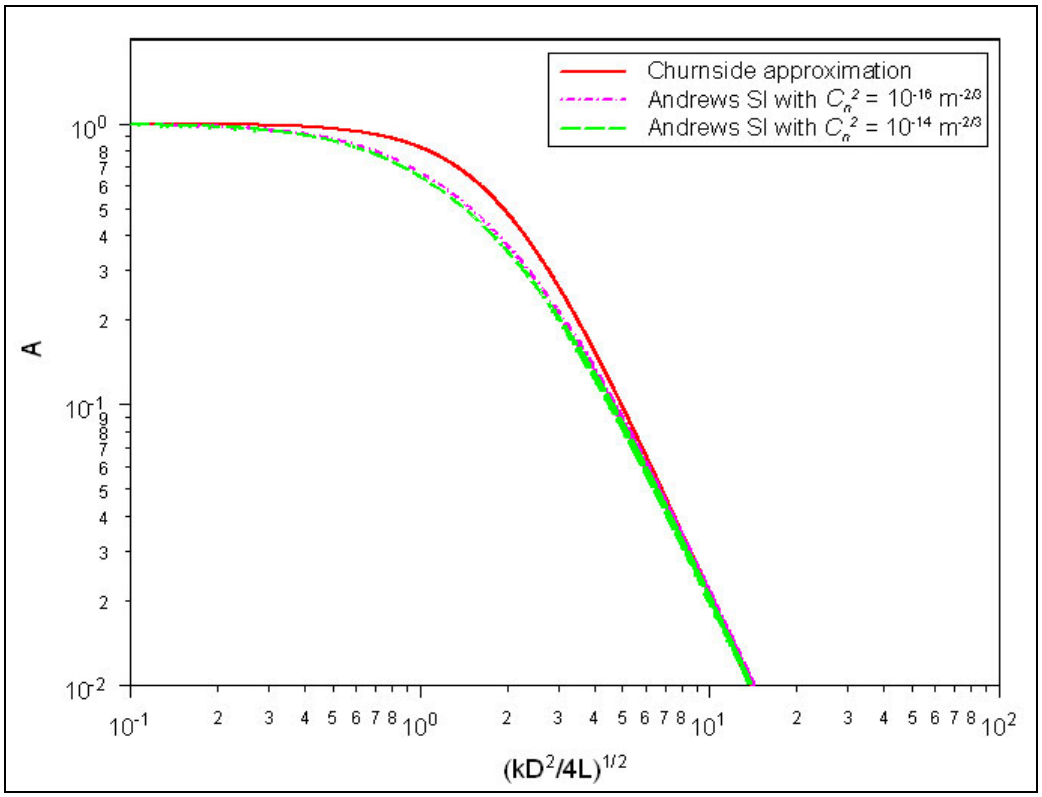

Fig. 3.12: Comparison of two different models for the spherical wave in weak turbulence. The Churnside approximation, Eq. (3.7), predicts a higher knee in the curve than the SI model.

Experimental mean aperture averaging data with error bars is shown in Fig. 3.13. In contrast to what is predicted by the exact theory, we see a higher knee in the data that the theory predicts near $\sqrt{kD^2/4L} \approx 1$. It also shows that the Churnside approximation is a better fit to the spherical wave data than the scintillation index model. This supports a generally accepted notion that aperture averaging in weak turbulence is independent of C_n^2.

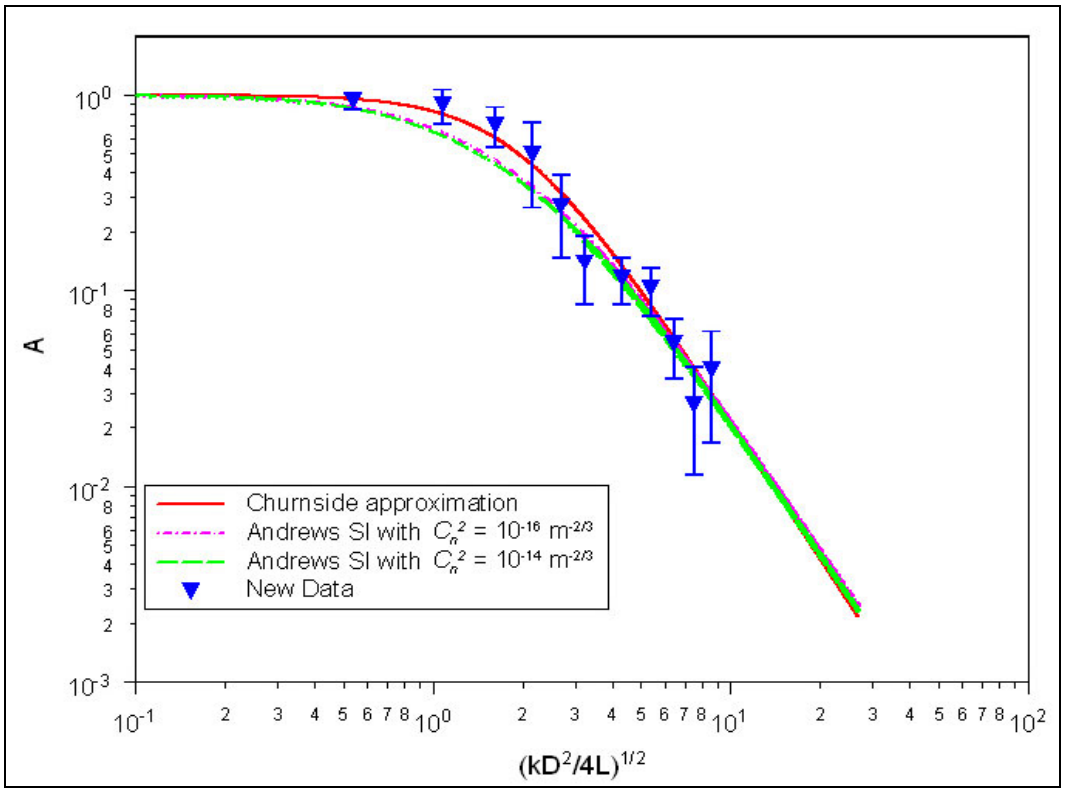

Fig. 3.13: Experimental mean aperture averaging data plotted against the ratio of aperture radius to the Fresnel zone size.

The Churnside experimental data measured over a 500 m path is displayed along with our mean data in Fig. 3.14. The Churnside data does not exhibit the same knee that our new data shows. Churnside assumed that a high knee is a result of a violation of propagation uniformity due to cloud cover over part of the path [11]. This seems to be an unlikely explanation for the knee in our new data, since the data was taken under clear weather conditions with wind speeds less than 4 m/s and low relative humidity. It is possible that a few trees and a building near the propagation path adversely affect the homogeneity of the atmosphere in that area. There may be additional scintillations induced near the transmitter since the laser propagates about 1.5 m above the roof of A.V. Williams over a length of 10 m.

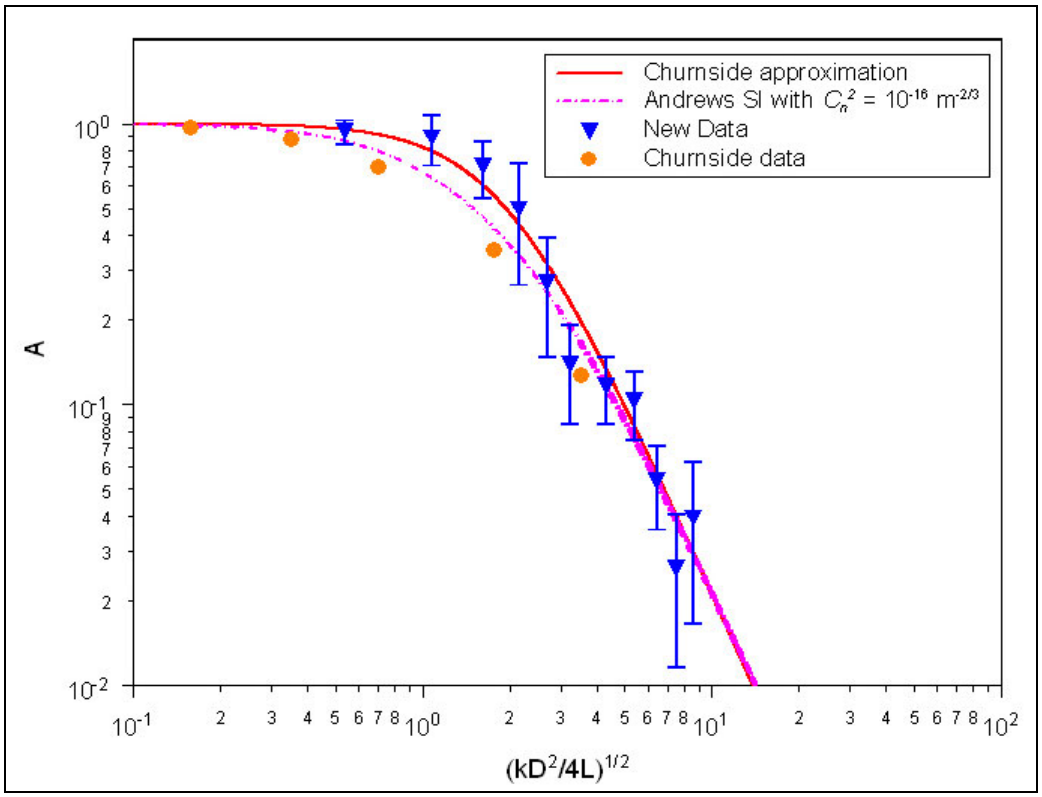

Fig. 3.14: Comparison of our new mean data with the Churnside data.

It is not apparent that the knee in the new data is due to inner scale effects. A large inner scale (larger than the Fresnel zone size), should reduce the aperture averaging factor, and not increase it as we are seeing. The Fresnel zone size is on the order of 1 cm, making it unlikely that the inner scale ℓ_o is larger than 1 cm for this path length and height. However, an inner scale that is smaller than the Fresnel zone size will still impact the data in weak turbulence conditions. Therefore, irradiance variance models including an ℓ_o dependence should be investigated.

3.6 New Aperture Averaging Model

Data was fit to the generalized form of the Churnside model in Eq. (3.15). A must be 1 when the aperture diameter becomes infinitesimal, so only the coefficient of

the $\sqrt{kD^2/4L}$ term was varied. The *genfit* function in MathCad allows arbitrary functions to be fitted to data matrices. Using this function, a fit to the measured aperture averaging data was found to be:

$$A = \left[1 + 0.196\left(\frac{kD^2}{4L}\right)^{7/6}\right]^{-1} \tag{3.18}$$

This new recommended fit, along with the new data and the Churnside approximation, given by Eq. (3.15), are plotted in Fig. 3.15.

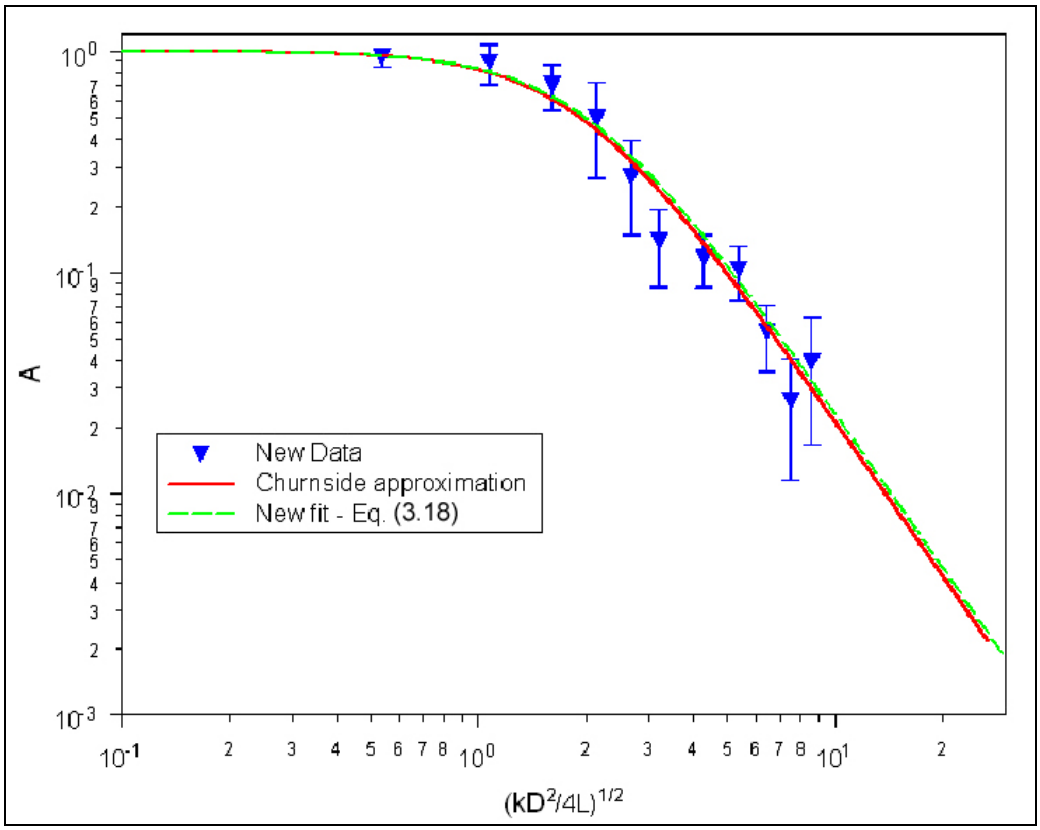

Fig. 3.15: New weak turbulence fit (Eq. 3.18) shown with new data and the Churnside model (Eq. 3.15).

The limitations of the $\sqrt{kD^2/4L}$ term do not pick up on the nuances of the data; more specifically, it does not predict the knee that we see in Fig. 3.14. Including a

square root term in the model does pick up on the knee, and we find the approximate formula using MathCad:

$$A = \left[1 + 0.266\left(\frac{kD^2}{4L}\right)^{7/6} - 0.162\left(\frac{kD^2}{4L}\right)^{7/12}\right]^{-1} \tag{3.19}$$

Fried had previously proposed that a fit could be improved with a $\left(\frac{kD^2}{4L}\right)^{7/12}$ term, although Churnside discounted the term as unnecessary [16].

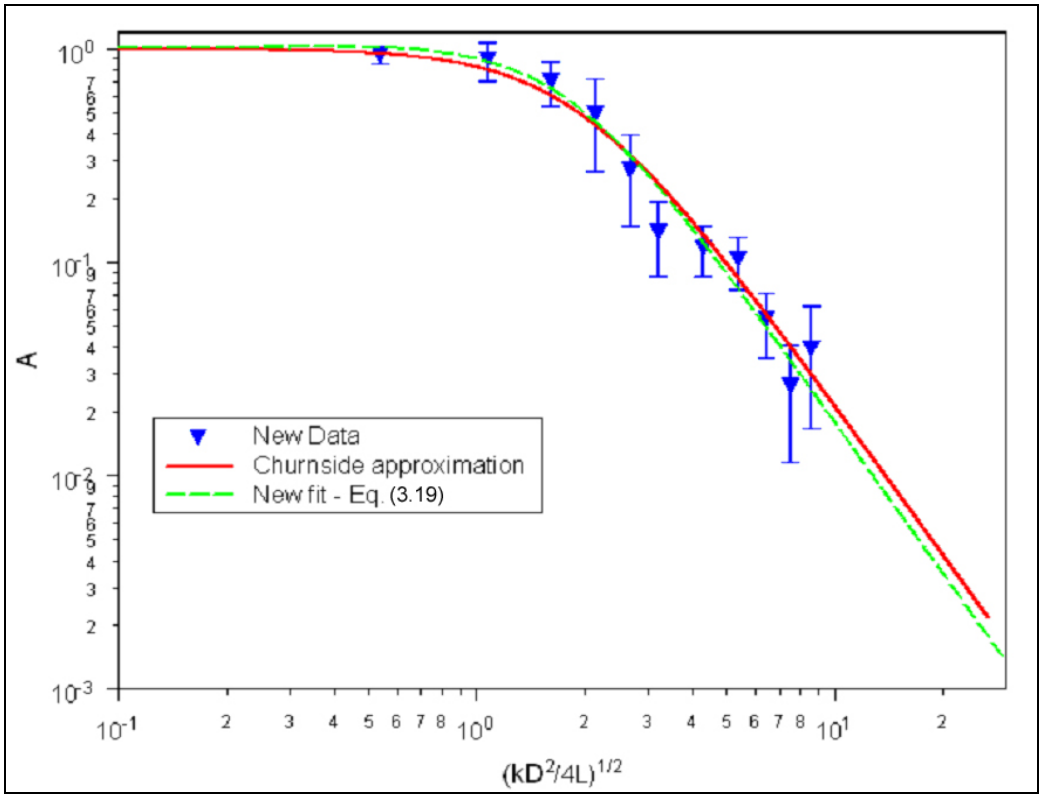

Fig. 3.16: New fit to weak turbulence data with an additional square root term, given by Eq. (3.19), plotted along with the Churnside approximation in Eq. (3.15).

3.7 Determination of the Inner Scale of Turbulence, ℓ_o

Although inner scale could not be measured during the aperture averaging experiments, ℓ_o may be determined by fitting available aperture averaging models to the

collected new data. Similar to the development of a new aperture averaging model in Section 3.6, the *genfit* function in MathCad is used to determine ℓ_o.

In a first attempt to extract a value of ℓ_o, the new data is fit to the plane wave aperture averaging factor given a large ℓ_o given by Eq. (3.11). The fit determined ℓ_o = 5.27 cm, a value that is approximately an order of magnitude larger than what would be expected in weak turbulence conditions. The new data is plotted along with Eq. (3.11) using ℓ_o = 5.27 cm in Fig. 3.17. In our previous analysis, spherical wave models are expected to be in better agreement with data acquired on the Chesapeake-AVW test range. Although the fit in Fig. 3.17 is reasonable, the assumption that the diverged beam approximates a plane wave is not.

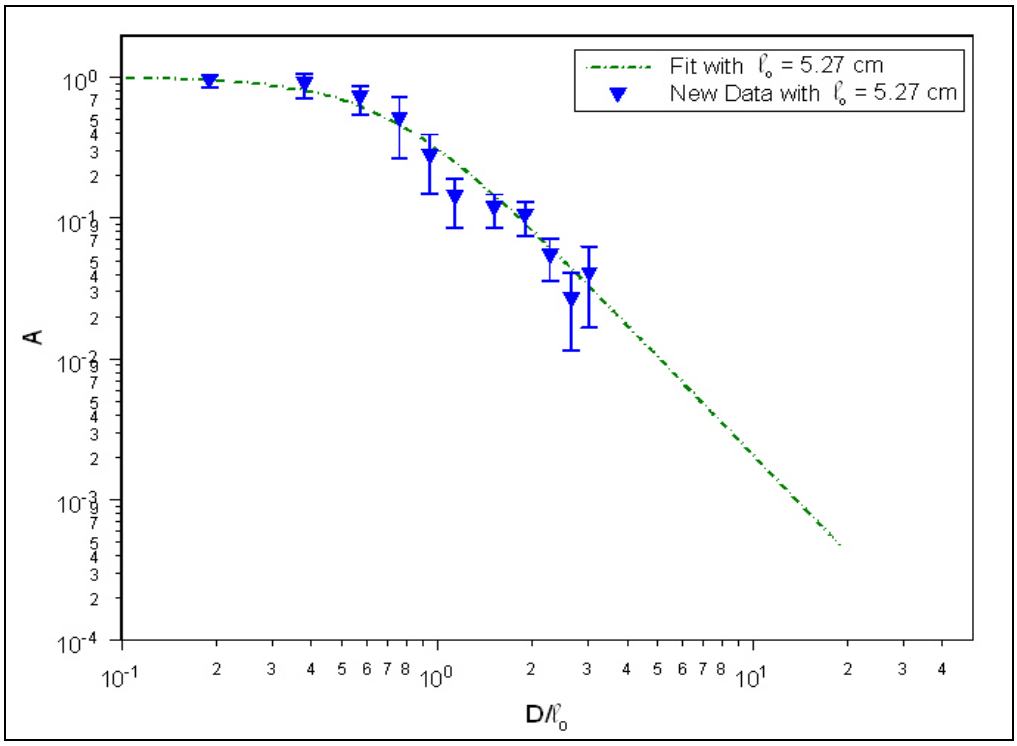

Fig. 3.17: Eq. (3.11) plotted using the curve fit value of ℓ_o = 5.27 cm, against the ratio of the aperture diameter to the inner scale. The dashed line represents Eq. (3.11).

The new data was next fitted to the aperture averaging factor for a spherical wave given a large inner scale, given by Eq. (3.17). The fit resulted in a predicted ℓ_o = 1.45 cm. This value is on the high end of the range of inner scale measurements reported in the literature [60,61]. The new data along with Eq. (3.17) with ℓ_o = 1.45 cm is shown in Fig. 3.18.

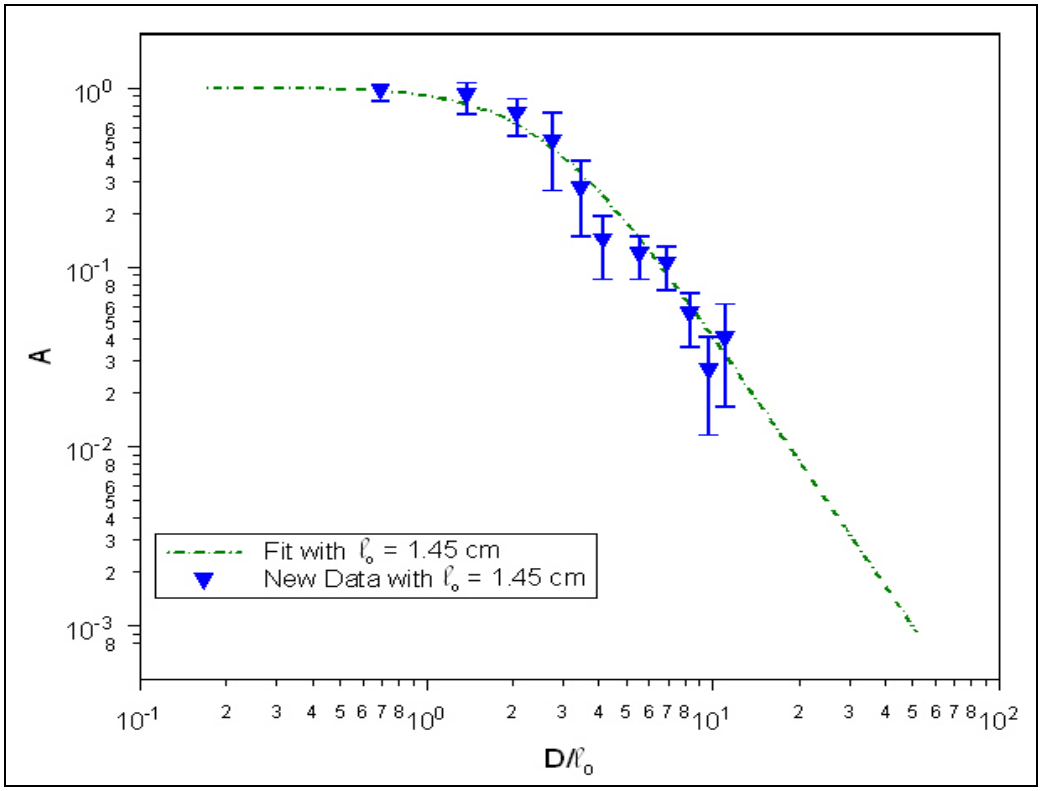

Fig. 3.18: Spherical wave aperture averaging factor for ℓ_o = 1.45 cm using Eq. (3.17) plotted along with the new data. The dashed line represents Eq. (3.17).

Since a reasonable value of ℓ_o has not been determined using the standard approximation to the aperture averaging factor, a more involved model for the dependence of the aperture averaging factor on ℓ_o is investigated. Recall that the modified atmospheric spectrum and effective atmospheric spectrum presented in Section 2.7.3 compose the best model to date for determining the influence of inner

scale on the irradiance variance. Using these spectra and assuming spherical wave propagation, the aperture averaging factor is calculated by taking the ratio of Eq. (2.73) with aperture diameter D to Eq. (2.73) with $D = 0$:

$$A = \frac{\sigma_I^2(D, \ell_o)}{\sigma_I^2(0, \ell_o)} \tag{3.20}$$

By using the *genfit* function in MathCad, the aperture averaging factor using the atmospheric spectrum predicts $\ell_o = 4.008$ mm. The new data along with the atmospheric spectrum aperture averaging factor for $\ell_o = 4.008$ mm are plotted in Fig. 3.19.

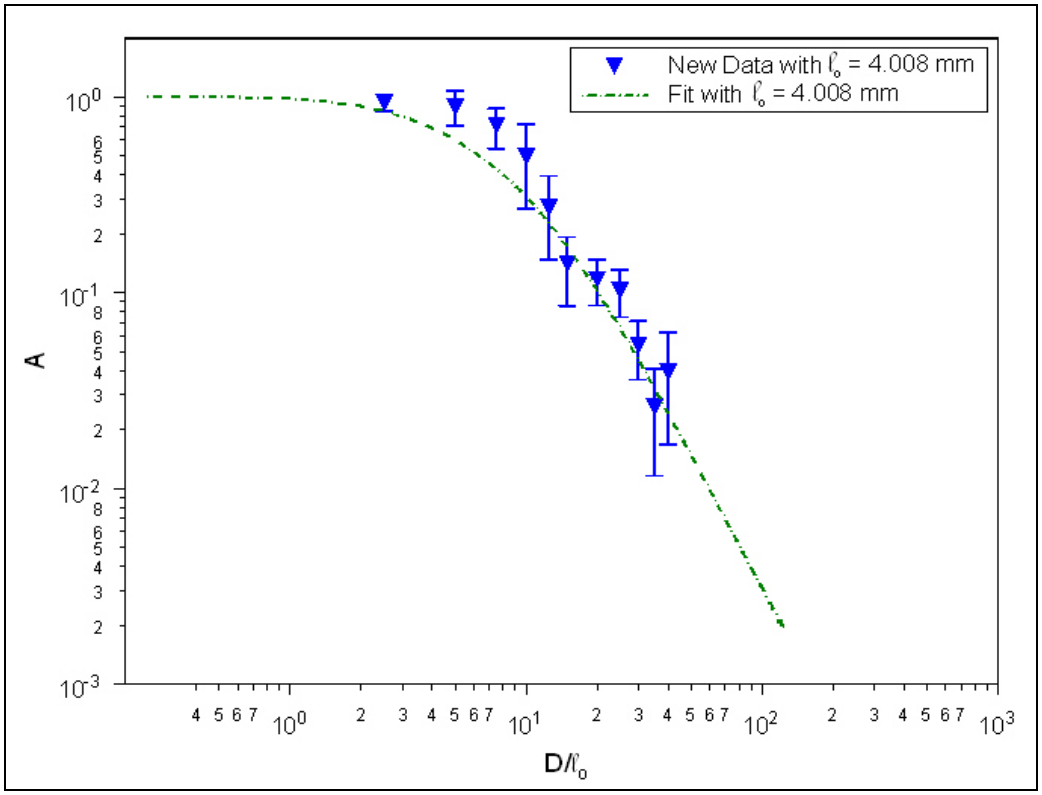

Fig. 3.19: New data is plotted using the predicted value $\ell_o = 4.008$ mm. The inner scale was determined using the atmospheric spectrum, which is represented by the dashed line.

The primary reason the Churnside plane wave and spherical wave approximations to the aperture averaging factor, given by Eq. (3.11) and (3.17), did not produce accurate inner scale values is that the models are meant to be used when the inner scale is larger than the Fresnel zone size. In our case, we expect the Fresnel zone size to be larger than ℓ_o. The atmospheric spectrum produces reasonable results because it is not constrained by the Fresnel zone size. The atmospheric spectrum mandates that the inner scale always impacts the irradiance variance in weak turbulence conditions. Although the model is much more complex than the Churnside approximations, its usefulness in determining the inner scale, especially when ℓ_o is not measurable, is proven.

Referring back to the discussion in Sec. 3.5, the atmospheric spectrum aperture averaging model with ℓ_o = 4.008 mm in Fig. 3.19 does not follow the knee of the data, as the Churnside spherical wave approximation in Fig. 3.18 does. It is still unclear what physical mechanism contributes to the knee. From Fig. 3.19, we can ascertain that even small values of ℓ_o will reduce A. It seems likely that the terrain uniformity and slightly off-horizontal path could act as forces counteracting the impact of ℓ_o. Either way, it is clear that improvements must be made to the atmospheric spectrum models of the irradiance variance in order to capture the physical nature of the relationship between the aperture averaging factor and ℓ_o.

3.8 Conclusions

The experimental results presented in this chapter show the behavior of the aperture averaging factor in weak turbulence. The data is consistent with models developed from the Kolmogorov, Tatarskii, and atmospheric spectra for spherical wave

propagation. This experiment was carefully planned out, and the results are the most accurate to date. The aperture averaging measurements presented here consider a variety of receive aperture diameters, simultaneous measurement of background light levels, and concurrent measurement of path-averaged C_n^2 values. Inner scale was also estimated from the data.

Chapter 4

Aperture Averaging in Strong Turbulence

4.1 Introduction

Aperture averaging in strong turbulence is extremely difficult to study because of the lack of a comprehensive theory for strong intensity scintillations including saturation effects [1,11,20,21,27,29,33,40,41]. In order to make useful comparisons of the experimentally determined aperture averaging factor with previously developed theory and numerical approximations, non-measurable quantities must be evaluated for this experiment. These include the Rytov variance, transverse coherence length, Fresnel zone, inner scale, and scattering disk size.

4.2 Data Analysis in Strong Turbulence

4.2.1 General Aperture Averaging Form

The general form of the aperture averaging factor for the spherical wave has the same representation as in weak turbulence theory, given by Eq. (3.1). The spatial covariance terms are represented by their strong turbulence theory counterparts.

4.2.2 Plane Wave Analysis

4.2.2.1 Churnside Asymptotic Analysis for the Plane Wave

The aperture averaging factor in strong turbulence may be evaluated using asymptotic theory [11,27]. The theory relies on the assumption that the irradiance

variance is the sum of 1 and a perturbation term, as discussed in Section 2.6.1. Asymptotic theory is the best theory to describe behavior in the saturation regime, because it uses a two-scale model to describe behavior in the inertial subrange and the transition into the dissipation region.

The asymptotic method uses three terms from the series expansion of the covariance function [27]. The asymptotic form of the covariance function for a plane wave with small inner scale is [11]:

$$C_I(\rho) = \exp\left[-\left(\frac{\rho}{\rho_0}\right)^{5/3}\right] + \tfrac{1}{2} N_3 \left(\frac{k\rho_0^2}{L}\right)^{1/3} \left[b_1(\rho) + b_2(\rho)\right] \tag{4.1}$$

where N_3 is a constant equal to 1.22 for a plane wave, and b_1 and b_2 are functions that go to unity as ρ goes to zero and go to zero when ρ goes to infinity. Specific descriptions of the formulas and the constant are found in Sec 2.6.1 and Ref. 27. Asymptotic theory includes the impact of two scale sizes, the scattering disk, $L/k\rho_0$, and the transverse coherence length, ρ_0. Asymptotic theory is expected to be valid only where the irradiance variance is close to unity, indicating a region of strong, saturated path-integrated turbulence [11].

For zero inner scale, the variance of the irradiance is related to the transverse coherence length by:

$$\sigma_I^2 = C_I(\rho = 0) = 1 + 1.22\left(\frac{k\rho_0^2}{L}\right)^{1/3} \tag{4.2}$$

By solving for ρ_0 in Eq. (4.2), we can find the predicted asymptotic value of ρ_0 by using measured values of σ_I^2. We can also use the transverse coherence length, ρ_0, for plane wave propagation, given in Eq. (4.3), to find predicted values of C_n^2 and, consequently, σ_R^2 using:

$$\rho_0 = \left(1.46k^2 LC_n^2\right)^{-3/5} \tag{4.3}$$

and

$$C_n^2 = \frac{\sigma_R^2}{1.23k^{7/6}L^{11/6}} \tag{4.4}$$

Churnside evaluated the aperture averaging factor as a sum of two terms, based on the two scale functions b_1 and b_2 in Eq. (4.1):

$$\begin{aligned} A_1 &= \frac{16}{\pi}\frac{\sigma_I^2+1}{2\sigma_I^2}\int_0^1 dyy\left[\cos^{-1}y - y\left(1-y^2\right)^{1/2}\right]\exp\left[-\left(\frac{Dy}{\rho_0}\right)^{5/3}\right] \\ A_2 &= \frac{56L^2}{3k^2D^2\rho_0^2}\frac{\sigma_I^2-1}{2\sigma_I^2}\int_0^1 dxx^{-2/3}J_1^2\left(\frac{kD\rho_0 x}{2L}\right) \end{aligned} \tag{4.5}$$

By evaluating the two components of the aperture averaging factor for large and small diameters, the approximate aperture averaging factor is given as [11]:

$$A = \frac{\sigma_I^2+1}{2\sigma_I^2}\left[1+0.908\left(\tfrac{D}{2\rho_0}\right)\right]^{-1} + \frac{\sigma_I^2-1}{2\sigma_I^2}\left[1+0.162\left(\tfrac{k\rho_0 D}{2L}\right)^{7/3}\right]^{-1} \tag{4.6}$$

The approximate aperture averaging factor, given in Eq. (4.6), for a plane wave with a small inner scale is plotted in Fig. 4.1, using AVW-Chesapeake test range characteristic values.

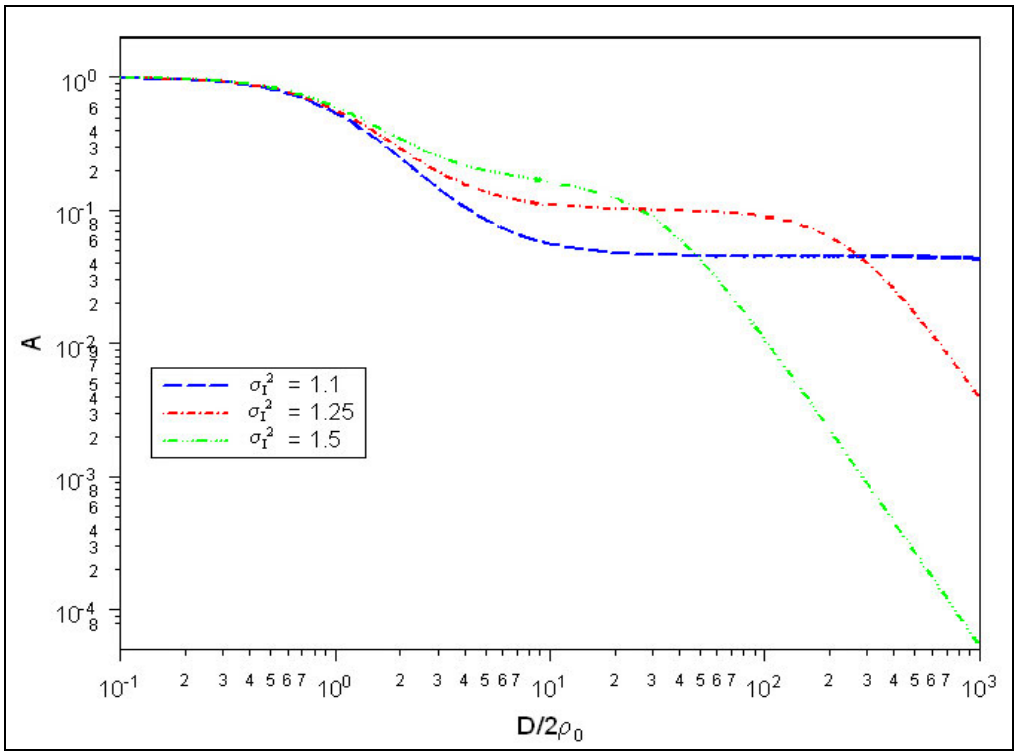

Fig. 4.1: The plane wave aperture averaging factor A vs. the ratio of the aperture radius $D/2$ to the transverse coherence length ρ_0, for L = 863 m and λ = 632.8 nm. The legend indicates different values of irradiance variance σ_I^2, where turbulence strength increases in the asymptotic limit of $\sigma_I^2 \to 1$.

The impact of the two scale sizes, the scattering disk and the transverse coherence length, is especially evident in the curves with $\sigma_I^2 = 1.25$ and 1.5 in Fig. 4.1. According to asymptotic theory, values of σ_I^2 closer to unity indicate stronger levels of turbulence. From Eq. (4.2), the width of the plateau, which is the separation of the two scales, may be determined. For $\sigma_I^2 = 1.5$, the width is 14.5. For $\sigma_I^2 = 1.1$, the separation is 1815, which indicates that the drop off in Fig. 4.1 is beyond the range of the chart. The location of the plateau is also at a lower value of A for $\sigma_I^2 = 1.1$.

The graphs for various irradiance variances in Fig. 4.1 show the trend of the aperture averaging factor in strong turbulence. Initially, there is more aperture

averaging in strong turbulence conditions, because A drops off faster in strong turbulence than in weak turbulence. At larger values of $D/2\rho_0$, plateaus form in the strong turbulence aperture averaging factor from the influence of the two-scale sizes, the transverse coherence length and the scattering disk size. The plateaus cause the aperture averaging factor to remain high over a wide range of aperture diameters, and allow the weak turbulence aperture averaging factor to catch up to the strong turbulence value. For most practical purposes, $D/2\rho_0$ will always be small enough so that the link will experience more aperture averaging in strong turbulence conditions.

4.2.2.2 Andrews Asymptotic Analysis for the Plane Wave

Andrews approached the theory of aperture averaging using the effective Kolmogorov spectrum and modified Rytov theory to determine a model for aperture averaging valid over the range of weak-to-strong scintillations. This approach will be fully developed in the following section. In the strong fluctuation region, the asymptotic relation of the irradiance variance for a plane wave to the Rytov variance developed from Prokhorov is used [20,27]:

$$\sigma_I^2 = 1 + \frac{0.86}{\left(\sigma_R^2\right)^{2/5}} \tag{4.7}$$

which is valid when $\sigma_I^2 >> 1$ and the spatial coherence radius, $\rho \approx 2\rho_0$, is larger than the inner scale, ℓ_o. The aperture averaging factor given by Eq. (4.7) has been plotted in Fig. 4.2 for a variety of irradiance variance values. Given a value of σ_I^2, Eq. (4.7) may be solved for C_n^2, from which the transverse coherence length for a plane wave is determined and substituted into Eq. (4.6) to calculate A. This model for A reduces the width of the plateau on the aperture averaging curve.

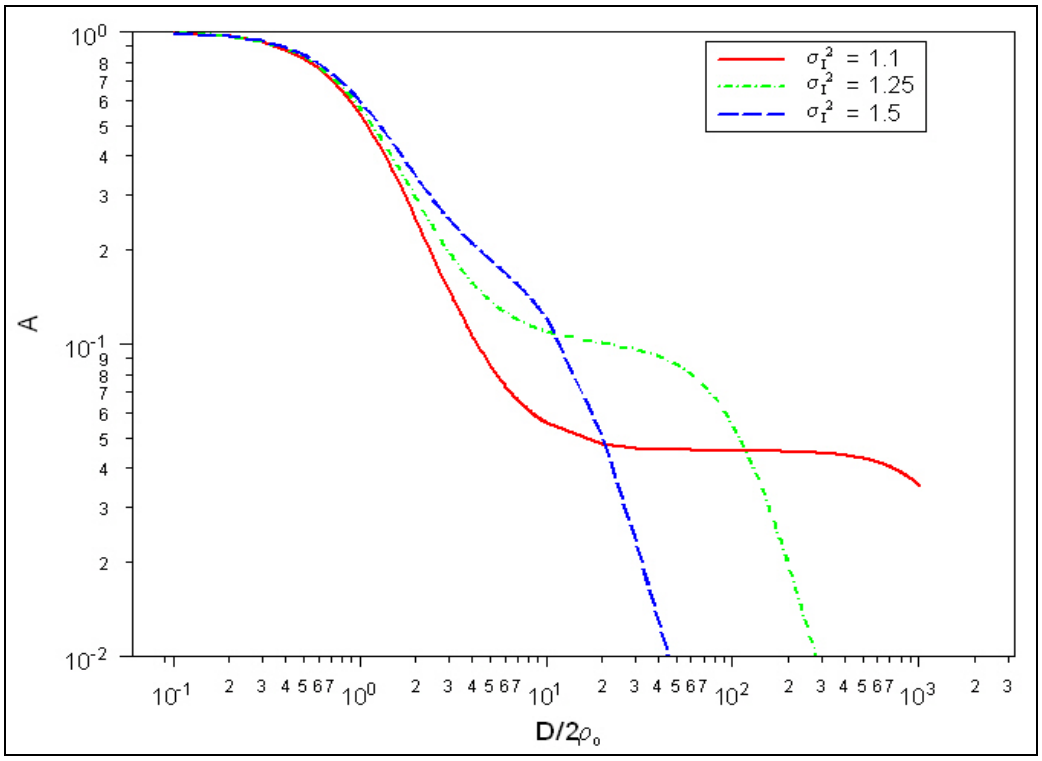

Fig. 4.2: Aperture averaging factor using the Andrews asymptotic model vs. the ratio of aperture radius to the transverse coherence length.

4.2.2.3 Scintillation Index (SI) Model for the Plane Wave

Andrews and Philips developed a model to describe plane wave characteristics over the entire range of fluctuation conditions, from weak to strong turbulence [33]. They use the effective Kolmogorov spectrum, which modifies the Kolmogorov spectrum by two filter functions to exclude mid-scale sizes that have an insignificant effect on the propagating wave in the moderate-to-strong turbulence region. The effective Kolmogorov spectrum model is [20,33]:

$$\Phi_{n,\ell}(\kappa) = 0.033 C_n^2 \kappa^{-11/3} \left[G_x(\kappa) + G_y(\kappa) \right] \tag{4.8}$$

where the large-scale filter function that passes only spatial frequencies $\kappa < \kappa_x$ is:

$$G_x(\kappa) = \exp\left(-\frac{\kappa^2}{\kappa_x^2} \right) \tag{4.9}$$

and the small-scale filter function, passing only spatial frequencies $\kappa > \kappa_y$, is:

$$G_y(\kappa) = \frac{\kappa^{11/3}}{(\kappa + \kappa_y)^{11/6}} \tag{4.10}$$

Likewise, modified Rytov theory may be used to define the scintillation index, σ_I^2, in terms of large-scale and small-scale scintillations [20,33]:

$$\sigma_I^2 = \exp\left(\sigma_{\ln x}^2 + \sigma_{\ln y}^2\right) - 1 \tag{4.12}$$

where $\sigma_{\ln x}^2$ and $\sigma_{\ln y}^2$ are the large-scale and small-scale log irradiance fluctuations. These functions are evaluated in Ref. [33], to define the scintillation index for a plane wave, excluding inner scale effects, as:

$$\sigma_I^2(L) = \exp\left[\frac{0.49\sigma_R^2}{\left(1+1.11\sigma_R^{12/5}\right)^{7/6}} + \frac{0.51\sigma_R^2}{\left(1+0.69\sigma_R^{12/5}\right)^{5/6}}\right] - 1 \tag{4.13}$$

where σ_R^2 is the Rytov variance for a plane wave. Eq. (4.13) reduces to the Rytov approximation in weak turbulence conditions, while it reduces to the Andrews asymptotic model in saturated strong turbulence conditions.

4.2.2.4 Comparison of Strong Turbulence Models for the Plane Wave

The three irradiance variance models, along with weak turbulence theory ($\sigma_I^2 = \sigma_R^2$), are plotted in Fig. 4.3. The Andrews and Churnside asymptotic models follow a similar trend, with the Andrews asymptotic model matching the scintillation index model when $\sigma_R^2 > 36$ [33]. In the weak-to-moderate fluctuation regime with $0.5 < \sigma_R^2 < 2$, the scintillation index model has a lower slope than what weak turbulence theory would predict. It is well known that weak turbulence theory is most accurate

when $\sigma_R^2 = \sigma_I^2 < 0.3$, and the scintillation index model accounts for the deviation of data in this region from weak turbulence theory.

The coherence length is expected to follow asymptotic behavior in the saturation region. When the irradiance variance σ_I^2 approaches 1, asymptotic theory predicts that the transverse coherence length will become infinitely small. This would require the presence of unreasonably high turbulence levels on the link. Fig. 4.4 shows the behavior of the transverse coherence length based on three different models for the irradiance variance in strong turbulence. The scintillation index model is plotted in the onset-of-strong turbulence region, where $0.5 < \sigma_R^2 < 2$. In the onset of strong turbulence, ρ_0 is in the range of 2 mm to 6 mm for a path length of 863 m and λ = 632.8 nm.

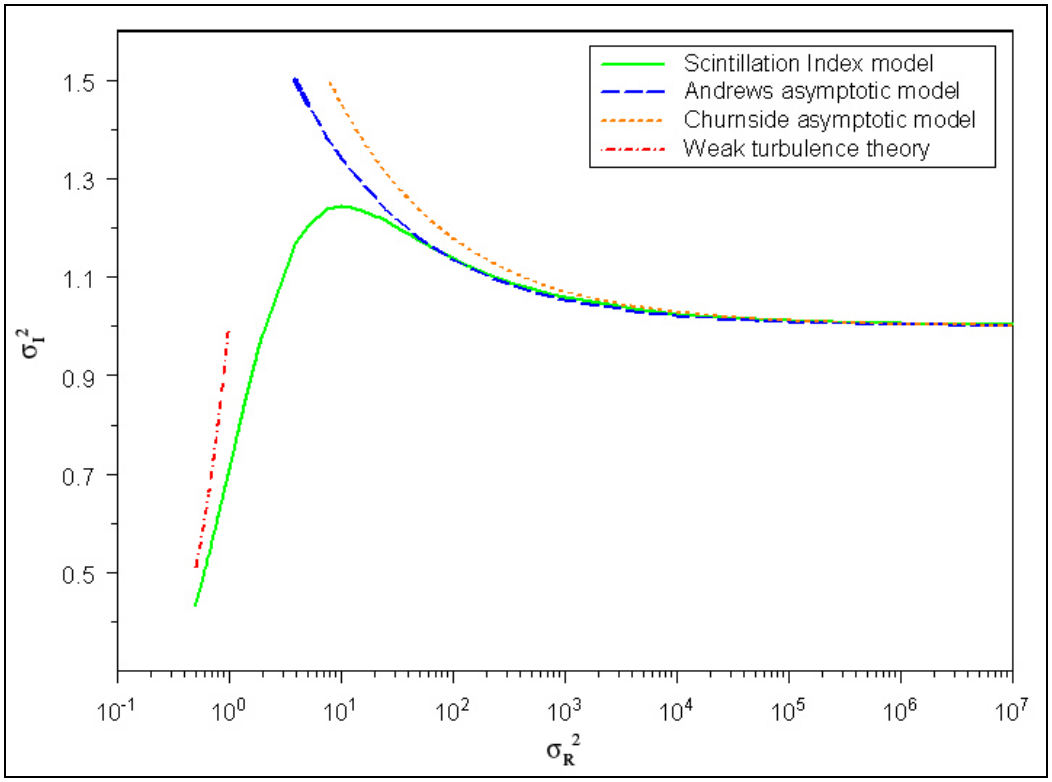

Fig. 4.3: Irradiance variance, or scintillation index, of a plane wave versus Rytov variance. Asymptotic models in the saturation region are shown.

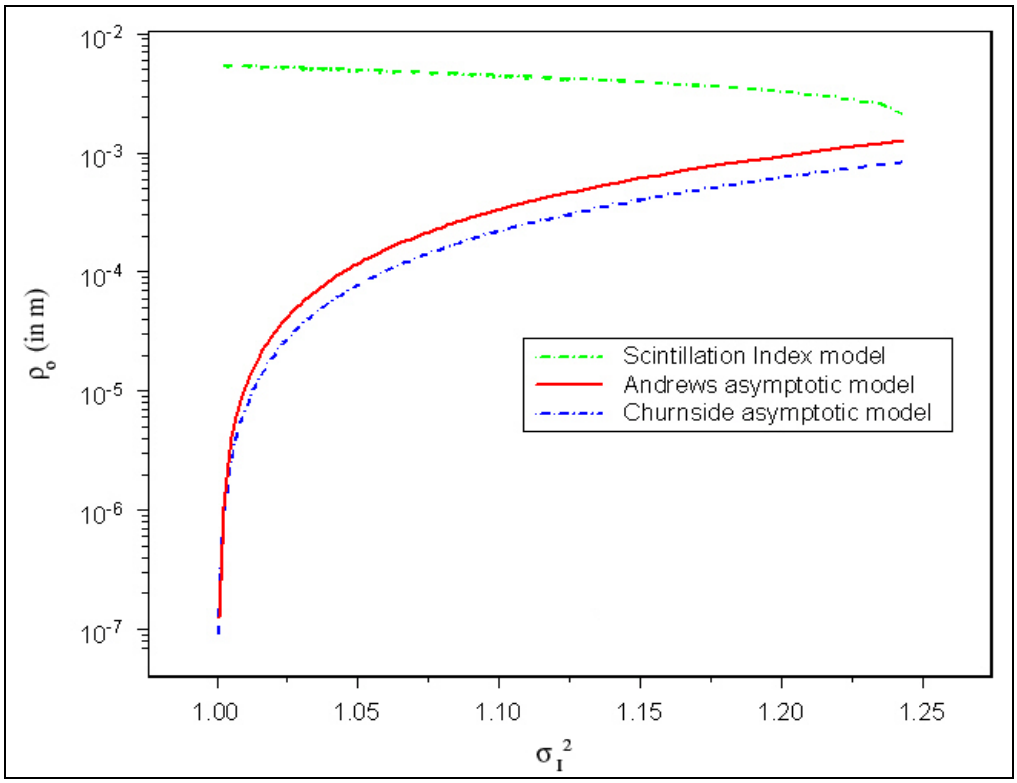

Fig. 4.4: Transverse coherence length based on strong turbulence models plotted against irradiance variance, σ_I^2.

4.2.3 Spherical Wave Analysis

4.2.3.1 Churnside Asymptotic Analysis for the Spherical Wave

Aperture averaging theory for spherical wave propagation with small inner scale is also evaluated using asymptotic theory as in Sec. 4.2.2.1. The spherical wave analysis uses the same covariance function as presented in Eq. (4.1), although N_3, b_1, and b_2 take on spherical wave representations. The transverse coherence length for the spherical wave is defined by:

$$\rho_0 = \left(0.545k^2LC_n^2\right)^{-3/5} \tag{4.14}$$

The coefficient in Eq. (4.14) is the only difference between the plane and spherical wave cases, otherwise the behavior of ρ_0 is the same. The constant N_3 also takes on a new value of 3.86 for the spherical wave case. The two scale functions b_1 and b_2 are also modified from the plane wave situation, although their behavior as ρ goes to zero and infinity are the same. For negligible inner scale, the irradiance variance is related to ρ_0 by [11]:

$$\sigma_I^2 = 1 + 3.86\left(\frac{k\rho_0^2}{L}\right)^{1/3} \tag{4.15}$$

The irradiance variance is related to the plane wave Rytov variance σ_R^2 by using the form presented in Eq. (2.36).

Churnside evaluated the strong turbulence spherical wave aperture averaging factor as a sum of two terms which are strongly influenced by b_1 and b_2 in the evaluation of the covariance equation [11]:

$$\begin{aligned} A_1 &= \frac{16}{\pi}\frac{\sigma_I^2+1}{2\sigma_I^2}\int_0^1 dyy\left[\cos^{-1}y - y\left(1-y^2\right)^{1/2}\right]\exp\left[-\left(\frac{Dy}{\rho_0}\right)^{5/3}\right] \\ A_2 &= 3.66\left(\frac{2L}{kD\rho_0}\right)^{7/3}\frac{\sigma_I^2-1}{2\sigma_I^2}\int_0^\infty duu^{-2/3}J_1^2(u)\int_0^1 dxx^2(1-x)^{-1/3} \\ &\qquad \times\exp\left[-\left(\frac{2L}{kD\rho_0}\right)^{5/3}u^{5/3}x^{5/3}\right] \end{aligned} \tag{4.16}$$

As in Eq. (4.15), the term A_1 represents scale sizes smaller than ρ_0, while the term A_2 represents scale sizes larger than the scattering disk, $L/k\rho_0$. The total aperture averaging factor is $A=A_1+A_2$, and is given by [11]:

$$A = \frac{\sigma_I^2 + 1}{2\sigma_I^2}\left[1 + 0.908\left(\frac{D}{2\rho_0}\right)^2\right]^{-1} + \frac{\sigma_I^2 - 1}{2\sigma_I^2}\left[1 + 0.613\left(\frac{kD\rho_0}{2L}\right)^{7/3}\right]^{-1} \tag{4.17}$$

Eq. (4.17) is plotted for various values of irradiance variance in Fig. 4.5 below. The separation of scale sizes for the spherical wave case, calculated from the width of the plateau, is wider than in the plane wave case. For $\sigma_I^2 = 1.1$, the Fresnel zone size is $240\rho_0$, and the width of the plateau is beyond the range of the graph at 57512. When $\sigma_I^2 = 1.25$, the Fresnel zone size is smaller at $60.6\rho_0$, and the plateau width is 3681. For $\sigma_I^2 = 1.5$, the Fresnel zone size is $21.4\rho_0$, and the plateau width is 460. As in the plane wave case, larger irradiance variances show higher plateaus in A.

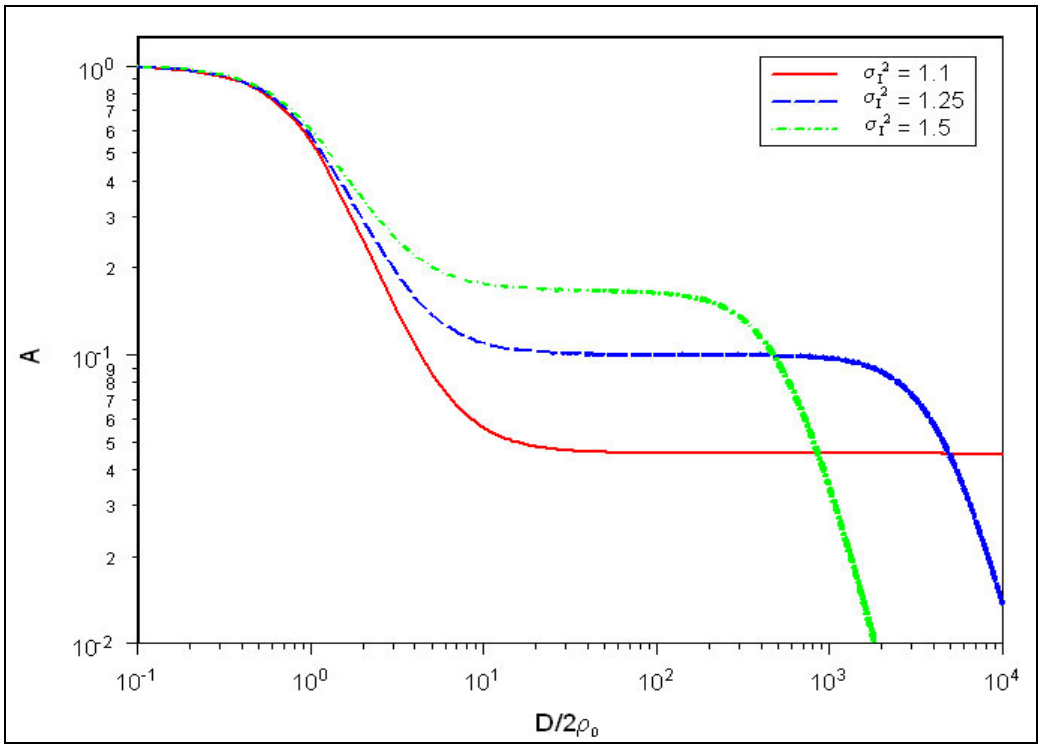

Fig. 4.5: Churnside approximate aperture averaging factor plotted against the ratio of the aperture radius to the transverse coherence length, for $\sigma_I^2 = 1.1$, 1.25, and 1.5. Curves calculated for an AVW test range path length of 863 m.

4.2.3.2 Andrews Asymptotic Analysis for the Spherical Wave

Andrews used the Kolmogorov spectrum to relate the irradiance variance in the saturation region to the plane wave Rytov variance σ_R^2 [11]:

$$\sigma_I^2 = 1 + \frac{2.73}{\left(\sigma_R^2\right)^{2/5}} \tag{4.19}$$

where $\sigma_I^2 >> 1$. This asymptotic model predicts a transverse coherence length that is different from the Churnside asymptotic model by a factor of 2.74. This coherence length is then used in the aperture averaging factor model given by Eq. (4.17). The shift in the aperture averaging factor from its value given by the Churnside model is visible in Fig. 4.6. The plateaus are also narrower than those of the Churnside model. The Andrews asymptotic analysis is a good fit to the scintillation index model for a spherical wave, which will be presented in Sec. 4.2.3.3.

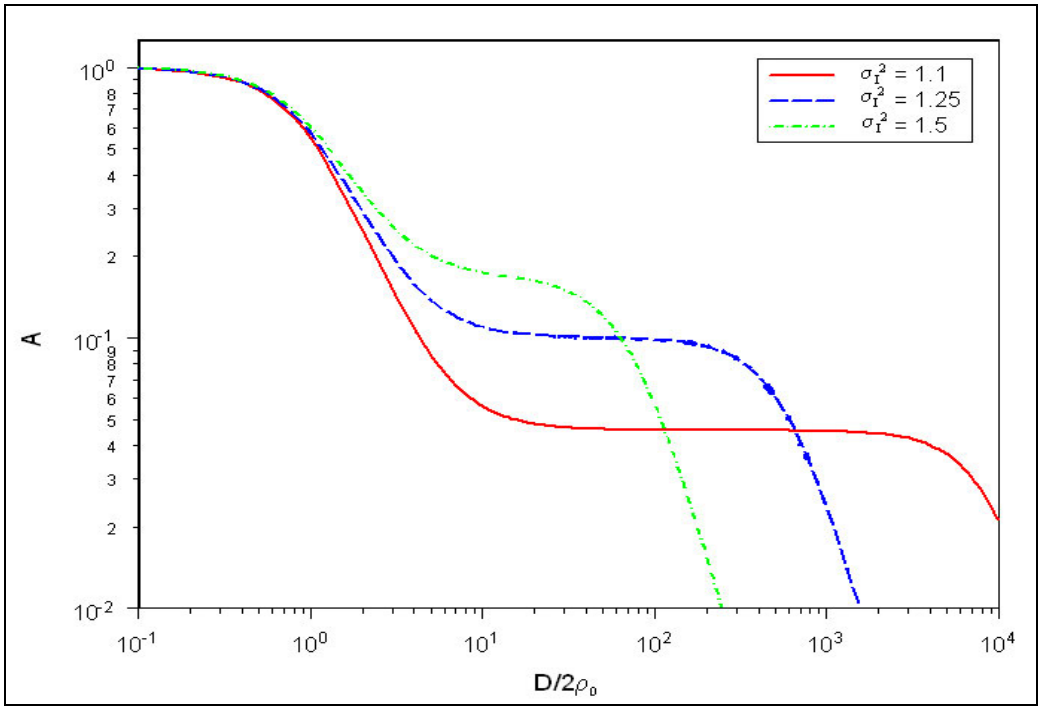

Fig. 4.6: Andrews asymptotic model for the spherical wave plotted against the ratio of the aperture radius to the transverse coherence length.

4.2.3.3 Scintillation Index (SI) Model for the Spherical Wave

The scintillation index model attempts to describe the behavior of irradiance fluctuations over the entire range of turbulence strengths. The model for a spherical wave is developed using the effective Kolmogorov spectrum, using the same filter functions as presented in Eqs. (4.9) and (4.10) for the plane wave case. The small scale and large scale log irradiance fluctuations are evaluated to define the scintillation index of a spherical wave, neglecting inner scale effects, by [20]:

$$\sigma_I^2(L) = \exp\left[\frac{0.20\sigma_R^2}{\left(1+0.19\sigma_R^{12/5}\right)^{7/6}} + \frac{0.20\sigma_R^2}{\left(1+0.23\sigma_R^{12/5}\right)^{5/6}}\right] - 1 \qquad (4.20)$$

where σ_R^2 is the plane wave Rytov variance.

4.2.3.4 Comparison of Strong Turbulence Models for the Spherical Wave

Both asymptotic models, along with the scintillation index model and weak turbulence theory, are plotted in Fig. 4.7. As in the plane wave case, the asymptotic models are similar, with the Andrews model matching the scintillation index model when $\sigma_R^2 > 64$. In the onset of strong scintillation region, where $0.5 < \sigma_R^2 < 2$, the scintillation index model has a lower slope than that predicted by weak turbulence theory.

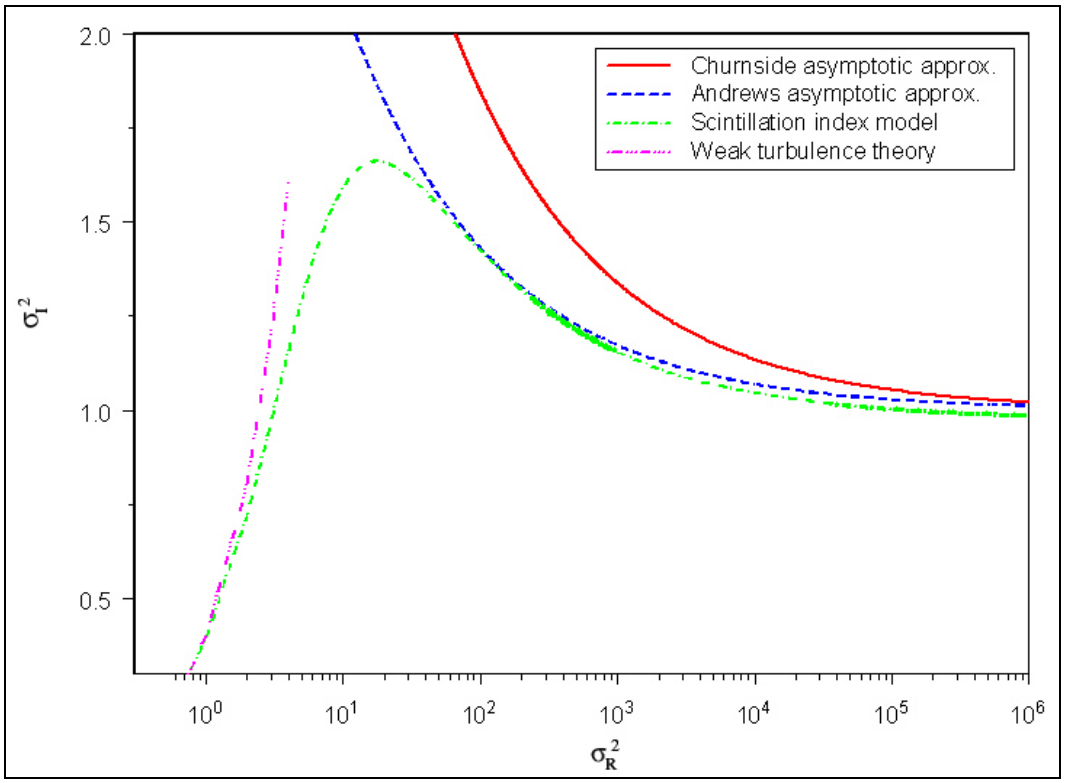

Fig. 4.7: Spherical wave irradiance variance plotted as a function of plane wave Rytov variance. Asymptotic and weak turbulence relations are indicated.

The transverse coherence length also behaves asymptotically in the saturation region. Figure 4.8 shows that ρ_0 becomes infinitely small as $\sigma_I^2 \to 1$. The scintillation index model predicts values of ρ_0 in the range of 1 mm to 1 cm. In the saturated region, the scintillation index model follows the Andrews asymptotic model. The asymptotic models predict that for strong saturation conditions, the transverse coherence length becomes very small (0.1 mm to 0.001 mm) for path lengths on the order of the range used in this experiment.

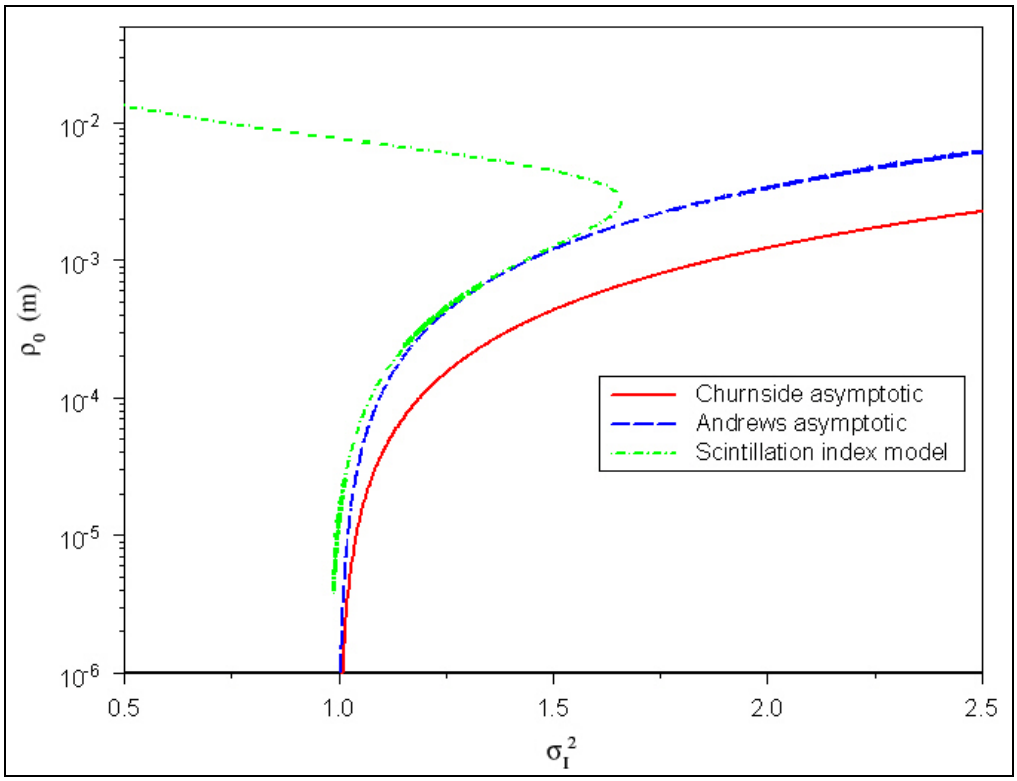

Fig. 4.8: Behavior of the transverse coherence length in the strong fluctuation region, plotted as a function of the plane wave Rytov variance.

4.3 Aperture Averaging Experiment

4.3.1 Experimental setup

Strong turbulence aperture averaging data was collected over multiple days along the 863 m AVW-Chesapeake test range. The only valid experimental method for determining the aperture averaging factor in strong turbulence is to directly measure the irradiance variance of a propagating wave [40]. Unlike the situation in weak turbulence, there is no way of equating the irradiance variance to the log-irradiance variance in strong turbulence. On this test range, measured intensity variance values ranged from 1.01 to 1.35; however, a sufficiently large data set is available only at $\sigma_I^2 =$ 1.1.

The transmitter and receiver systems are the same as those used in the weak turbulence aperture averaging experiment, presented in Section 3.3.1. Aperture diameters ranging from 1 cm to 16 cm were used; however, due to atmospheric variations during the data collection period, not all available aperture diameters produced data in strong turbulence conditions.

Data was collected during clear weather conditions. Winds ranged from 1 m/s to 4.5 m/s, with low relative humidity (less than 50%). Temperatures ranged from 60°F to 83°F. Strong turbulence values were always measured in daylight.

4.3.2 LabVIEW Data Acquisition

Data acquisition for the strong turbulence case proceeded in the same manner as for the weak turbulence case, which was presented in Section 3.3.2. The LabVIEW program was shown in Fig. 3.7, and outputs the same 13 data values presented in Table 3.1. Received intensity was sampled in LabVIEW at 3000 samples/sec, with intensity variance values averaged over 1 minute intervals. The 1 minute averaging time allowed for more accurate measurements. Data is sorted according to the measured irradiance variance of the scintillometer channel. Data is then grouped by irradiance variance value and separated into two regions: weak irradiance fluctuations, $\sigma_I^2 < 1.0$, and strong irradiance fluctuations, $\sigma_I^2 > 1.0$.

4.4 Experimental Results for the Plane Wave Case

Data was analyzed by the process described in Section 4.2.1. The Fresnel zone size is 9.32 mm, and the scattering disk is $8.69 \cdot 10^{-5}/\rho_0$. To neglect inner scale effects, $\ell_o \leq \rho_0$ and $\rho_0 < (L/k)^{1/2}$. As in the weak turbulence case, we expect the spherical wave

analysis to be in better agreement with the theory, due to the divergence of the laser beam.

New data is plotted in Fig. 4.9 using the Churnside asymptotic value for ρ_0. The data plotted has an average σ_I^2 ranging from 1.07 to 1.12. Therefore, the mean data should follow the solid line for $\sigma_I^2 = 1.1$. Error bars represent one standard deviation of the measured values. Since ρ_0 is calculated from measured values of irradiance variance, it also has a range of values within one standard deviation of the mean. The asymptotic theory curve seems to underpredict the aperture averaging factor, thereby overestimating the amount of aperture averaging that is taking place in strong turbulence. In the plateau region, near $D/2\rho_0 = 350$, the experimental aperture averaging factor is 43% higher than the value predicted by the model.

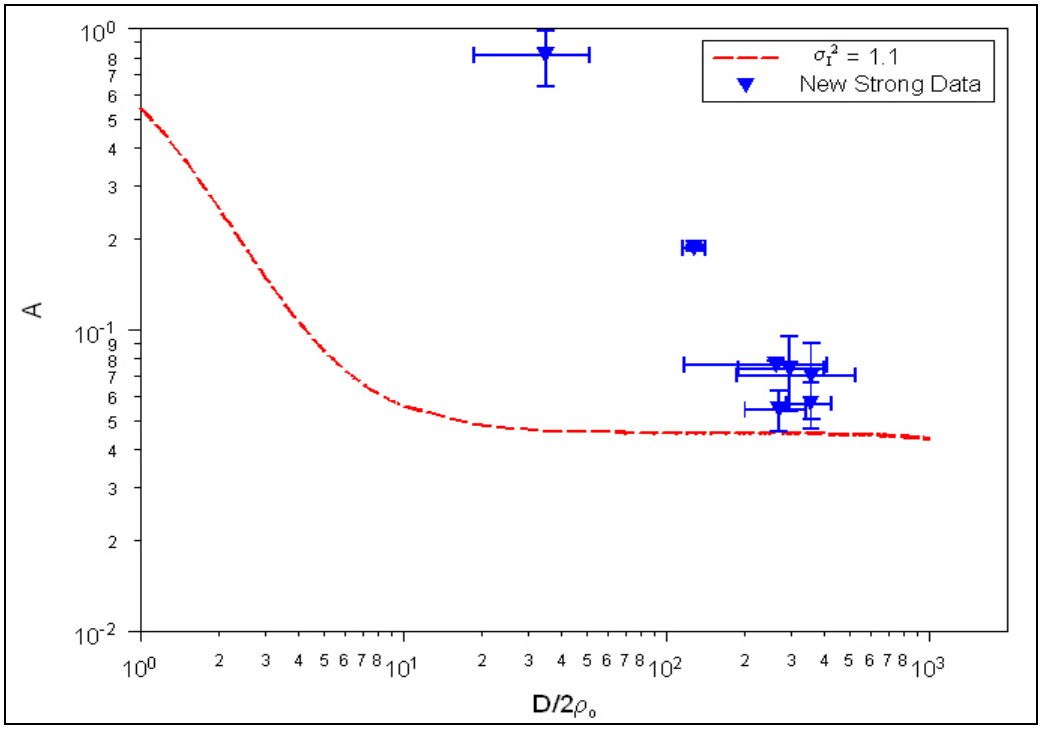

Figure 4.9: Average aperture averaged data in strong turbulence using Churnside asymptotic analysis plotted against the ratio of the aperture radius to the transverse coherence length. Churnside asymptotic analysis predicts $C_n^2 = 9.3\times10^{-12}$ m$^{-2/3}$.

As mentioned previously, the direct measurement of the intensity to determine σ_I^2 is the only valid method for determining aperture averaging in strong turbulence [40]. In the absence of independent measurements of C_n^2 by an non-saturating incoherent scintillometer [11,24], the asymptotic model presented in Sec. 4.2.2.1 was used to extract values for σ_R^2 and ρ_0. Typical values of ρ_0 in weak to non-saturated strong turbulence are on the order of 1 mm. Using measured data values the asymptotic model predicts ρ_0 in the order of 0.01 mm to 0.1 mm for saturated strong turbulence, along with values of C_n^2 averaging 9.3×10^{-12} $m^{-2/3}$. These values are consistent with those expected experimentally, since very long propagation paths have very small transverse coherence lengths [42].

New data is plotted in Fig. 4.10 using the Andrews asymptotic relation of Eq. (4.7). The only difference between this data and the data plotted using the Churnside asymptotic representation in Fig. 4.9 is that the data is left-shifted on the x-axis by a factor of 1.52. There is a small constant offset between Eqs. (4.2) and (4.7), leading to this shift. Once again, the data clustered near $A = 0.06$ appears to exhibit a plateau effect. The Andrews asymptotic model gives $\rho_0 = 0.39$ mm and $C_n^2 = 5.7\times10^{-12}$ $m^{-2/3}$ for this data.

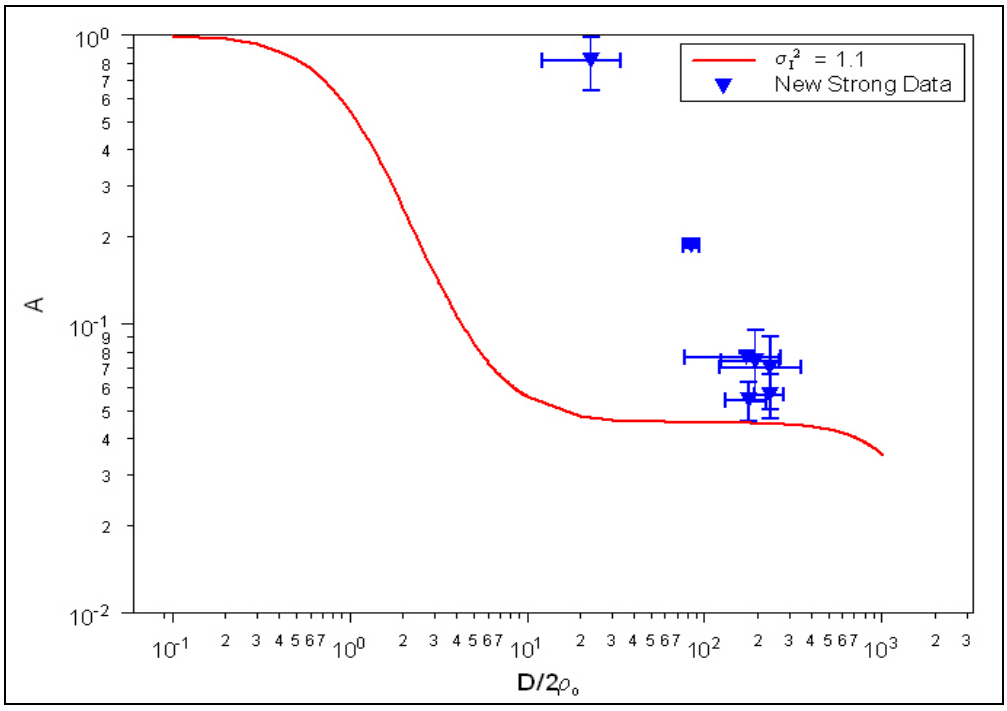

Fig. 4.10: New data using the Andrews asymptotic theory plotted against the ratio of the aperture radius to the transverse coherence length. The solid line represents the aperture averaging factor given by the Andrews asymptotic theory for $\sigma_I^2 = 1.1$.

We previously introduced an expression for irradiance variance σ_I^2 based on σ_R^2 that is valid over all turbulence conditions, with inner scale effects neglected. This is the scintillation index (SI) model. In order to determine the transverse coherence length from Eq. (4.3), we have interpolated values of σ_I^2 based on σ_R^2 for the rising portion of the scintillation index curve shown in Fig. 4.3. Therefore, the data is analyzed assuming strong turbulence without saturation, giving a value for ρ_0 that is consistent with the conditions on the experimental test range. This new data is presented in Fig. 4.11, along with scintillation index model curves using saturated and non-saturated values of the Rytov variance for $\sigma_I^2 = 1.1$.

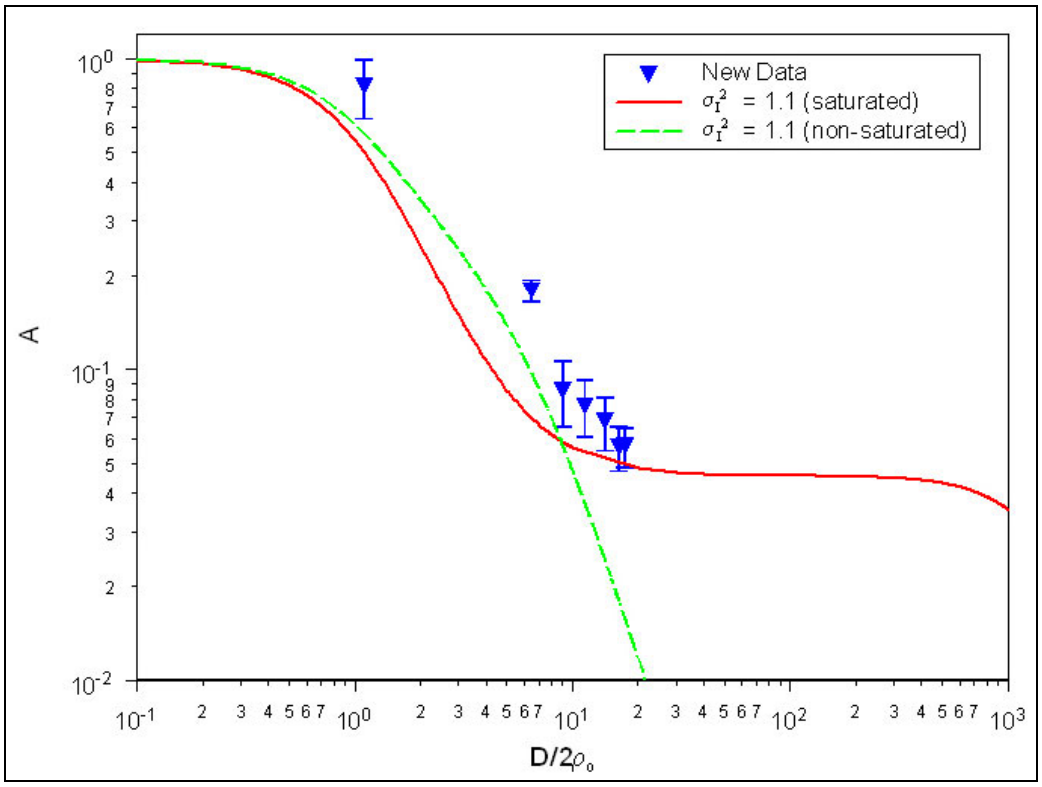

Fig. 4.11: New aperture averaging data calculated using the SI model plotted against the ratio of aperture radius $D/2$ to the transverse coherence length ρ_0 for a plane wave propagating in strong turbulence. The curves represent the aperture averaging factor given saturated and non-saturated strong turbulence values for σ_R^2.

The new data in Fig. 4.11 is in better agreement with theory, and visibly follows the predicted trend for $\sigma_I^2 = 1.1$. Using the scintillation index model to find a Rytov variance of $\sigma_R^2 \approx 2.9$ when $\sigma_I^2 = 1.1$, the transverse coherence length is found to be $\rho_0 \approx 4.4$ mm. The turbulence strength average is $C_n^2 = 8.4\times10^{-14}$ m$^{-2/3}$. Since our data was not acquired under strong saturation conditions [42], our receive aperture on the scintillometer channel with $D = 5$ mm is sufficient to avoid aperture averaging effects.

4.5 Experimental Results for the Spherical Wave Case

Strong turbulence data for the spherical wave case was acquired through the process presented in Section 4.3. Using the models presented in Section 4.2.3, we can compare measured aperture averaging data with that of the theoretical approximations for the spherical wave case. The Fresnel zone size is 9.32 mm, while the typical transverse coherence length was near 7 mm, indicating that we are within the strong turbulence region.

New data with $\sigma_I^2 \approx 1.1$ is shown in Fig. 4.12 using the Churnside asymptotic model, presented in Section 4.2.3.1, to determine ρ_0. The approximate formula from Eq. (4.17) is also plotted in Fig. 4.11, for $\sigma_I^2 = 1.1$. The data is slightly higher than what the approximate formula for $\sigma_I^2 = 1.1$ predicts. The Churnside asymptotic model predicts $\rho_0 \approx 0.04$ mm and $C_n^2 = 7.2 \times 10^{-10}$ m$^{-2/3}$ when $\sigma_I^2 = 1.1$. The predicted C_n^2 indicates very strong turbulence because the asymptotic model assumes strong saturation conditions that force the transverse coherence length to be a very small value, on the order of 0.01 mm. The drawbacks of the asymptotic model are explained in more detail later in this chapter.

The Andrews asymptotic relationship for the transverse coherence length was used to plot the aperture averaging factor in Fig. 4.13 for $\sigma_I^2 \approx 1.1$. Eqs. (4.14) and (4.19) were used to determine ρ_0 for this set of data. As with the Churnside asymptotic analysis, the data is higher than what the asymptotic approximations predict. The Andrews model predicts the transverse coherence length for this path to be on the order of 0.1 mm. Andrews asymptotic analysis estimates the level of turbulence at $C_n^2 = 1.2 \times 10^{-10}$ m$^{-2/3}$.

In the case of both asymptotic relations, the Churnside and Andrews asymptotic models predict that A will always be much less than 1 for an aperture diameter of any reasonable size. In order to measure A near 1, the receiver aperture diameter must be on the order of the saturated value of ρ_0, which ranges from 0.01 mm to 0.1 mm. The residual value in Figs. 4.12 and 4.13 is that they clearly show that this data was not taken in saturated strong turbulence conditions. The two data points located at $A = 0.78$ and $A = 0.18$ would not have been measured if the turbulence was saturated. The rest of the data points indicate a plateau effect, although the mean of those five points is about 36% higher than the asymptotic model values at $D/2\rho_0 = 2000$. Recall that the discrepancy between the Churnside and Andrews asymptotic models is that ρ_0 in the Andrews model is a factor of 2.74 larger than that of the Churnside asymptotic model.

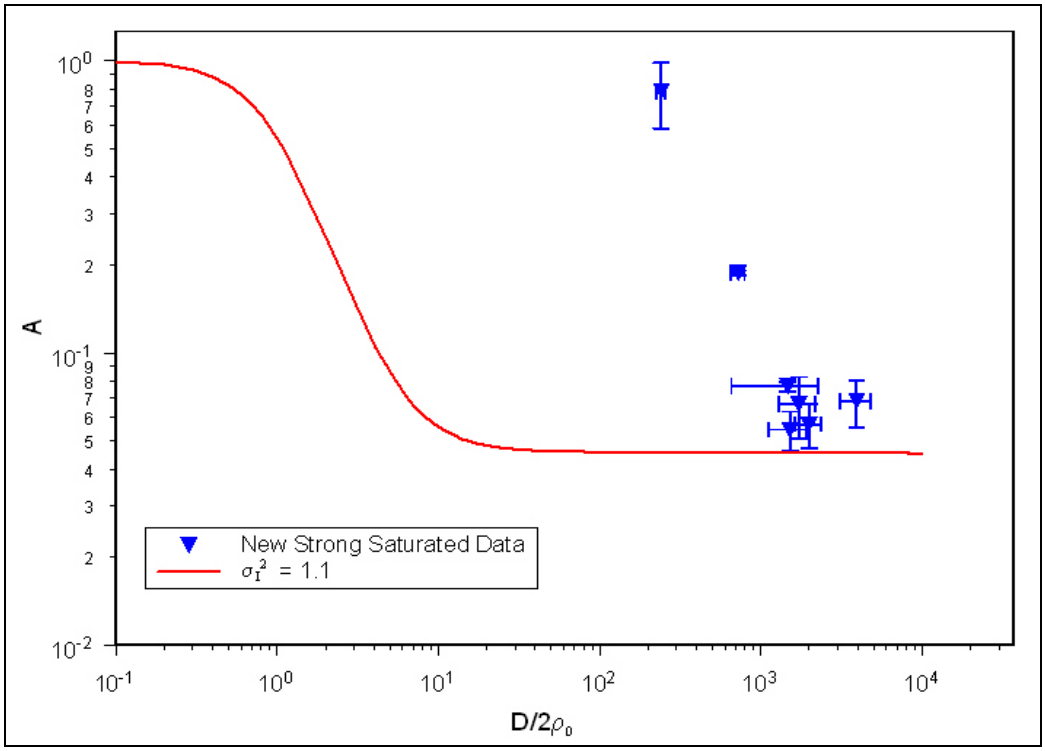

Fig. 4.12: New strong turbulence data analyzed using the Churnside asymptotic method for a spherical wave, with irradiance variances near 1.1.

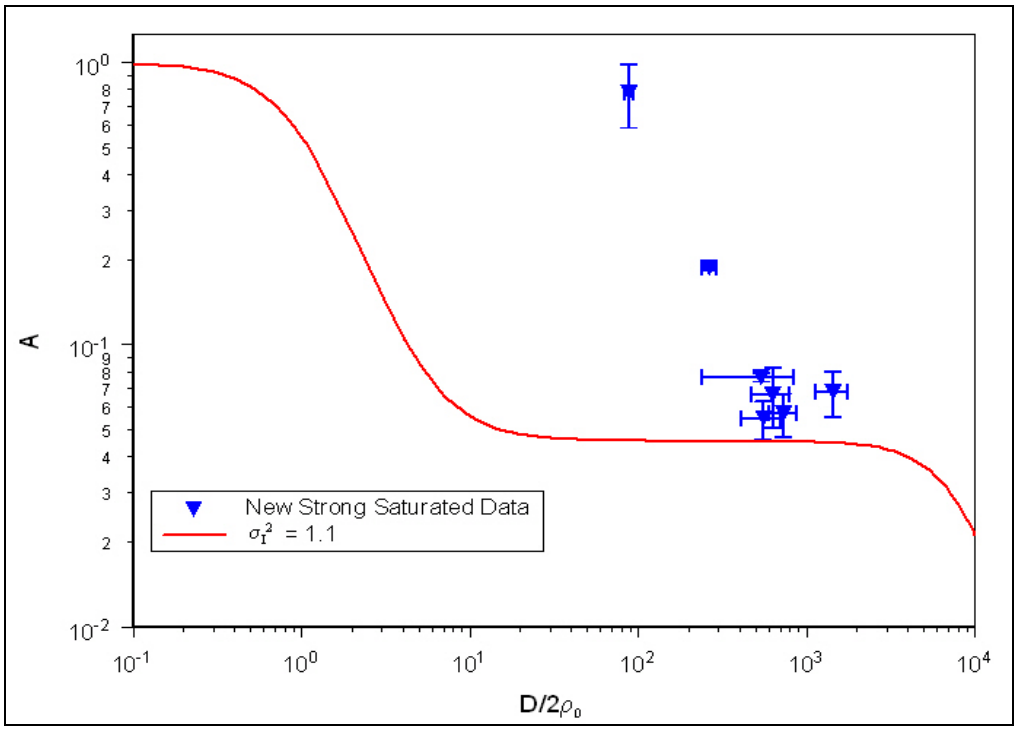

Fig. 4.13: New strong turbulence data plotted using the Andrews asymptotic model for the spherical wave from Eq. (4.19). The curve represents the Andrews asymptotic model aperture averaging factor for $\sigma_I^2 = 1.1$.

To address the shortcomings of the asymptotic theories, the scintillation index model for the irradiance variance in Eq. (4.20) was used to analyze the experimental data in a non-saturation strong turbulence region. The ρ_0 for $\sigma_I^2 = 1.1$ was near 7 mm, putting us well within the strong turbulence region on this path. This corresponds to an average $C_n^2 = 8.4\times10^{-14}$ m$^{-2/3}$. Fig. 4.14 shows the mean data plotted with the approximation to the aperture averaging theory when $\sigma_I^2 = 1.1$. The data appears to show a tapering off and potentially a plateau area near $D/2\rho_0 = 10$, similar to that predicted by the approximate curve. This is consistent with the turbulence working to render scale sizes larger than ρ_0 ineffective along the path.

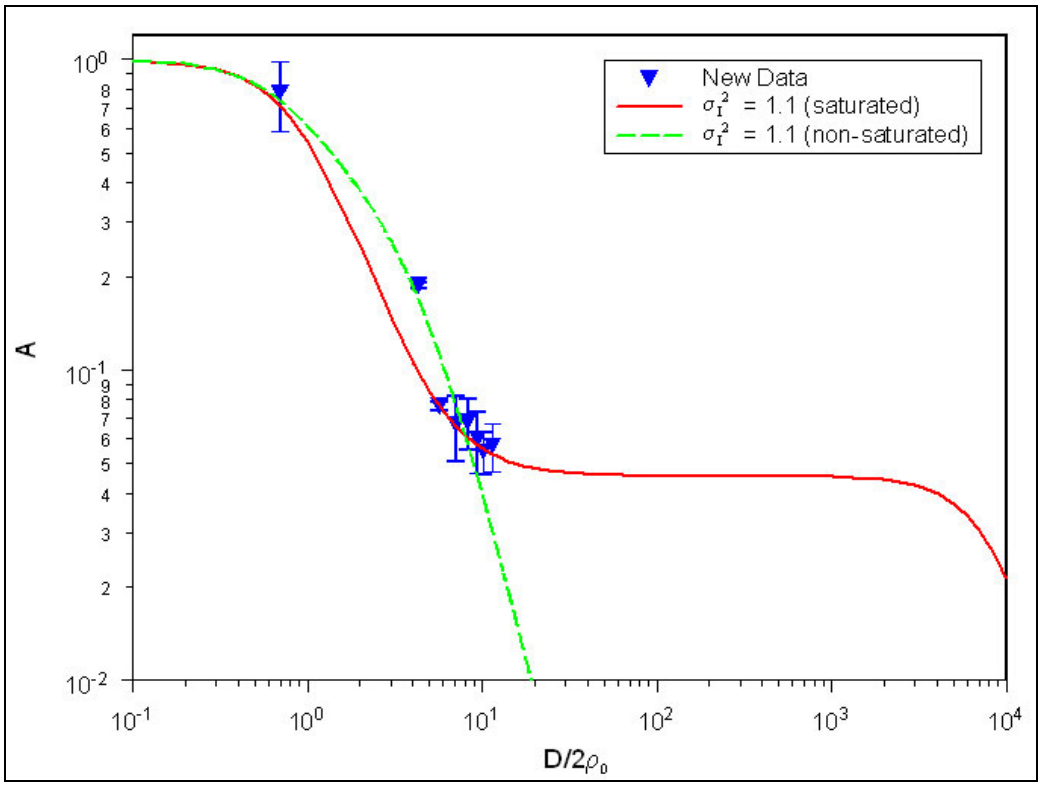

Fig. 4.14: Mean data with error bars plotted against the ratio of the aperture radius to the transverse coherence length. The solid line is the aperture averaging approximation in Eq. (4.17) for $\sigma_I^2 = 1.1$.

The new data using the asymptotic and SI models have been plotted along with the Churnside experimental data in Figs. 4.15 and 4.16. The Churnside data is the only well-accepted set of aperture averaging data in strong turbulence. The Churnside data was taken by propagating a HeNe laser over a 1000 m path, with an average irradiance variance of 3.08 ± 0.38. The Churnside asymptotic curve for $\sigma_I^2 = 3.08$ is shown in Fig. 4.15 to contrast with the Churnside data. Data for six apertures was collected simultaneously; and C_n^2 was measured over a 250 m path, adjacent to the 1000 m aperture averaging path, using an incoherent scintillometer. The inability to measure C_n^2 over the same path as A calls into question the true path-averaged nature of the turbulence data. The average C_n^2 measured was $1.29 \pm 0.39 \times 10^{-12}$ m$^{-2/3}$, and $\rho_0 = 1.74$

mm ± 0.24 mm. The Churnside data is limited in breadth, since Churnside did not have large enough apertures available to measure very small aperture averaging factors. This also limited their ability to see any scale size effects due to the size of turbulent eddies relative to ρ_0 and the scattering disk.

In a condition of strong saturated turbulence, the new data analysis using asymptotic theory in Fig. 4.15 results in data that is beyond the range of the Churnside data. Although the analyzed data demonstrates a plateau in reasonable agreement with approximate theory, the data should only be treated as an estimate of what could occur if the link experienced strong saturated turbulence, following the discussion presented earlier regarding Figs. 4.12 and 4.13. The new data reinforces the idea that it will be difficult to surpass the plateau and reach the scattering disk scale in saturated conditions; this would require an extremely large diameter receiver. By plotting the aperture averaging factor on the plateau, an aperture size near the ρ_0 scale may be chosen for a specific link, if it is required to work in saturated scintillation conditions.

As mentioned previously, the ρ_0 and scattering disk scale sizes result in a plateau region in the aperture averaging factor for strong turbulence. The Churnside data does not show any scale effects, while the new aperture averaging data using the SI model (Fig. 4.16) begins to exhibit a tapering around $D/2\rho_0 = 10$, likely leading to a plateau. The new data is in good agreement with the predicted aperture averaging curve, even at higher values of A. The spherical wave treatment is also much improved over the plane wave analysis of Section 4.4, which is due to the beam divergence of the transmitter. Only the point at $A = 0.188$ and $D/2\rho_0 = 4.32$ in Fig. 4.16 does not include the

approximate theory for the aperture averaging factor within the error bars. This is due to a limited number of data points at that aperture size.

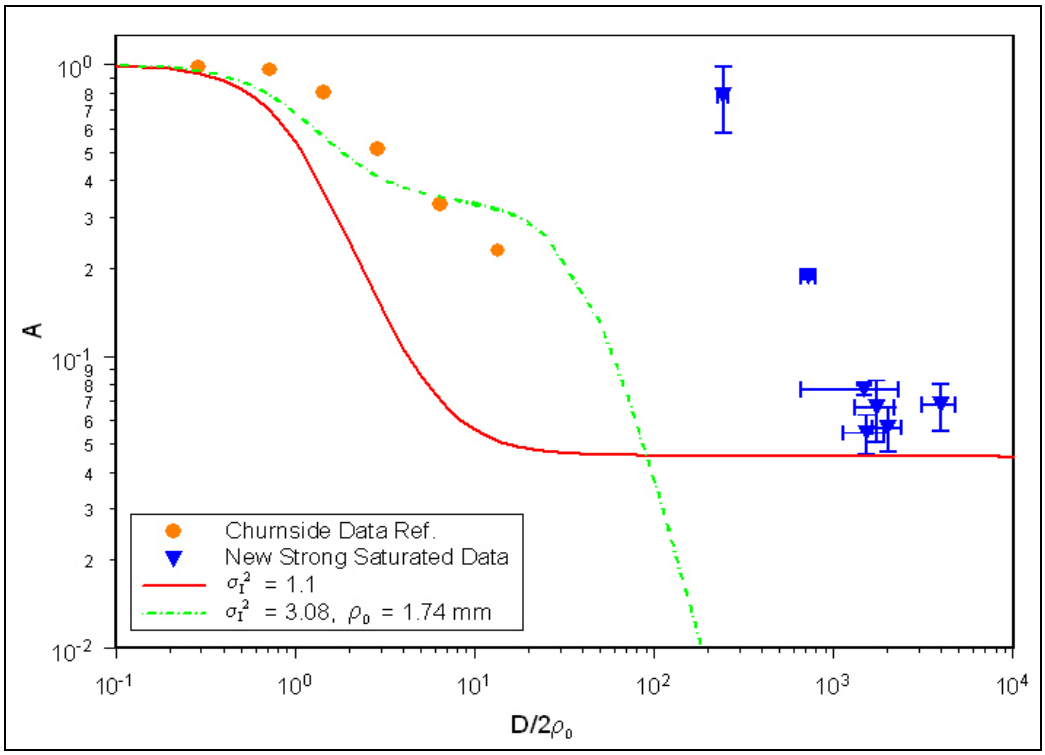

Fig. 4.15: Mean data analyzed with the Churnside asymptotic model, plotted along with the strong turbulence Churnside data taken over a 1000 m path.

The new data in Fig. 4.16 is shown with both the SI model curves for saturated and non-saturated strong turbulence at $\sigma_I^2 = 1.1$. The new data is in good agreement with both curves. Although Fig. 4.16 is beginning to show scale size effects, data for larger apertures is needed to discern the validity of these results. Given that the amount of strong turbulence data over this test range was limited, these results should encourage further experimental studies of aperture averaging in strong turbulence in order to improve the quality of theoretical models available in saturated and non-saturated strong atmospheric turbulence.

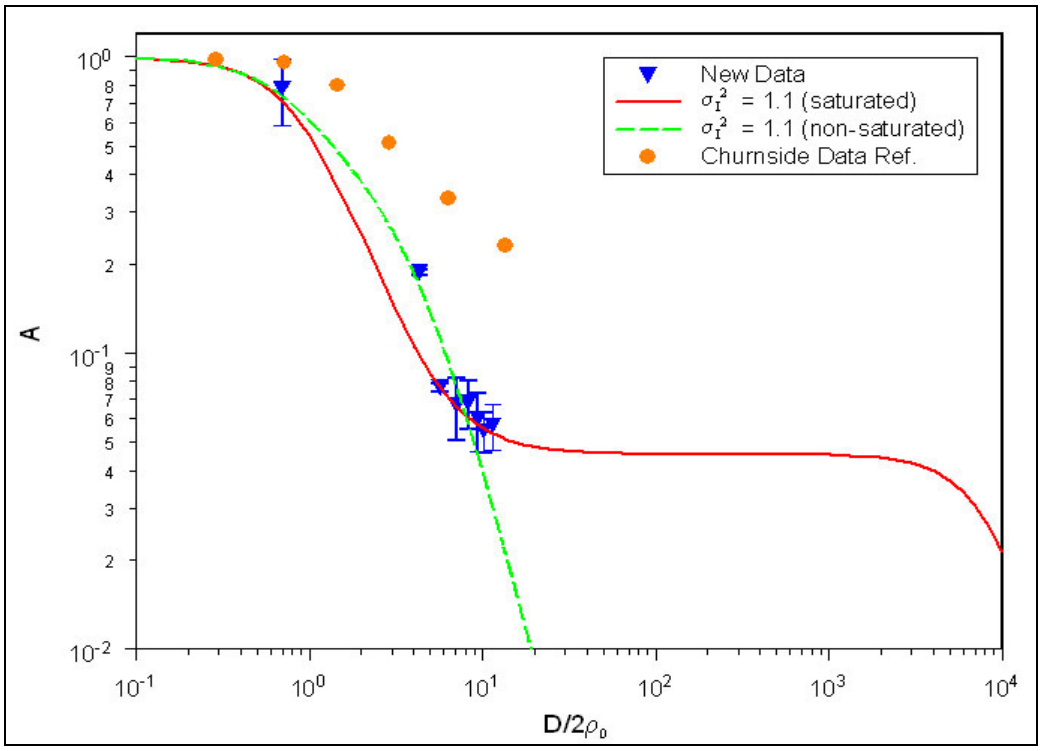

Fig. 4.16: Mean data analyzed using the scintillation index model in the non-saturated strong turbulence region, plotted along with the Churnside data for a 1000 m path. Saturated and non-saturated SI model curves for $\sigma_I^2 = 1.1$ are also shown.

4.5 Conclusions

Strong turbulence aperture averaging data, measured on an 863 m test range at the University of Maryland, College Park, has been analyzed using the Churnside Asymptotic, Andrews Asymptotic, and Scintillation Index models. The models are used to determine values for ρ_0 and σ_R^2, which otherwise could only be measured by using an incoherent light scintillometer. The SI model shows the best aperture averaging results for the spherical wave in strong turbulence. Due to the height of the propagation path above ground, it was difficult to acquire enough data points in strong turbulence conditions for analysis. The only large data set was available for $\sigma_I^2 = 1.1$. In spite of these limitations, this is the first set of strong turbulence aperture averaging data to be acquired in non-saturation conditions.

Chapter 5

Free Space Optical Communication using Nonimaging Optics

5.1 Introduction

Atmospheric turbulence adversely affects the propagation of optical waves. As we have investigated in the previous chapters, the atmosphere distorts the wavefront and produces intensity scintillations. Another manifestation of the interaction of atmospheric turbulence with an optical wave is the receiver spot wander in the focal plane. High speed optical receivers use photodetectors with diameters on the order of 10s of microns. In an on-off keyed transmission system, achieving a good bit error ratio (BER) requires that a maximum amount of received light is received by the photodetector. When turbulence induced beam wander moves the focal spot, there is a definite increase in the BER. Commercial systems for data transmission typically require a BER of 10^{-9} or better [43]. Minimizing beam wander in the focal plane of the receiver is an important and relatively low cost step in maximizing link reliability.

5.2 Turbulence-Induced Beam Motion

5.2.1 Beam Wander

After a beam propagates through a length equal to a few transmitter diameters of turbulent atmosphere, the beam begins to wander randomly in the plane transverse to the propagation direction [44]. Beam wander is a result of the electromagnetic wave interacting with turbulent eddies of sizes on the order of the transmit aperture diameter

[44]. Typically, the influential scale sizes are larger than the inner scale, ℓ_o. Although the beam wanders, it tends to maintain the shape it would have if the beam was propagating through free space [45]. It has been shown experimentally that the time constant of the beam wander is on the order of the ratio of the beam size to the wind velocity. Previous work has proposed that a fast tracking transmitter be used to minimize beam wander [20,45].

The motion of the centroid of the beam, r_c, is defined by [20]:

$$\left\langle r_c^2 \right\rangle^{1/2} = \sqrt{W_{LT}^2 - W_{ST}^2} \tag{5.1}$$

where W_{ST} is the short term beam width, and W_{LT} is the long term beam width, shown in Fig. 5.1. Beam wander may be observed while propagating a visible laser (such as a HeNe) at night.

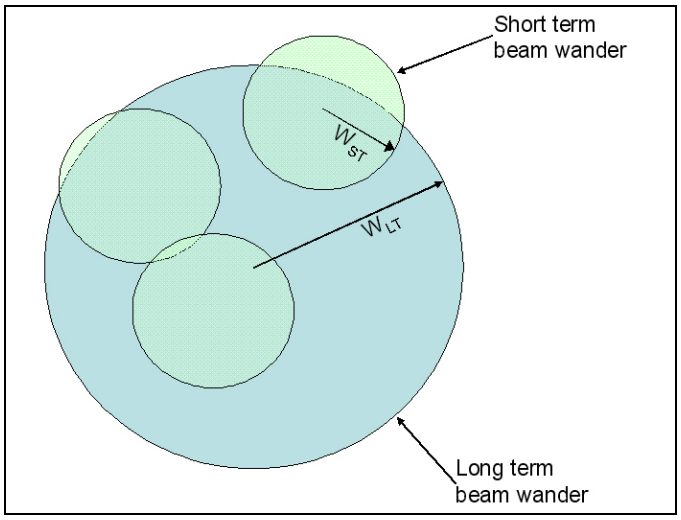

Fig. 5.1: Beam wander at the receiver plane is characterized by the short term and long term beam widths [adapted from Ref. 20].

5.2.2 Angle of Arrival and Image Dancing

Imaging dancing, also called beam wander in the focal plane, is related to turbulence-induced phase fluctuations on the propagating optical wave. The angle-of-

arrival is a result of a phase shift along the receiver lens diameter that is manifested as an optical path difference. The angle-of-arrival, α, is defined by [20]:

$$\alpha = \frac{\Delta l}{D} = \frac{\Delta S}{D} \quad \text{(in radians)} \tag{5.2}$$

where Δl is the optical path difference and ΔS is the phase shift across a receiver aperture with diameter D. Using Eq. (5.2), the RMS image displacement, Δs_{RMS}, is [20]:

$$\Delta s_{RMS} = \left\langle \alpha^2 \right\rangle^{1/2} f = \left(2.91 C_n^2 L D^{-1/3}\right)^{1/2} f \quad \text{for } D >> \ell_o \tag{5.3}$$

where f is the focal length of the optical receiver in meters. Using the specifications of link under test and typical weak turbulence conditions, $C_n^2 = 5\times10^{-15}$ m$^{-2/3}$, L = 863 m, D = 16 in or 40.6 cm, and f/10, the RMS image displacement is 16.47 μm. In testing high speed (> 1 Gbps) transmission systems, low-capacitance, small aperture photodetectors with diameters of less than 100μm are used. Any image motion will result in the loss of photons and will increase the BER.

5.3 BER in On-Off Keyed Systems

An on-off keyed (OOK) system is binary transmission protocol where 1s and 0s are represented by the transmission of a large number of photons or the lack of photons in a bit slot. The optical signal is created by either the direct modulation of a laser, or the use of an external modulator to control the emission from a continuous-wave (CW) laser source. Depending on the power and subsequent amplification of the laser source, the number of photons transmitted for a "1" may be upwards of 1,000,000,000 photons. On an atmospheric link with a fade on the order of 40 dB during a "1" bit period, and a transmitter power of 0 dBm = 1 mW, only 7800 photons may make it to the receiver.

For a p-i-n photodetector operating at 100 Mbps with a minimum receive power of -42 dBm, a minimum of 4925 photons must make it to the photodetector surface. Loosing photons due to beam wander in the focal plane is an unnecessary liability in an optical wireless link.

Measuring the BER is the best way to characterize the performance of an optical wireless communication system. The BER also accounts for the modulation format of the transmission, which in this case is the OOK format. In an OOK system, the probability of an error may be written as [20]:

$$\Pr(error) = p_0 \Pr(1 \mid 0) + p_1 \Pr(0 \mid 1) \tag{5.4}$$

where p_0 is the probability that a "0" is transmitted, p_1 is the probability that a "1" is transmitted, and $p_0 + p_1 = 1$. When a pseudorandom sequence is transmitted, an equal number of "1" and "0" bits are transmitted on average, implying that $p_0 = p_1 = 0.5$. The BER of an OOK system is derived from the theoretical probability of a bit error assuming a Gaussian noise distribution [20]:

$$\Pr(error) = \frac{1}{2} erfc\left(\frac{i_S}{2\sqrt{2}\sigma_N} \right) \tag{5.5}$$

where i_S is the signal current of one bit pulse, and σ_N is the standard deviation of the Gaussian noise distribution. The BER for an OOK system is [20,46]:

$$BER(OOK) = \frac{1}{2} \int_0^\infty p_I(S) \operatorname{erfc}\left(\frac{\langle SNR \rangle S}{2\sqrt{2}\langle i_S \rangle} \right) dS \tag{5.6}$$

where SNR is the signal-to-noise ratio of the transmission, and $p_I(S)$ is the Nakagami gamma-gamma distribution with variables representing the contribution of small-scale, γ, and large-scale, ψ, components to the irradiance of the transmission, $I = \gamma \psi$ [20,47]:

$$p_I(S) = \frac{2(\psi\gamma)^{(\psi+\gamma/2)}}{\Gamma(\psi)\Gamma(\gamma)\langle i_S \rangle}\left(\frac{S}{\langle i_S \rangle}\right)^{\left(\psi+\gamma/2\right)-1} K_{\psi-\gamma}\left(2\sqrt{\frac{\psi\gamma S}{i_S}}\right) \tag{5.7}$$

where $K_{\psi\text{-}\gamma}()$ is the modified Bessel function of the second kind. The gamma-gamma distribution is the representative probability distribution function for a range of physical phenomena, including the propagation of radio waves in the troposphere or ionosphere [20]. The components of the irradiance in the presence of atmospheric turbulence may be defined by [20,47]:

$$\begin{aligned}
\gamma &= \left(\exp\left[\frac{0.51\sigma_{R,sph}^2\left(1+0.69\sigma_{R,sph}^{12/5}\right)^{-5/6}}{1+0.90d^2+0.62d^2\sigma_{R,sph}^{12/5}}\right]-1\right)^{-1} \\
\psi &= \left(\exp\left[\frac{0.49\sigma_{R,sph}^2}{\left(1+0.18d^2+0.56\sigma_{R,sph}^{12/5}\right)^{7/6}}\right]-1\right)^{-1} \\
d &= \sqrt{\frac{kD^2}{4L}} \\
\sigma_{R,sph}^2 &= 0.4065\sigma_R^2
\end{aligned} \tag{5.8}$$

By defining a new random variable $x = S/\langle i_S \rangle$, and its derivative $dS = \langle i_S \rangle dx$, Eq. (5.6) can be transformed into the BER of an OOK system in the presence of atmospheric turbulence [47]:

$$\begin{aligned}
BER = &\frac{(\psi\gamma)^{(\psi+\gamma)/2}}{\Gamma(\psi)\Gamma(\gamma)} \\
&\times\int_0^\infty \operatorname{erfc}\left(\frac{\langle SNR\rangle x}{2\sqrt{2}}\right)(x)^{\left(\psi+\gamma/2\right)-1} K_{\psi-\gamma}\left(2\sqrt{x\psi\gamma}\right)dx
\end{aligned} \tag{5.9}$$

Eq. (5.9) is plotted in Fig. 5.2 to demonstrate the relationship between the BER and SNR for different values of irradiance variance. The three values of irradiance fluctuation were chosen to represent weak $\sigma_R^2 = 0.3$, intermediate $\sigma_R^2 = 0.6$, and non-

saturated strong turbulence $\sigma_R^2 = 2.0$. Three more curves in Fig. 5.2 are plotted to show the BER improvement for a 4 inch aperture along a 1.726 km link. For a BER of 10^{-9}, there is a between a 4 dB and 15 dB improvement with aperture averaging across each level of irradiance fluctuations.

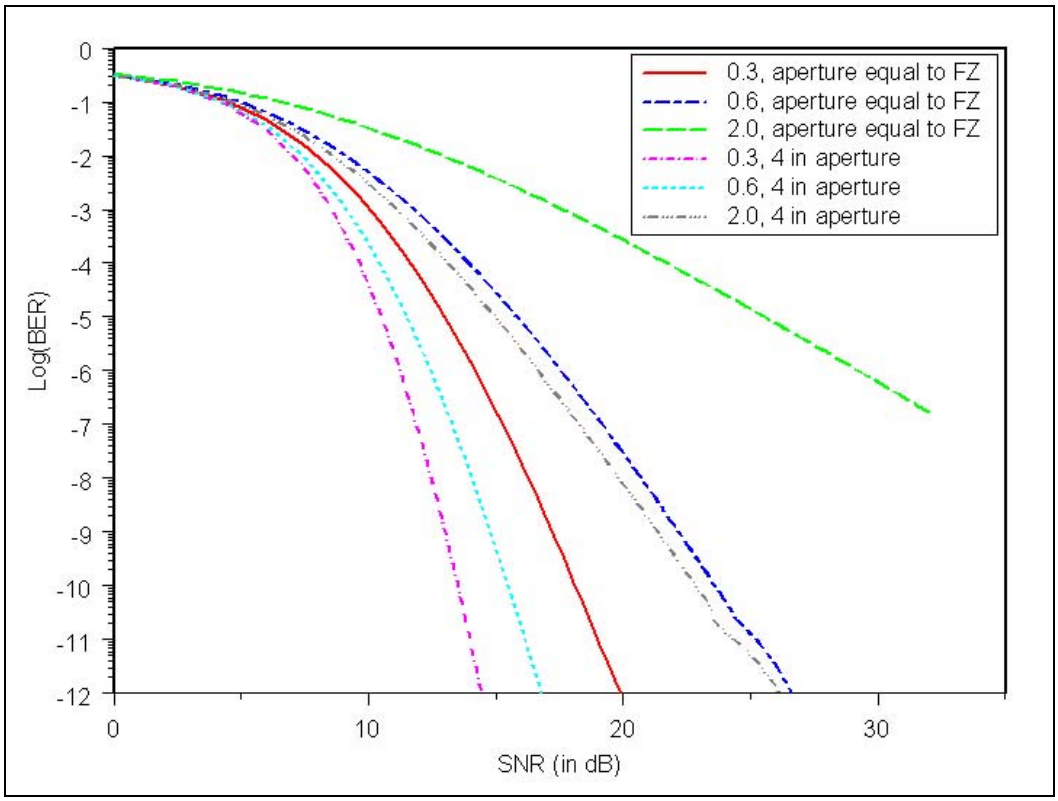

Fig. 5.2: The BER of a communications link with a gamma-gamma probability distribution function (PDF) as a function of signal-to-noise ratio. The Rytov variances plotted are 0.3, 0.6, and 2.0. When $\sqrt{kD^2/4L} = 1$, there is no aperture averaging present because the aperture radius is equal to the Fresnel zone size (FZ). Three more curves are plotted for an aperture averaged case using a 4 inch diameter aperture. The irradiance variances used in the calculation are the same in both cases.

5.4 Nonimaging Optics

To address the problem of beam wander in the focal plane, presented in Sec. 5.2, we have chosen to integrate a nonimaging optical element into the optical receiver of an optical wireless link.

5.4.1 Theory of the Compound Parabolic Concentrator

Roland Winston and W.T. Welford published the first book on nonimaging optics in 1978 [48]. Initially, nonimaging optical elements were investigated for application to the concentration of solar energy. In 1976, the design of the dielectric-filled Compound Parabolic Concentrator (CPC) for energy concentration was first published [49]. The CPC is an extension of the basic cone concentrator. The cone concentrator was limited in its performance, because some rays would be reflected back through the entrance aperture of the cone. This behavior is indicated by the double arrows in Fig. 5.3.

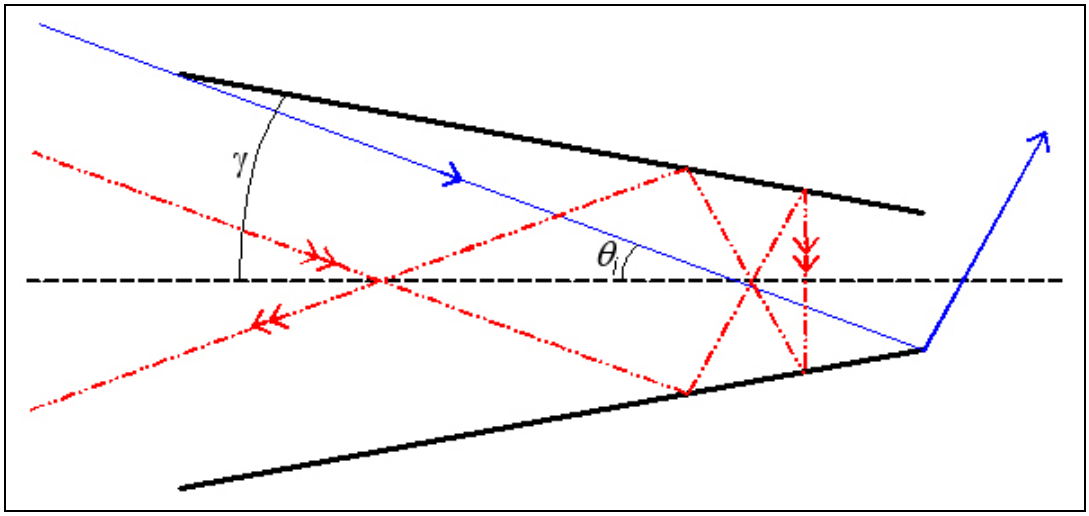

Fig. 5.3: The cone concentrator with cone angle γ and maximum entrance angle θ_i. (adapted from Ref. 48). The cone is hollow with reflective (metallic) edges.

The CPC uses surfaces traced out by an off-axis parabola to improve the concentration ratio over that of the cone concentrator. Figure 5.4 shows a diagram of the CPC. As in the case of the cone concentrator, θ_i is the maximum entrance angle of the CPC. This angle is related to the entrance and exit apertures by:

$$\sin(\theta_i) = \frac{a_{out}}{a_{in}} \tag{5.10}$$

where a_{out} is the radius of the exit (smaller) aperture, and a_{in} is the radius of the entrance (larger) aperture. The parabola has a focal length of:

$$f = a_{out}(1 + \sin(\theta_i)) \tag{5.11}$$

The design equations of the CPC in Cartesian coordinates are easily determined from Fig. 5.4:

$$\begin{aligned} y &= r\sin(\phi - \theta_i) - a_{out} = \frac{2f\sin(\phi - \theta_i)}{1 - \cos(\phi)} - a_{out} \\ z &= r\cos(\phi - \theta_i) = \frac{2f\cos(\phi - \theta_i)}{1 - \cos(\phi)} \end{aligned} \tag{5.12}$$

where the parametric angle ϕ is the angle between the axis of the parabola and the vector *r*. The parametric angle has minimum and maximum angles of $\phi_{\min} = 2\theta_i$ and $\phi_{\max} = \frac{\pi}{2} + \theta_i$. The length, *L*, of the concentrator is found by calculating *z* for $\phi = \phi_{\min}$:

$$\begin{aligned} L = \frac{2f\cos(\theta_i)}{1 - \cos(2\theta_i)} &= \frac{a_{out}(1 + \sin(\theta_i))\cos(\theta_i)}{\sin^2(\theta_i)} \\ &= (a_{in} + a_{out})\cot(\theta_i) \end{aligned} \tag{5.13}$$

The theoretical maximum concentration ratio for a 3-dimensional CPC is:

$$C_{\max} = \left(\frac{a_{in}}{a_{out}}\right)^2 = \sin^{-2}(\theta_i) \tag{5.14}$$

In fact, the maximum concentration ratio will depend on the reflectance of the concentrator surface.

CPCs are especially useful for integration into FSO communications receivers; they are easily designed, highly efficient, add minimal size and weight to the system, and are self baffling. The self baffling nature of the CPC limits the amount of stray light incident on the photodiode.

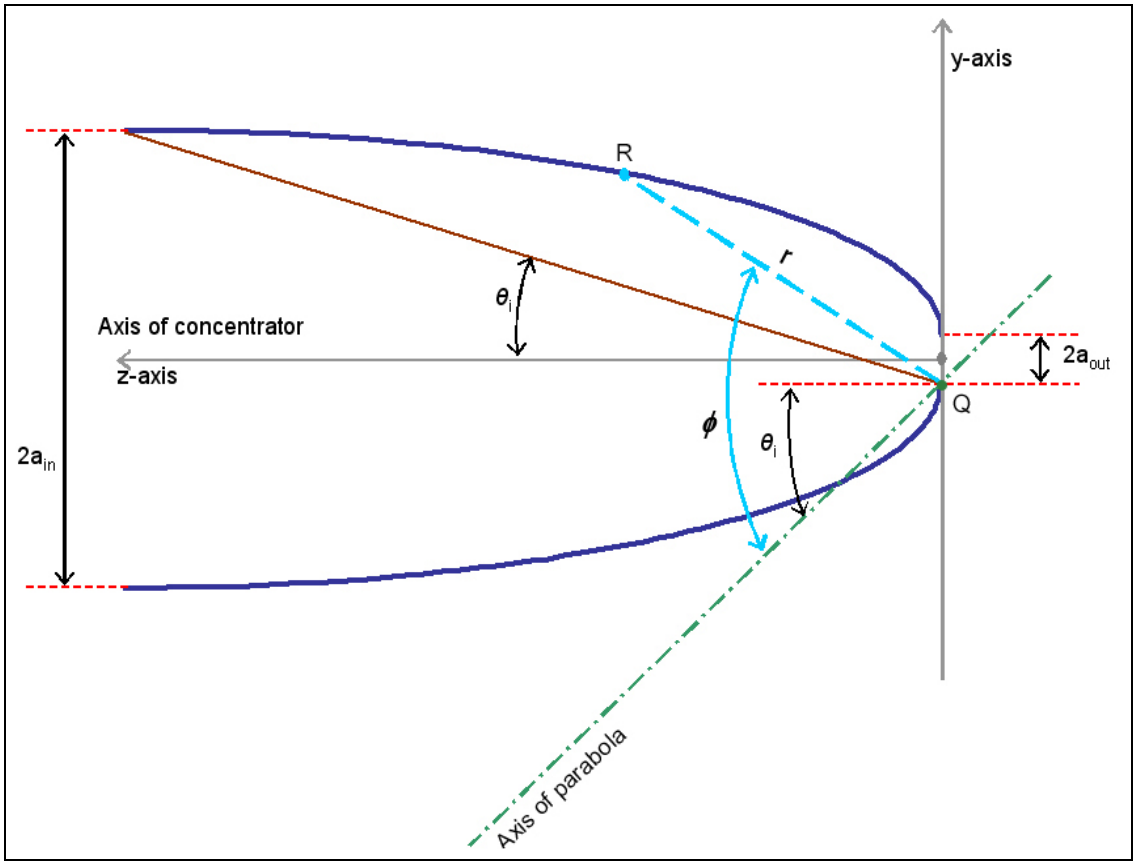

Fig. 5.4: The design of the CPC surface. The axis of the parabola and the CPC axis are different. The surface of the CPC is traced out by moving the vector *r* through the parametric angle ϕ.

5.4.2 The Dielectric-Filled CPC

Dielectric-filled CPCs take advantage of the principle of total internal reflection to maximize the concentration ratio. Since total internal reflection is nearly 100% efficient, the theoretical maximum concentration ratio becomes [48]:

$$C_{\max,dielectric} = \left(\frac{a_{in}}{a_{out}}\right)^2 = \frac{n^2}{\sin^2(\theta_e)} \tag{5.15}$$

where n is the refractive index of the dielectric material, and θ_e is the maximum angle of incidence of an entrance ray on the dielectric surface. Figure 5.5 is a plot of θ_e and the internal maximum transmission angle, θ_n. The angles θ_e and θ_n are related to n by:

$$\begin{aligned} \sin\theta_e &\le n - (2/n) \\ \sin\theta_n &\le 1 - (2/n^2) \end{aligned} \tag{5.16}$$

If $n > 2$, the angle θ_e becomes imaginary. Since the CPC cannot accept an angle larger than 90°, the maximum angle that is refracted into the dielectric is given by Snell's Law as $\sin^{-1}(1/n)$.

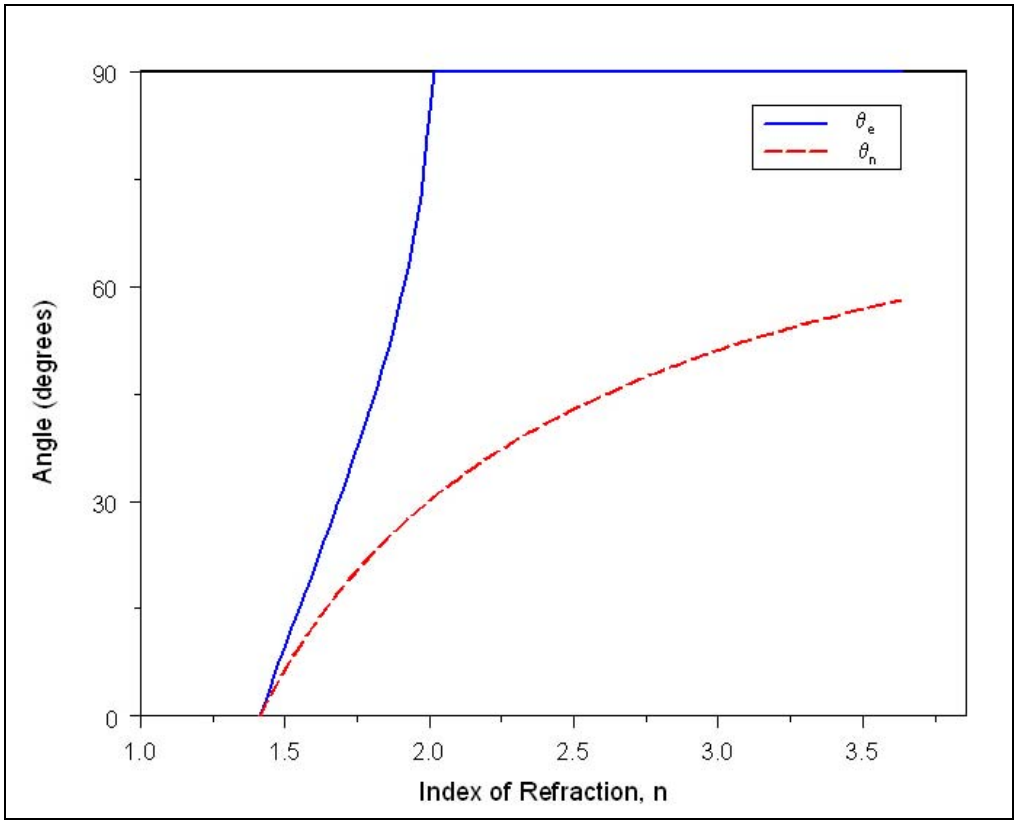

Fig. 5.5: Plot of the maximum entrance angle in air, θ_e, and the maximum internal ray angle, θ_n for a range of refractive indices.

The parametric equations for the dielectric CPC are the same as those used to describe the hollow CPC, given by Eq. (5.11) through (5.13), with θ_i replaced by the maximum internal transmission angle of the CPC.

5.4.3 The CPC-Photodetector Combination

The coupling of a CPC to a light detection device is logical method of increasing the probability that an optical signal is accurately detected. CPCs must obey the brightness principle, which states that an image cannot be brighter than the incident object [48,50,51]. When considering a CPC, the brightness theorem dictates that radiation incident on the CPC over an angle of incidence θ_i will exit the CPC maintaining the same flux per unit area; therefore, the radiation will exit the CPC over a range of angles larger than θ_i.

Using the brightness principle, a relation is found between the entrance aperture of the CPC and the photodetector area required to achieve maximum efficiency [50,51]:

$$A_{PD} = A_i \frac{\sin^2(\theta_i)}{n^2} \tag{5.17}$$

where A_{PD} is the area of a photodetector and A_i is the area of the entrance aperture of the CPC. In order to minimize the detection noise and maximize the bit rate of the system, the smallest photodetector allowed by Eq. (5.17) should be used. The maximum collection efficiency expected by Eq. (5.17) will be less than 100%, since Fresnel losses may exist at the entrance and exit surfaces of the CPC.

Alternative designs of nonimaging concentrators have been proposed, including the θ_i/θ_o concentrator [48], and RX and RXI dielectric concentrators [50,51]. The

former design restricts the exit angle by using a cone section at the exit aperture. The latter designs enhance the uniformity of the output irradiance distribution.

5.5 1.7 km CPC Link Experiment

The hypothesis of a BER improvement when using a CPC in the optical receiver of an optical wireless link was tested on a 1.7 km range at the University of Maryland, College Park.

5.5.1 Experimental Setup and Test Range

The test range used for the CPC link experiment is the same range that was used for aperture averaging experiments. The addition of a hollow, corner-cube retroreflector (CCR) allowed the link range to be doubled to 1.726 km. A schematic of the link experiment is shown in Fig. 5.6. The bit error ratio tester (BERT) generates a pseudorandom binary sequence (2^7-1), which modulates the laser diode. The output of the fiber-coupled laser diode is transmitted to the erbium doped fiber amplifier (EDFA), which amplifies the signal to approximately 158 mW. After the signal exits the optical fiber, the optical beam is transmitted by a beam expansion system to the CCR downrange. The beam expander contains a 10 x magnifying lens and a 2.25 in. biconvex lens. The 5 in. corner-cube retroreflector is gold-plated for maximum infrared reflectance. Since the retroreflector has a narrow divergence angle of 1 mrad, the transmitting lens system must be placed in front of the center of the 16 in. Meade Schmidt-Cassegrain telescope. Almost fortunately, part of the primary aperture on the telescope is obstructed by the secondary mirror, so the amount of obstruction due to the transmitter lens system is minimized.

After a portion of the beam is reflected by the CCR, the reflected wave expands and is incident on the 16 in. telescope. The Meade is an *f*/10 telescope, although the focus is adjustable. A ZnSe dielectric-filled CPC with a 1 cm entrance aperture is placed in front of the focal plane of the telescope to maximize collection efficiency. Details of the ZnSe CPC are discussed in the following section. The exit aperture (1 mm diameter) of the CPC is butt-coupled to a New Focus DC - 125 Mhz InGaAs photodiode (PD), Model 1611. The photodiode signal is amplified through two RF amplifiers and subsequently read by the BERT receiver. The BERT is an Anritsu ME522, which can transmit data at rates from 50 Mbps to 700 Mbps. An external multiplexer/demultiplexer will increase the limit to 1.4 Gbps. The BERT measurement period is variable from 1 second to hours.

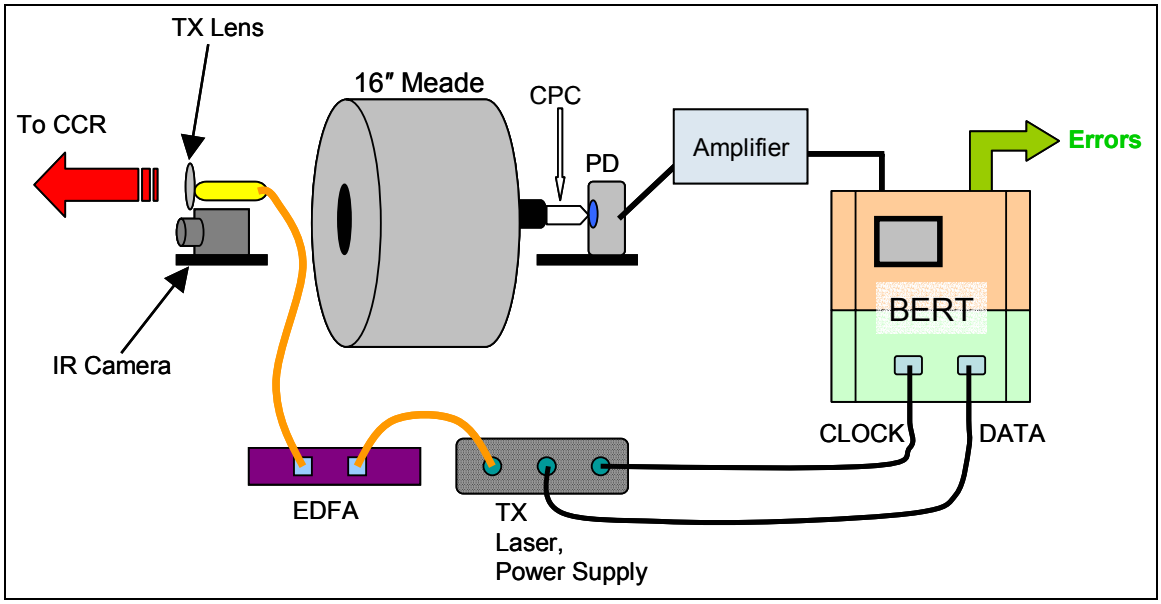

Fig. 5.6: Setup of the CPC link experiment. Black lines are electrical connections; orange lines are fiber optic connections. The IR camera is used for alignment purposes only, and is lowered below the field of view of the 16 in. Meade telescope when not in use.

5.5.2 ZnSe CPC

The CPC used in this experiment was made of ZnSe, due to its high transmission at 1.55 μm. The refractive index of ZnSe at 1.55 μm is 2.48. The CPC is approximately 2.25 cm long, with an entrance diameter of 1 cm and an exit diameter of 1 mm. A profile of the CPC is shown in Fig. 5.7, with a canned photodiode centered at the exit aperture of the CPC. The CPC has a maximum entrance angle of ~5°. At normal incidence, 18% of the light is reflected at each aperture.

For the 1.7 km experiment, the photodetector integrated into the package was removed. The New Focus InGaAs photodetector was used in its place.

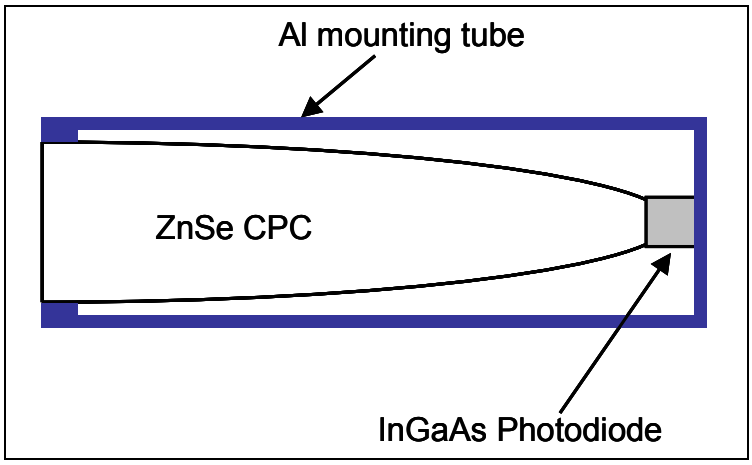

Fig. 5.7: Profile of the mounted ZnSe CPC directly coupled to an InGaAs PD.

5.5.3 Link Budget

The link budget is a design method to ensure that enough power will reach the optical receiver given that there will be some losses on the optical link. It may be written in the form [52]:

$$P_{TX} = P_{RX} + C_L + M_s \tag{5.18}$$

where P_{TX} is the average transmitter power, P_{RX} is the receiver sensitivity in dBm, C_L represents the channel losses, and M_s is the system margin, which represents the maximum additional loss the system can handle. The link budget is normally written with the optical power in dBm, where $1\,\text{dBm} = 10\log_{10}(P/1\,\text{mW})$, and the electrical power in dB. The link budget of the 1.7 km link, without the CPC, is articulated in Table 5.1.

The system margin is given by:

$$\begin{aligned} M_s &= P_{TX} - P_{RX} - C_L \\ &= 22\text{dBm} + 44.3\text{dBm} - 38.5\text{dB} \\ &= 28.2\text{dB} \end{aligned} \tag{5.19}$$

Although this system margin is sufficient to maintain a BER of 10^{-9} in a digital communications system, where an electronic noise margin of 21 dB is required [20, 46,53], it does not account for fading on the optical wireless link. A fade is a sudden drop in the signal strength that may result in the erroneous detection of a bit. Fading on optical wireless links is induced by the motion of turbulent eddies in the atmosphere. Fades of 10dB are common, although fades of over 40 dB have been reported [54]. Fig. 5.2 shows that for a BER of 10^{-9} in weak turbulence ($\sigma_R^2 = 0.3$), a SNR of 17 dB is needed. This is a clear example of how receivers integrated with nonimaging concentrators should improve the link margin without placing any additional size, weight, or power burdens on the system.

Link component	Component specifications	Power (in dB or dBm)
1.55 μm laser: Force, Inc. model 2666A	Max. launch power 0.15 mW, extinction ratio 10:1	-8 dBm
Optigain EDFA model 2000	Max. gain 30 dB Max. output 23 dBm	30 dB
P_{TX}	Transmitter power = 158 mW	22 dB
Fiber splice	2 splices @ -0.15 dB	-0.3 dB
Fiber connectors	2 connectors @ -0.5 dB	-1 dB
Viracon thermal pane window in Chesapeake Bldg.	Average 25% transmission for infrared wavelengths	-6 dB
Atmospheric transmission	Assume an attenuation of 0.2 dB/km for clear air [55]	-0.75 dB
Retroreflector	Loss due to mismatch of beam width and CCR diameter (129mm)	-11.7 dB
	Surface reflectivity	-0.175 dB
Atmospheric transmission		-0.75 dB
Window loss		-6 dB
Meade LX 200 EMC	Loss due to mismatch of beam width and 16 in. aperture	-6.54 dB
	Loss due to secondary mirror obstruction of Schmidt-Cassegrain design telescope	-0.446 dB
	Telescope transmission at 1.55μm with EMC coatings	-1.25 dB
Coupling loss	Coupling of focal spot to photodetector	-0.5 dB
Total channel loss, C_L		-38.5 dB
P_{RX} New Focus 1611 InGaAs photodetector	Receiver sensitivity NEP = 2.5pW/(Hz)$^{1/2}$	-44.3 dBm

Table 5.1: Link budget analysis for the 1.7 km link, neglecting atmospheric turbulence.

5.5.4 C_n^2 Measurements

The strength of turbulence, C_n^2, is measured over the same time interval as the BER. Measurements over 1 minute intervals gave the most reliable results. The C_n^2

was measured over the scintillometer channel used in the aperture averaging experiment.

5.5.5 Experimental Results and Analysis

A 100 Mbps pseudorandom binary sequence with a pattern length of 2^7-1 bits was transmitted downrange and reflected by the corner cube retroreflector. Test runs were done with and without a ZnSe CPC placed directly in front of the New Focus 1611 InGaAs photodetector. The exit aperture of the CPC was in direct contact with the photodetector window in order to achieve maximum optical coupling. This coupling is especially important since there is a large area mismatch between the CPC exit aperture (1 mm diameter) and PD (0.3 mm diameter). The coupling of the CPC and photodetector is very angle sensitive, and the CPC was placed on a 6 degree-of-freedom stage to attempt to maximize light output. The PD was mounted on an xyz stage. The actual PD surface is set back 0.5 mm from the lens case. A significant loss of coupling was observed when there was more than 2 mm of air space between the PD and the CPC.

Data was taken over two consecutive days in weak turbulence conditions ($\sigma_I^2 < 0.3$). BER for 100 Mbps PRBS transmission with and without the CPC is plotted against the measured C_n^2 in Fig. 5.8, with error bars representing the fluctuation of C_n^2 over a 1 min. acquisition period. Fig. 5.9 plots a first order linear fit along with the mean data. The curve fit equation is also shown in the plot.

From Figs. 5.8 and 5.9, the measured BERs were found to be on the order of 10^{-3} to 10^{-4}. The range of BER measurements indicates that the beam may not have been as collimated as was thought. Since the system operates at 1.55 μm, the width of

the beam when it reaches the 5 inch retroreflector is extremely difficult to measure. Though the BERs on the FSO link are high, the important result is the relative enhancement of the BER when the optical communications receiver includes a CPC.

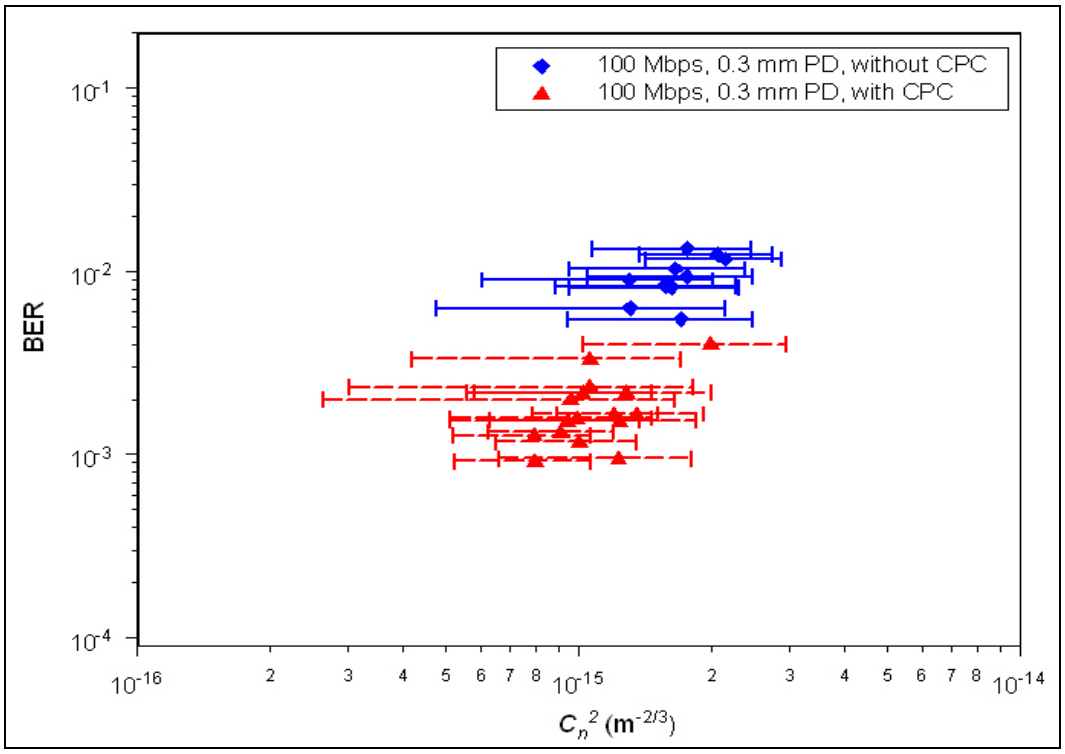

Fig. 5.8: BER plotted as a function of C_n^2 for the 1.7 km link with and without the CPC integrated into the optical receiver. The error bars in C_n^2 represent its fluctuation over the 1 min averaging interval.

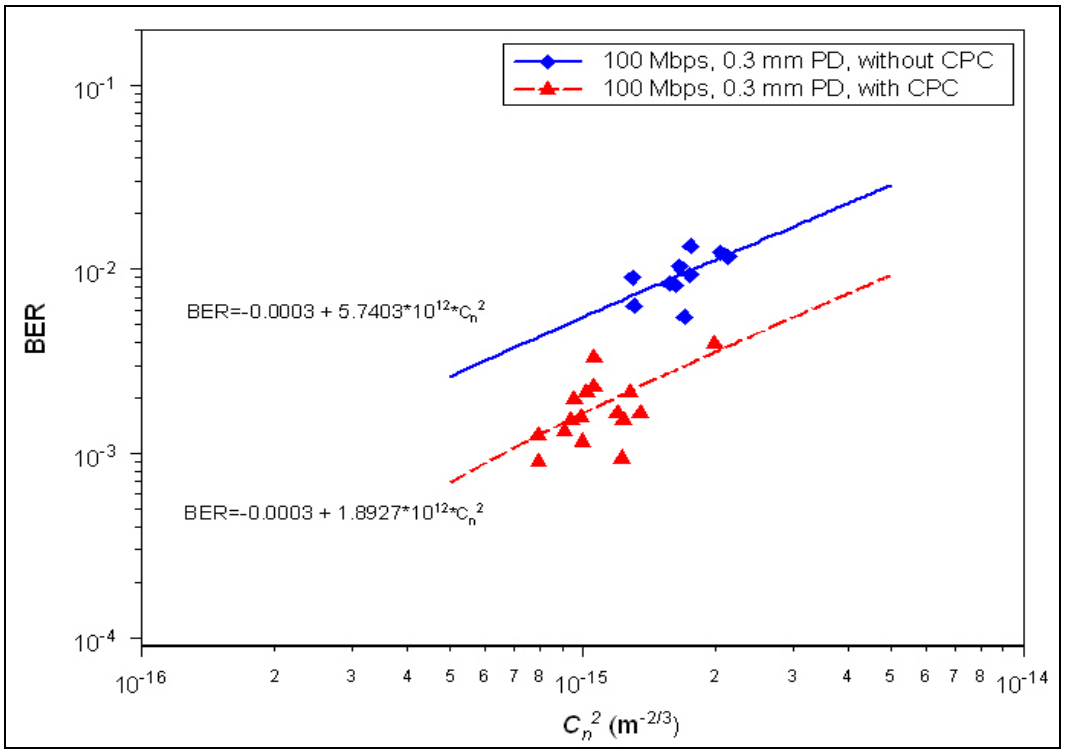

Fig. 5.9: Same data as in Fig. 5.8, plotted along with a first order linear fit to the mean data.

There is approximately a factor of 5 improvement in the BER when using the CPC in the optical receiver. This enhancement is particularly encouraging, considering that only about 11% of the light that exits the CPC is collected by the PD, due to the area mismatch. A CPC-PD combination where the PD area is either the same or slightly larger than the exit aperture of the CPC should yield a better BER enhancement. Also, the CPC and PD were mounted on a tripod, which caused the signal to be sensitive to vibrations of the floor. Since the Meade telescope is in its own, very large, heavy tripod, it does not feel the vibrations. A telescope with the CPC and PD using the same optomechanical mount would also improve the performance by making the system immune to vibrations.

Fig. 5.10 is an oscilloscope trace of the amplified received data, before and after passing the signal through a limiting amplifier. The second trace in Fig. 5.10 is actually the inverse of the data, which is connected to the oscilloscope so that each of the limiting amplifier terminals are properly terminated. Nonetheless, it shows how the limiting amplifier attempts to clean up the turbulence induced fluctuations of the data, but still leaves residual noise on the data that it cannot clean up. In using the BERT, the user must be careful that the terminals of the BERT are not overloaded; otherwise there could be significant damage to the system. The turbulence-induced optical fluctuations of the receive signal affect the quality of the electrical signal output of the RF amplifiers. The amplified signal even showed some baseline wander due to the fluctuations in the intensity of the received signal. The amplified signal was attenuated to between 30 mV_{p-p} and 500 mV_{p-p} so that any sudden spikes in intensity would not overload the limiting amplifier. The limiting amplifier then outputs a 1.2 V_{p-p} signal to the BERT.

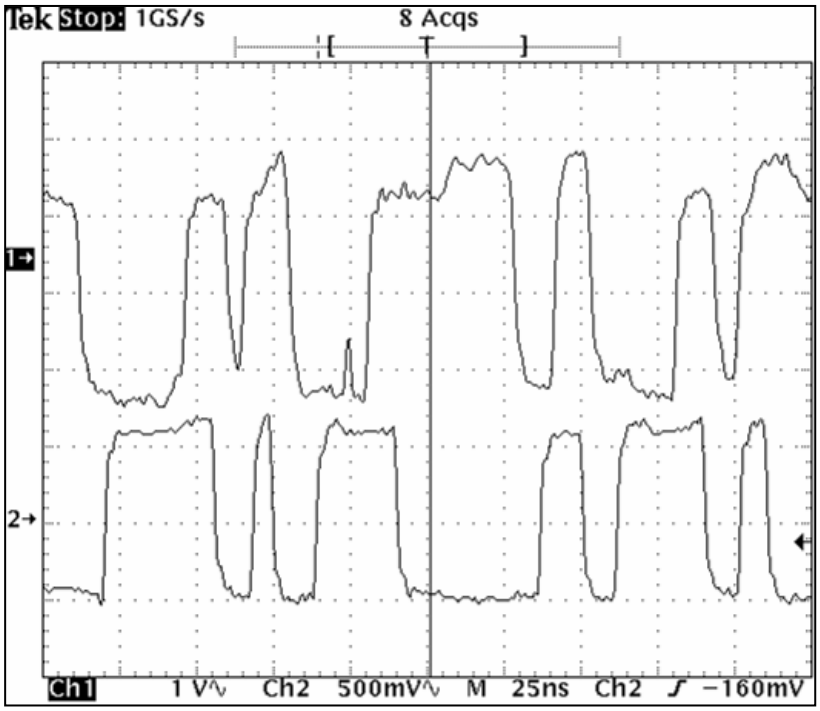

Fig. 5.10: Trace 1 shows the data stream after passing through two 20 dB RF amplifiers. Trace 2 shows the inverted data after passing through a limiting amplifier. The signal after the limiting amplifier is much cleaner; however there is still enough turbulence-induced noise to degrade the BER.

5.6 NRL Test Range Experiment over the Chesapeake Bay

An experiment to demonstrate the BER enhancement due to the use of a CPC-PD combination in an optical receiver was conducted at the Naval Research Laboratory's Chesapeake Bay Detachment, in Maryland (NRL-CBD).

5.6.1 Experimental Setup and Test Range

The Naval Research Laboratory has a facility located on the Chesapeake Bay in Maryland that they have set up for use as a laser communications test site. They have previously used the facility to test their modulating retroreflector (MRR) array technology [56,57]. To test high speed laser communications, a solid retroreflector array is located on a tower at Tilghman, MD, and can be interchanged with an MRR

array. The Tilghman site is approximately 16.2 km across the bay from NRL-CBD. Fig. 5.11 is a diagram of the test range.

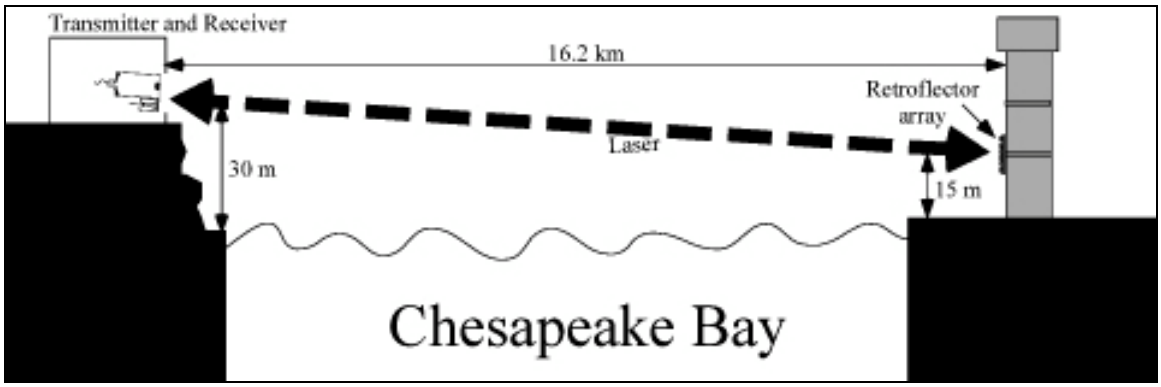

Fig. 5.11: The NRL-CBD laser communication test range [56].

The retroreflector array at the Tilghman tower is composed of 12 solid retroreflectors, aligned three wide by four tall, spaced on 5 inch centers. Each retroreflector is 2 inches in diameter. The optical transmitter uses a fiber-coupled diode laser at 1.55 μm that is subsequently amplified to 2 W. The signal exiting the fiber is expanded and collimated, and sent downrange to the retroreflector array. Fig. 5.12 is a diagram of the optical transmitter. A BERT pattern generator (Agilent model 86130A) modulates the fiber-coupled diode with a 2^7-1 PRBS pattern.

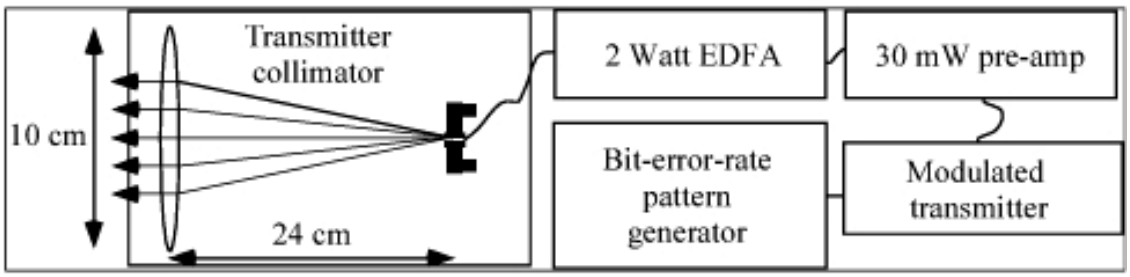

Fig. 5.12: Optical transmitter at NRL-CBD. The collimated optical output is approximately 2 W [56].

When the retroreflected signal returns, it is collected by a 16 in. Meade LX200 Schmidt-Cassegrain telescope. This is the same telescope used in the 1.7 km link at the University of Maryland. It is estimated that 1.84 mW of the 2 W launch power is

collected by the 16 in. receiver telescope [56]. Since the signal strength is very low after traversing a 32 km roundtrip, the signal is amplified with a Femto variable gain voltage amplifier that can amplify a signal by up to 60 dB (model DHPVA-100). The signal is then detected by the BERT receiver. A description of the optical receiver is shown in Fig. 5.13.

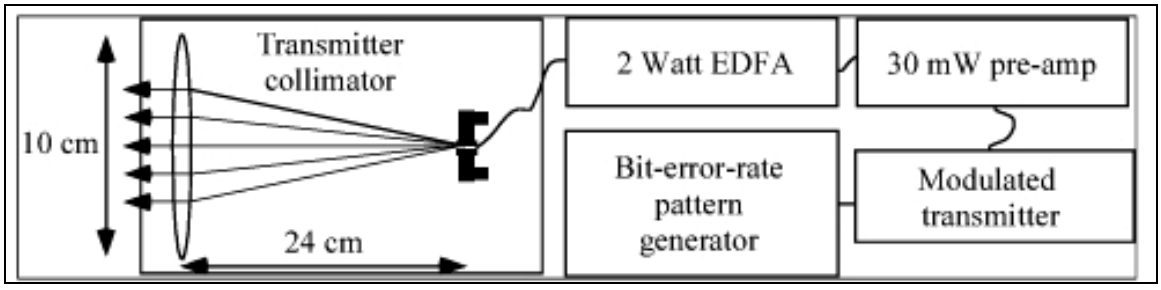

Fig. 5.13: The optical receiver at NRL-CBD [56].

5.6.2 CPC-PD Combination System

The integrated CPC-photodiode optical receiver, shown in Fig. 5.7, is used as the detection system in the NRL-CBD experiment. The detector integrated into the package is a Telecom Devices 35PD500-TO InGaAs photodiode with a 0.5 mm diameter. The distance between the TO-46 package window and the photodiode surface is 0.38 mm. At 1.5 μm, the photodiode has a responsivity of 1.0 A/W. The back end of the aluminum mounting tube has bond pads and short leads that connect the photodiode signal to a Maxim 3266 low noise transimpedance preamplifier chip.

The input sensitivity of the preamplifier for a BER of 10^{-9} is:

$$\begin{aligned} Sensitivity &= 10\log\left(\frac{OSNR \times I_N (r_{ex}+1)}{2\Re(r_{ex}-1)} \times 1000\right) \\ &= 10\log\left(\frac{11.89 \times 200\text{nA} \times (10+1)}{2 \times 1.0\text{A/W}(10-1)} \times 1000\right) \\ &= -28.38\text{dBm} \end{aligned} \qquad (19)$$

where *OSNR* is the optical SNR required to achieve a BER of 10^{-9}, I_N is the input-referred RMS noise current of the Maxim 3266, r_{ex} is the extinction ratio of the laser transmitter (defined here by the ratio P_1/P_0) [58,59], and $\Re$ is the responsivity of the photodiode in A/W. The optical power in a "1" bit and "0" bit may also be calculated. When using a PRBS transmission pattern, the optical power in a "1" bit is approximated by twice the average power [43]. Given a 10:1 extinction ratio and assuming a 2W (33 dBm) average power, the optical power in a "0" bit is 10 dB lower than that of a "1" bit:

$$\begin{aligned} P_1 &= 4\text{W} \\ \text{P}_0 &= 0.1 \times 4\text{W} = 400\text{mW} \end{aligned} \tag{20}$$

where P_0 is the power in a "0" bit, and P_1 is the power in a "1" bit.

5.6.3 Experimental Results and Analysis

BER measurements were taken over the 32.4 km test range at NRL-CBD. The CPC-PD receiver was used in place of a 62.5 μm optical fiber coupled receiver. Measurements were made at standard telecommunication data transmission rates of OC-1 (51.84 Mbps), OC-2 (103.68 Mbps), and OC-3 (155.52 Mbps). Data was taken over a 4 hour window with an atmospheric temperature range of 2.4° to 3.5°, a water temperature range of 5.8° to 5.9°, and an average windspeed ranging from 1.0 m/s to 2.6 m/s. These temperature and windspeed measurements were taken from a NOAA buoy in proximity to the NRL-CBD test range at Thomas Point, MD. The experiment was attempted twice prior to the successful test, but had to be cancelled because of the amount of turbulence present on the link. The turbulence made it impossible to align the test link using LED beacons on the tower at Tilghman and a position sensitive detector located at NRL-CBD.

From Eq. (5.3), the beam wander in the focal plane is estimated at Δs_{RMS} = 339.6 μm for a $C_n^2 = 1\times10^{-13}$ $m^{-2/3}$. A high value of C_n^2 is assumed because link must be in the saturated strong turbulence range, due to the extremely long propagation length.

Data collected at OC-1 is shown in Fig. 5.14. The overall BER is plotted in 1 min intervals, along with the "0" error rate and "1" error rate. The Agilent BERT has the ability to count "0" errors and "1" errors. Typically, we expect that "0" errors are much lower than "1" errors because the power in a "0" bit should be below the threshold of the BERT. For the OC-1 test, the "0" error rate is lower than the "1" error rate, although not substantially lower.

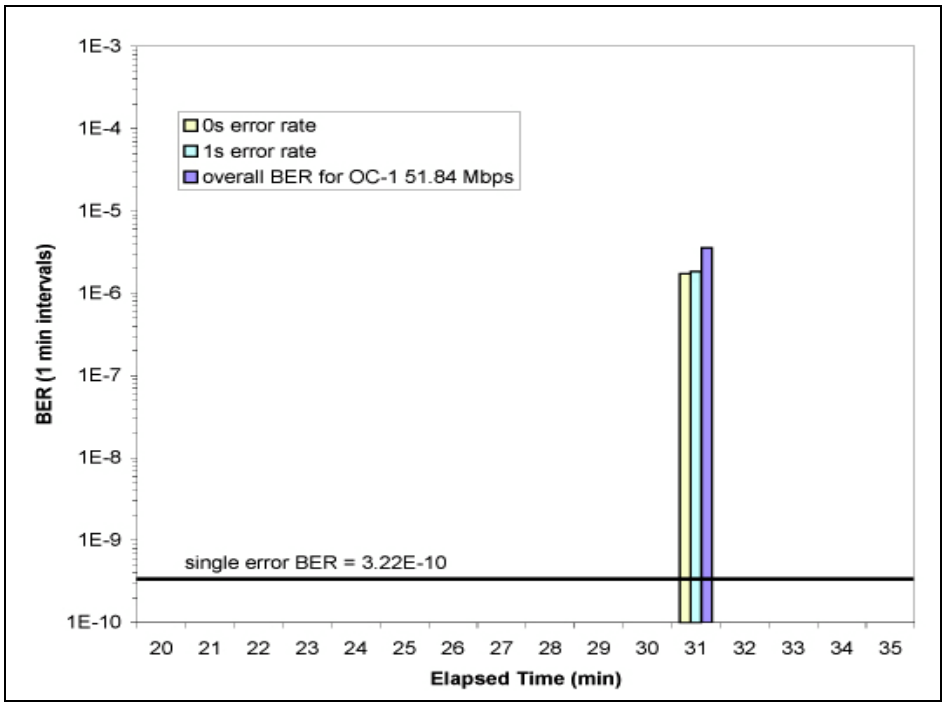

Fig. 5.14: Measurements of BER using the CPC-PD receiver when an OC-1 PRBS transmission pattern was tested during a 35 minutes test period. The BER of 1 bit in a 51.84 Mbps transmission is 3.215×10^{-10}, as indicated by the dark horizontal line. There were no errors between minutes 1 and 19. The only errors were detected in the 31st minute.

BER measurements taken at OC-2 are shown in Fig. 5.15. In the 11th minute, the "1" error rate is much higher than the "0" error rate. Fig. 5.16 shows OC-2 BER data published in an NRL paper, with a 62.5 μm optical fiber coupled receiver in place of the CPC-PD receiver. The signal is measured by an OC-12 receiver, regenerated and collected by an OC-48 receiver, and finally received by the Agilent BERT.

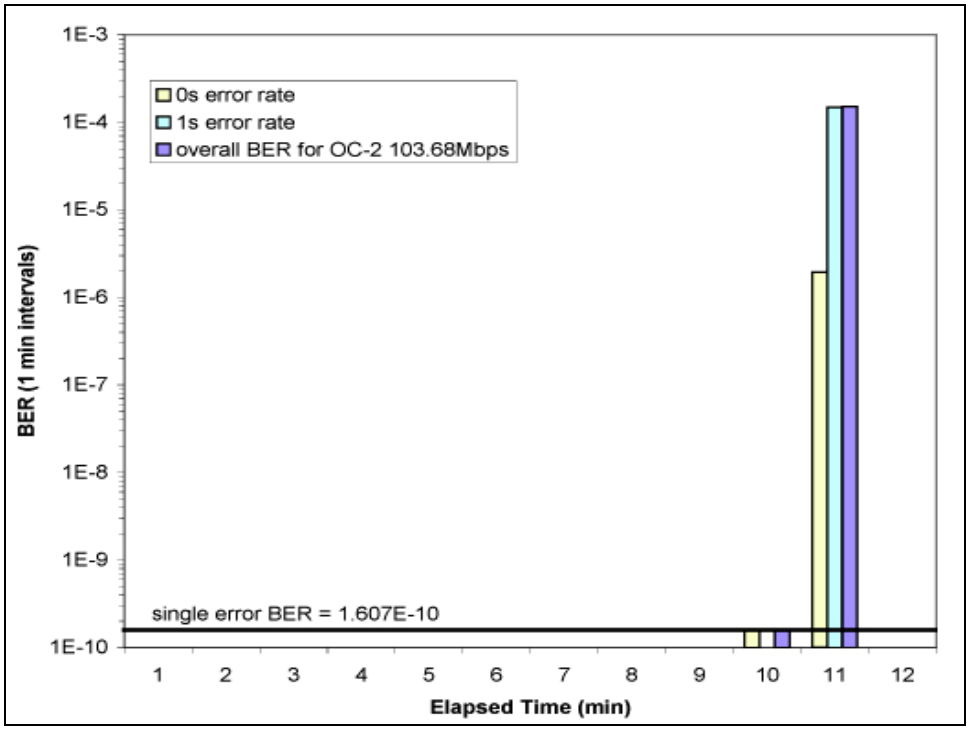

Fig. 5.15: BER at OC-2 over a 12 minute acquisition period using the CPC-PD receiver. A single bit error in a 103.68 Mbps transmission at OC-2 gives a BER of 1.607×10^{-10}.

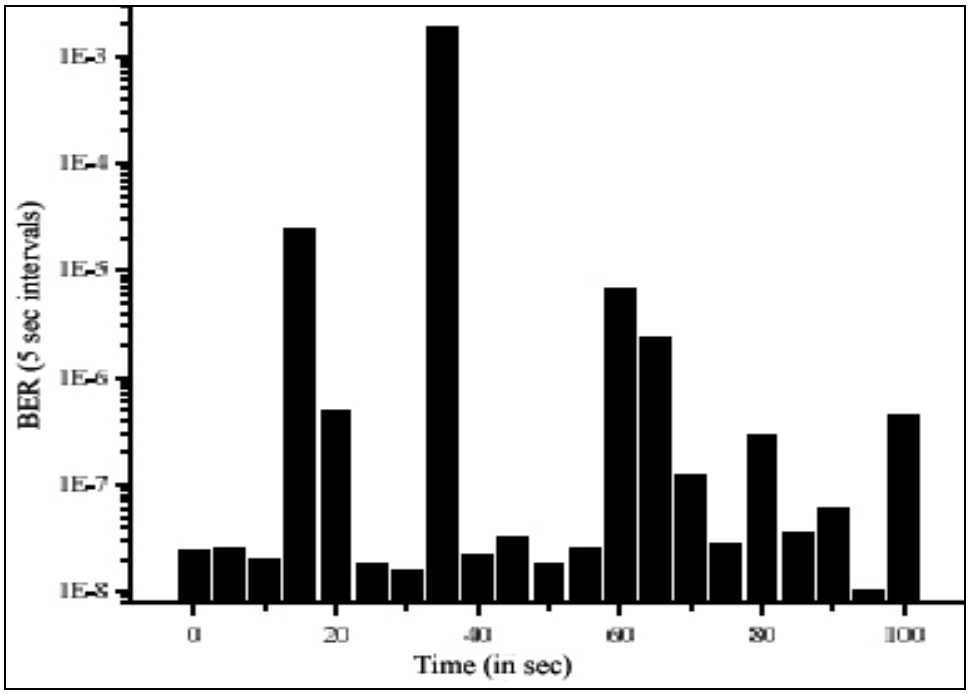

Fig. 5.16: BER at 100Mbps measured over the NRL-CBD test range with an optical fiber coupled receiver, from Ref. 46. Note that data is plotted for 5 sec intervals. The minimum BER for a 5 sec interval is 2×10^{-9}, which is beyond the range of the graph.

A comparison of the data from the CPC-PD receiver (Fig. 5.15) and the NRL-CBD optical fiber coupled receiver (Fig. 5.16) shows a significant improvement in BER when using the CPC. The long link length contributes to the amount of beam wander in the focal plane. In Fig. 5.16, there is not one acquisition interval that is error-free. The problem of beam wander in the focal plane is visibly reduced, and manifested in the BER improvement.

BER results from tests with the highest transmission rate, OC-3, are shown in Fig. 5.17. The first 4 minutes of acquisition are error free. The following 11 minutes show significant errors. This behavior is indicative of transmitter alignment problems and not problems with the CPC-PD receiver. There is no autotracking between the

transmitter and receiver on the link. There was also an evening haze rolling in during this acquisition time, which could affect alignment over such a long range.

The first 4 minutes of error free acquisition are extremely encouraging. Fig. 5.18 shows published results from the link with an optical fiber coupled receiver for data transmitted at 200 Mbps. A direct comparison with OC-3 data is not available. Fig. 5.18 shows a consistent and significant number of errors throughout the acquisition period. Compared with the new data in Fig. 5.17, it appears that the addition of a CPC into the receiver system would improve the BER. New data could not be acquired at 200 Mbps, due to the bandwidth range of the Femto variable gain amplifier. The device had a bandwidth of 100 MHz, and the receive signal intensity at 200 Mbps fell off significantly.

Overall, each of the three data rates tested showed a significant amount of error-free time. Although this CPC-PD receiver was not optimized for the link, nor was the optical coupling between the CPC exit aperture and PD surface optimized, the device performed extremely well.

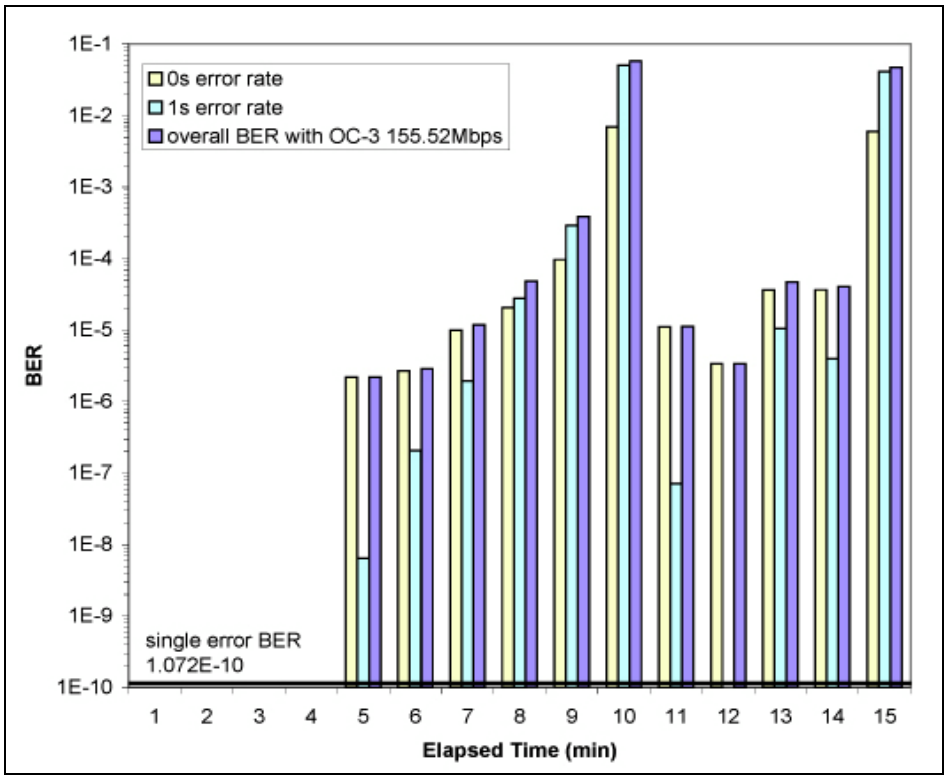

Fig. 5.17: BER at OC-3 measured over a 15 minute period using the CPC-PD receiver. The single error BER for a 1 min acquisition period is 1.072×10^{-10}.

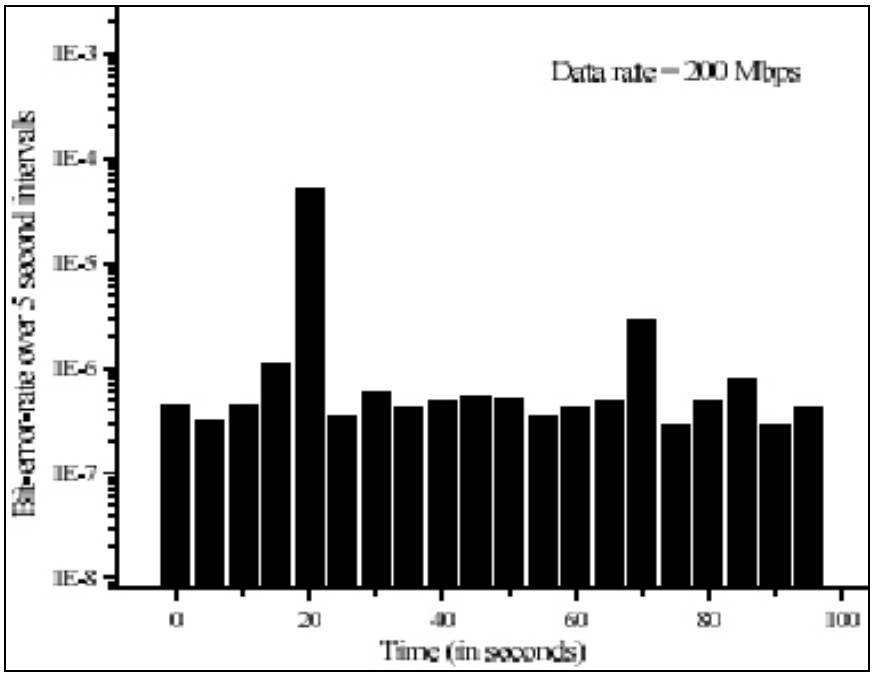

Fig. 5.18: BER at 200Mbps measured over the NRL-CBD test range with an optical fiber coupled receiver, from Ref. 46. Note that data is plotted for 5 sec intervals. The minimum BER for a 5 sec interval is 1×10^{-9}, which is beyond the range of the graph.

5.7 Conclusions

The experimental results presented in this chapter show the performance enhancement in BER due to the integration of nonimaging optical elements into a FSO optical receiver. The data shows a factor of 5 improvement in BER when a compound parabolic concentrator was integrated into the optical receiver system of a 100 Mbps link over a 1.7 km retroreflected test range at the University of Maryland, College Park. An integrated CPC-photodiode device was tested at the Naval Research Laboratory's 32.4 km Chesapeake Bay test range. The link showed only rare periods of burst errors during this experiment, as compared to significant, sustained errors without the use of the device. Both experiments validate the ability of the CPC to significantly reduce the number of data transmission errors due to beam wander in the focal plane of the receiver. Optimized CPC-photodiode combinations will improve on the results presented here.

Chapter 6

Conclusion

6.1 Summary of Contributions

This dissertation describes two techniques that will enhance the performance of free space optical communication systems, while minimizing the size, weight, and power of the system. Through experimental studies and comparison with available models and theory, on-off keyed FSO communication systems will show a significant performance improvement in data transmission when aperture averaging methods and nonimaging optical elements are incorporated into the system design. Both studies show the ability to mitigate the effects of atmospheric turbulence on the propagating coherent optical wave.

Aperture averaging techniques specifically aim to reduce the atmospheric turbulence-induced intensity fluctuations that appear on a propagating optical wavefront. Experimental studies of aperture averaging were conducted in both weak and strong fluctuation conditions over a test range at the University of Maryland, College Park. Due to the technical complexities involved in designing an aperture averaging experiment, only one set of published data to this point has been available to compare with analytical models. The experiment presented in this dissertation exceeds the scope of the previously published data. The new data presented here represents significantly improved measurements in both weak turbulence and strong turbulence conditions due to: the examination of a wider range of aperture diameters; the use of

better quality electronics, computers, and data acquisition equipment; the measurement of C_n^2 over the entire length of the aperture averaging test range; the simultaneous measurement of background light levels with aperture averaging data; and the use of an elevated test range allowed for minimal fetch influences. This is also the first report of aperture averaging data collected for non-saturated strong turbulence conditions. Since the behavior of the refractive index spectrum in the energy dissipation range is still in contention, strong turbulence theory is still questionable. This data will be useful in improving the quality of strong turbulence theory and models available for the study of aperture averaging in strong fluctuation conditions.

Compound parabolic concentrators integrated into optical wireless receivers are shown to counteract the bit error ratio degradation attributed to atmospheric turbulence-induced beam wander in the focal plane of the receiver. This dissertation is the first report of an experimental characterization of the performance enhancement due to the integration of the CPC into the receiver. Promising BER improvements by a factor of 5 resulted from the testing of 100 Mbps data in weak turbulence conditions on the 1.7 km link at the University of Maryland, College Park. Due to the small link margin and difficulty in link alignment, PRBS bit error ratio tests were not achieved at rates beyond 100 Mbps. This experiment is supplemented by BER testing using a CPC-photodiode combination receiver at the Naval Research Laboratory's Chesapeake Bay Detachment. The 32.4 km retroreflected link always experiences saturated strong turbulence conditions. By comparison with previously published NRL data, the CPC-PD receiver showed only minimal burst errors over the testing time, at optical communication standard rates of OC-1 through OC-3. The performance enhancements demonstrated in

this dissertation, along with the compact size of the device, should make the CPC a mandatory part of any OOK FSO communication receiver. By designing the CPC in such a way that its exit aperture maximizes concentration of optical energy onto the surface of a photodiode, data transmission errors due to beam wander in the focal plane could be absolutely canceled.

6.2 Future Work

This dissertation has begun to address perhaps the most significant problem plaguing the design of FSO systems: the lack of experimental data pertaining to the effects of atmospheric turbulence on the propagation of coherent optical waves. The experimental data presented here provides valuable insights into how FSO receivers may be optimized to improve the transmission of OOK systems. Although the data spans both weak and strong turbulence conditions, more data in strong turbulence conditions should be gathered to complement the data presented here.

Due to the height of the optical test range at the University of Maryland, only limited data was collected for aperture averaging in strong turbulence. The testing of smaller and larger receiver apertures on a new range that consistently experiences saturated strong turbulence conditions would also be beneficial.

Regarding the CPC experiments, an optimized CPC-PD device should allow the experimental determination of the extent of a BER performance enhancement. A new electronic preamplifier and receiver would have to be designed to test the device at data rates beyond 1 Gbps. It would certainly be interesting to characterize the maximum OOK transmission rate the CPC could handle.

Finally, the data presented here should be studied to improve the quality of the refractive index spectrums designed for strong turbulence. Although the Hill spectrum has been shown to be the most accurate in strong turbulence conditions, the fact that it needs to be solved numerically makes it difficult to use in practical situations. Approximations to the Hill spectrum, like the modified and effective atmospheric spectrums, still leave room for improvement. The new aperture averaging data presented here is valuable because it directly measured the irradiance variances in strong turbulence. In the past, spectrums have been derived from log-irradiance variance statistics, which do not address the practical measurements of the irradiance variances in strong turbulence conditions. Theoretical researchers need to address the refractive index spectrum in strong turbulence by studying experimental data collected for the strong turbulence irradiance variance.

References

[1] Strobehn, J.W. (ed.). *Topics in Applied Physics*, Vol. 25, *Laser Beam Propagation in the Atmosphere*. Springer-Verlag: New York, 1978.

[2] Lucy, R.F. and K. Lang. "Optical communications experiments at 6328 Å and 10.6 μm." *Appl. Opt*., Vol. 7, No. 10, Oct. 1968, p. 1965-70.

[3] Lipsett, M.S. et al. "Space instrumentation for laser communications." *IEEE J. Quant. Elec*., Vol. 5, No. 6, June 1969, p. 348-9.

[4] Solimeno, S. et al. "Optical communication in turbulent media." *Proceedings of the 1970 International Symposium on Information Theory*. IEEE: New York, 1970.

[5] Masud, Sam et al. "Ten Hottest Technologies." *Telecommunications Magazine*, May 2001.

[6] Li, Tiffany Jing and Murat Uysal. "Achievable Information Rate for Outdoor Free Space Optical Communication with Intensity Modulation and Direct Detection." *Proc. GLOBECOMM*, Vol. 2, 2003, p. 2654-8.

[7] Polak-Dingles, P. et al. "Performance update of a terrestrial laser-communications link with quadrature amplitude modulation." *Proc. SPIE*, Vol. 2990, *Free Space Laser Communication Technologies IX,* April 1997, p. 82-93.

[8] Ohtsuki, Tomoaki. "Performance Analysis of Atmospheric Optical PPM CDMA Systems." *J. Lightwave Technol*., Vol. 21, No. 2, February 2003, p. 406-11.

[9] Zhu, Xiaomihng and J. M. Kahn. “Performance Bounds for Coded Free-Space Optical Communications Through Atmospheric Turbulence Channels.” *IEEE Trans. Commun*., Vol. 51, No. 8, August 2003, p. 1233-9.

[10] Fried, D.L. “Aperture Averaging of Scintillation.” *J. Opt. Soc. Am*., Vol. 57, No. 2, February 1967, p. 169-75.

[11] Churnside, James H. “Aperture averaging of optical scintillations in the turbulent atmosphere.” *Appl. Opt*., Vol. 30, No. 15, 20 May 1991, p. 1982-94.

[12] Vinnichenko, N.K. et al. *Turbulence in the Free Atmosphere*. Consultants Bureau: New York, 1980.

[13] Wheelon, Albert D. *Electromagnetic Scintillation*, Vol.1, *Geometrical Optics*. Cambridge University Press: Cambridge, 2001.

[14] Andrews, David G. *An Introduction to Atmospheric Physics*. Cambridge University Press: Cambridge, 2000.

[15] Panofsky, Hans A. and John A. Dutton. *Atmospheric Turbulence: Models and Methods for Engineering Applications*. John Wiley & Sons: New York, 1984.

[16] Andrews, Larry C. and Ronald L. Philips. *Laser Beam Propagation through Random Media*. SPIE Optical Engineering Press: Bellingham, Washington, 1998.

[17] Lawrence, Robert S. and John W. Strobehn. “A Survey of Clear-Air Propagation Effects Relevant to Optical Communications.” *Proc. IEEE*, Vol. 58, No. 10, October 1970, p. 1523-44.

[18] von Karman, Theodore. “Progress in the Statistical Theory of Turbulence.” *Proc. NAS*, Vol. 34, November 1948, p. 530-9.

[19] Hill, R.J. and S.F. Clifford. "Modified spectrum of atmospheric temperature fluctuations and its application to optical propagation." *J. Opt. Soc. Am*., Vol. 68, No. 7, 1978, p. 892-9.

[20] Andrews, Larry C., et al. *Laser Beam Scintillation with Applications*. SPIE Press: Bellingham, Washington, 2001.

[21] Wheelon, Albert D. *Electromagnetic Scintillation*, Vol. 2, *Weak Scattering*. Cambridge University Press: Cambridge, 2003.

[22] Sasiela, Richard J. (ed.). *Electromagnetic Wave Propagation in Turbulence*. Springer-Verlag: Berlin, 1994.

[23] Goodman, J.W. *Statistical Optics*. Wiley: New York, 2000.

[24] Churnside, James H. "Aperture-Averaging Factor for Optical Propagation Through the Turbulent Atmosphere." *NOAA Technical Memorandum* ERL WPL-188, November 1990. (available from the National Technical Information Service <http://www.ntis.gov>).

[25] Fried, D.L. "Optical Resolution Through a Randomly Inhomogeneous Medium for Very Long and Very Short Exposures." *J. Opt. Soc. Am*., Vol. 56, No. 10, October 1966, p. 1372-9.

[26] Gracheva, M.E. and A.S. Gurvich. "Strong fluctuations in the intensity of light propagated through the atmosphere close to the Earth." *Sov. Radiophys*., Vol. 8, No. 4, 1965, p. 511-5.

[27] Prokhorov, A.M. et al. "Laser Irradiance Propagation in Turbulent Media." *Proc. IEEE*, Vol. 63, No. 5, May 1975, p. 790-811.

[28] Coles, W.A. and R.G. Frehlich. “Simultaneous measurements of angular scattering and intensity scintillation in the atmosphere.” *J. Opt. Soc. Am*., Vol. 72, No. 8, August 1982, p. 1042-8.

[29] Fante, Ronald L. “Inner-scale size effect on the scintillations of light in the turbulent atmosphere.” *J. Opt. Soc. Am*., Vol. 73, No. 3, March 1983, p. 277-281.

[30] Frehlich, R.G. “Intensity covariance of a point source in a random medium with a Kolmogorov spectrum and an inner scale of turbulence.” *J. Opt. Soc. Am*., Vol. 4, No. 2, February 1987, p. 360-6.

[31] Hill, R.J. and S.F. Clifford. “Theory of saturation of optical scintillation by strong turbulence for arbitrary refractive-index spectra.” *J. Opt. Soc. Am*., Vol. 71, No. 6, June 1981, p. 675-86.

[32] Clifford, S.F. and H.T. Yura. “Equivalence of two theories of strong optical scintillation.” *J. Opt. Soc. Am*., Vol. 64, No. 12, December 1974, p. 1641-4.

[33] Andrews, L.C. et al. “Aperture averaging of optical scintillations: power fluctuations and the temporal spectrum.” *Waves Random Media*, Vol. 10, 2000, p. 53-70.

[34] Andrews, L.C. “Aperture-averaging factor for optical scintillations of plane and spherical waves in the atmosphere.” *J. Opt. Soc. Am*., Vol. 9, No. 4, April 1992, p. 597-600.

[35] Churnside, James H. “Scintillation from a Diverging Laser Beam.” *NOAA Technical Memorandum* ERL ETL-240, September 1994. (available from the National Technical Information Service <http://www.ntis.gov>).

[36] Hutt, D.L. “Modeling and measurements of atmospheric optical turbulence over land.” *Opt. Eng*., Vol. 38, No. 8, August 1999, p. 1288-95.

[37] Oke, T.R. *Boundary Layer Climates*. Methuen & Co.: London, 1978.

[38] Ochs, Gerard R. and Reginald J. Hill. “Optical-scintillation method of measuring turbulence inner scale.” *Appl. Opt*., Vol. 24, No. 15, 1 August 1985, p. 2430-2.

[39] Frehlich, Rod G. “Estimation of the parameters of the atmospheric turbulence spectrum using measurements of the spatial intensity covariance.” *Appl. Opt*., Vol. 27, No. 11, June 1988, p. 2194-8.

[40] Hill, R.J. “Saturation resistance and inner-scale resistance of a large-aperture scintillometer: a case study.” *Appl. Opt*., Vol. 20, No. 22, 15 November 1981, p. 3822-4.

[41] Hill, Reginald J. and Rod. G. Frehlich. “Onset of strong scintillation with application to remote sensing of turbulence inner scale.” *Appl. Opt*., Vol. 35, No. 6, 20 February 1996, p. 986-97.

[42] Churnside, James H. et al. “Aperture size and bandwidth requirements form measuring strong scintillation in the atmosphere.” *Appl. Opt*., Vol. 28, No. 19, 1 October 1989, p. 4126-32.

[43] Derickson, Dennis (ed.). *Fiber Optic Test and Measurement*. Prentice Hall PTR: New Jersey, 1998.

[44] Churnside, James H. and Richard J. Lataitis. “Wander of an optical beam in the turbulent atmosphere.” *Appl. Opt*., Vol. 29, No. 7, 1 March 1990, p. 926-30.

[45] Ishimaru, Akira. *Wave Propagation and Scattering in Random Media*. IEEE Press and Oxford University Press: New York, 1997.

[46] Tyson, Robert K. and Douglas E. Canning. "Indirect measurement of a laser communication bit-error-rate reduction with low-order adaptive optics." *Appl. Opt*., Vol. 42, No. 21, 20 July 2003, p. 4239-43.

[47] Korotkova, Olga and Larry C. Andrews. "Model for a partially coherent Gaussian beam in atmospheric turbulence with application in Lasercom." *Opt. Eng*., Vol. 43, No. 2, February 2004, p. 330-41.

[48] Welford, W.T. and R. Winston. *High Collection Nonimaging Optics*. Academic Press: San Diego, 1989.

[49] Winston, R. "Dielectric compound parabolic concentrators." *Appl. Opt*., Vol. 15, No. 2, February 1976, p. 291-2.

[50] Miñano, Juan C. et al. "Ultra compact optics for optical wireless communications." *Proc. SPIE*, Vol. 3850, *Optical Wireless Communications II*, September 1999, p. 80-90.

[51] Mohedano, Rubén et al. "Ultracompact nonimaging devices for optical wireless communications." *Opt. Eng*., Vol. 39, No. 10, October 2000, p. 2740-7.

[52] Agrawal, Govind P. *Fiber-Optic Communication Systems*. John Wiley & Sons: New York, 1997.

[53] Davis, Christopher C. and Igor I. Smolyaninov. "The Effect of Atmospheric Turbulence on Bit-Error-Rate in an On-Off-Keyed Optical Wireless System." *Proc. SPIE*, Vol. 4489, *Free-Space Laser Communication and Laser Imaging*, July 2002, p. 126-137.

[54] Biswas, A. and M.W. Wright. “Mountain-Top-to-Mountain-Top Optical Link Demonstration: Part I.” *IPN Progress Report* 42-149, Jet Propulsion Laboratory, Pasedena, CA, 15 May 2002.

[55] Kim, Isaac I. et al. “Comparison of laser beam propagation at 785 nm and 1550 nm in fog and haze for optical wireless communications.” *Proc. SPIE*, Vol. 4214, *Optical Wireless Communications III*, February 2001, p. 25-37.

[56] Moore, C.I. et al. “Free-space high-speed laser communication link across the Chesapeake Bay.” *Proc. SPIE*, Vol. 4821, *Free Space Laser Communication and Laser Imaging II*, December 2002, p. 474-485.

[57] Gilbreath, C.G. and W.S. Rabinovich. “Research in Free-space Optical Data Transfer at the U.S. Naval Research Laboratory.” *Proc. SPIE*, Vol. 5160, *Free-Space Laser Communication and Active Laser Illumination III*, January 2003, p. 225-33.

[58] “Maxim 1.25Gbps/2.5Gbps, +3V to +5.5V, Low-Noise Transimpedance Preamplifiers for LANs.” Rev. 1, June 2000, Maxim Integrated Products.

[59] “Accurately Estimating Optical Receiver Sensitivity.” *Application Note: HFAN-3.0.0*, October 2001, Maxim Integrated Products.